CHEMICAL REVIEWS

pubs.acs.org/CR

Review

Electroceramics for High-Energy Density Capacitors: Current Status and Future Perspectives

Ge Wang,[‡] Zhilun Lu,[‡] Yong Li,[‡] Linhao Li, Hongfen Ji, Antonio Feteira, Di Zhou, Dawei Wang,* Shujun Zhang,* and Ian M Reaney*

Cite This: https://doi.org/10.1021/acs.chemrev.0c01264

Read Online

ACCESS | Metrics & More | Article Recommendations

ABSTRACT: Materials exhibiting high energy/power density are currently needed to meet the growing demand of portable electronics, electric vehicles and large-scale energy storage devices. The highest energy densities are achieved for fuel cells, batteries, and supercapacitors, but conventional dielectric capacitors are receiving increased attention for pulsed power applications due to their high power density and their fast charge−discharge speed. The key to high energy density in dielectric capacitors is a large maximum but small remanent (zero in the case of linear dielectrics) polarization and a high electric breakdown strength. Polymer dielectric capacitors offer high power/energy density for applications at room temperature, but above 100 °C they are unreliable and suffer from dielectric breakdown. For high-temperature applications, therefore, dielectric ceramics are the only feasible alternative. Lead-based ceramics such as La-doped lead zirconate titanate exhibit good energy storage properties, but their toxicity raises concern over their use in consumer applications, where capacitors are exclusively lead free. Lead-free compositions with superior power density are thus required. In this paper, we introduce the fundamental principles of energy storage in dielectrics. We discuss key factors to improve energy storage properties such as the control of local structure, phase assemblage, dielectric layer thickness, microstructure, conductivity, and electrical homogeneity through the choice of base systems, dopants, and alloying additions, followed by a comprehensive review of the state-of-the-art. Finally, we comment on the future requirements for new materials in high power/energy density capacitor applications.

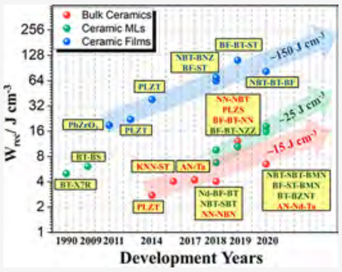

CONTENTS

Received: November 30, 2020

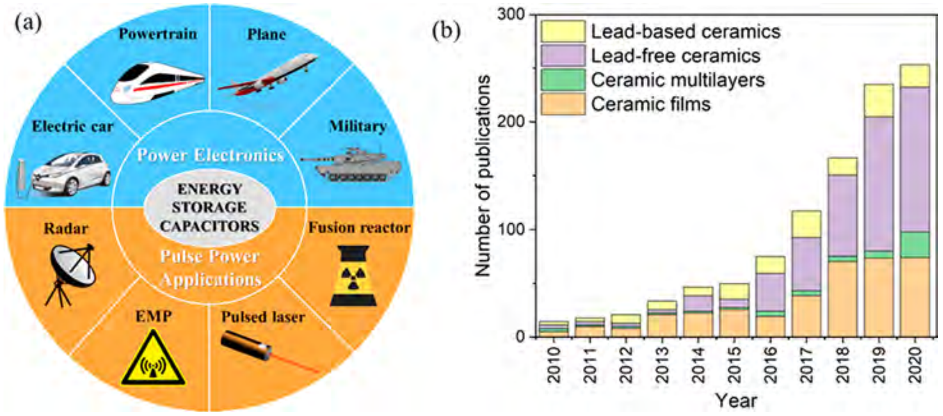

Figure 1. (a) Applications for energy storage capacitors. *EMP: electromagnetic pulse. (b) Number of annual publications on lead-based ceramics, lead-free ceramics, ceramic multilayers, and ceramic films for energy storage capacitors from 2010 to 2020. (Collected from Web of Science, search "energy storage/density lead-based ceramic, lead-free ceramic, multilayer ceramic, ceramic capacitor, ceramic films but NOT polymer"). Reproduced with permission from PixaBay, Creative Commons License.

1. INTRODUCTION

To limit global warming to <1.50 °C, as set out in the Paris agreement, carbon dioxide emissions need to decrease ∼45% by 2030 and reach net-zero by 2050.[1,2] Technologies based on renewable resources such as sun, wind, and tides will play a pivotal role to meet these targets. Although the increasing deployment of renewable energies is encouraging, there still are many barriers to the replacement of power generation from traditionally high CO_2-emitting sectors based on coal and gas, which is still a critical and large portion of the energy generation, due to the intermittent nature of renewables. Hence, to simultaneously move away from fossil fuels and to circumvent the unpredictability inherent in clean energy resources, it is necessary to integrate energy-harvesting technologies with energy storage devices.

Energy storage, therefore, is emerging as a key enabler for sustainable renewable technologies, particularly for the electrification of transportation but also in more specialized applications such as heart defibrillators and active armor.[3] Technologies already exist to store energy, such as batteries, electrochemical supercapacitors, and electrostatic capacitors.[4−16] The latter are electrical energy-storage devices belonging to the category of passive components, which are ubiquitous in electronics. Indeed, every year more than 3 trillion multilayer ceramic capacitors (MLCCs) are manufactured from $BaTiO_3$ (BT), the prototypical ferroelectric (FE) ceramic.[17−22]

In comparison with Li-ion batteries or fuel cells, the nonpolarized electrostatic or dielectric capacitors possess high power density (∼10^4−10^5 W/kg) resulting from their faster charging/discharging characteristics (∼μs), which are advantageous for power electronics in electrical vehicles (EVs) and pulse power applications (Figure 1a).[4,23−27] Hence, electrostatic capacitors are emerging as promising candidates for energy storage devices, where high power density in combination with high energy density are important technological requirements, as illustrated by the exponential rise in publications devoted to energy storage involving electrostatic ceramic capacitors, Figure 1b. Apart from high energy density and fast charging−discharging rate, other properties such as temperature/frequency stability, fatigue resistance, lifetime reliability, equivalent series resistance, and manufacturing cost are equally important for dielectric capacitors used in practical applications. New electroceramics are, therefore, required to facilitate near-engine power electronics, exhibit ultrafast charging, and have more durable EV performance at high temperature and voltage. Thus, future electroceramics must (i) deliver high energy density (W_{rec} > 10 J cm^{-3}) and conversion efficiencies (η > 90%); (ii) endure wider temperature ranges (−50−250 °C) and frequency ranges (1−1000 Hz); (iii) exhibit greater reliability (>10^5 cycles) and fatigue resistance (<5% change over capacitor lifetime); and (iv) be compatible with cost-effective internal electrodes and be easily integrated with other components.

Historically, many different dielectric materials, ranging from paper and plastic to ceramics, have been employed in the fabrication of electrostatic capacitors. Nowadays, capacitors are fabricated from either polymers or ceramics because they offer the best combination of properties in terms of capacitance, dielectric loss, breakdown strength (BDS), and for the latter, thermal stability.

The prospects of employing ceramic capacitors for energy storage can be traced back to the 1960s work by Jaffe[28] from the Clevite Corp., USA. One decade later, Burn and Smyth[29] from Sprague Electric Company evaluated the energy storage performance in $SrTiO_3$ (ST) and BT with applied electric fields up to 400 kV cm^{-1}. Until that point, quantitative data of energy storage on these materials were limited to fields generally smaller than 150 kV cm^{-1} due to the relatively low dielectric BDS of the fabricated ceramics. They emphasized that the maximum energy density for a ceramic should be obtained for thinner dielectric layers due to the lower probability for the occurrence of defects (such as pores, voids, or microcracks), which are well-known sources of dielectric breakdown. Later in 1990, Love,[30] also from Sprague Electric Company, revisited energy storage in ceramic capacitors and highlighted empirical design principles to achieve enhanced energy storage in capacitors, as shown in Table 1. Commercial *C0G*-type capacitors are manufactured from low relative permittivity (ε_r) linear dielectrics but may achieve an energy storage of 1 J cm^{-3}, by virtue of their intrinsically high BDS. The significance of the BDS, to achieve high energy storage becomes apparent in the case of *X7R*-type capacitors, fabricated from high ε_r BT. An important correlation between dielectric BDS and the thickness (t) can be extracted from Table

Table 1. General Characteristics of Commercial Type Ceramic Materials Relevant for Energy Storage (Adapted from Love[30]) Using Electronic Industries Alliance (EIA) Classifications[a]

dielectric type	dielectric BDS (V μm^{-1})	relative permittivity, ε_r	t (μm)	energy at 1 kV (J cm^{-3})
C0G (temperature coefficient 0 with tolerance ±30 × 10^{-6}/K)	65	75	18.5	0.88
Z5U (+10/+85 °C, $\Delta C/C_0$ = +22/−56%)	13.2	7500	95	0.02
X7T (−55/+125 °C, $\Delta C/C_0$ = +22/−33%)	16	2800	70	0.71
X7R (−55/+125 °C, $\Delta C/C_0$ = ± 15%)	30	2000	38	1.40
X7R	40	2000	30	1.34
X7R	90	1800	20	4.82

[a] Class I ceramic capacitors are accurate, temperature-compensating capacitors, *C0G* will have 0 drift with a tolerance of ±30 × 10^{-6}/K. Class II ceramic capacitors have a dielectric with a high permittivity. *C* and C_0 are represented capacitance value and capacitance value at 25 °C.

1. Indeed, by halving the t of the dielectric layers, the energy storage appears to increase >3 fold. This effect has been recently captured by Yang and co-workers,[31] who compiled BDS data from literature for several dielectric materials of different t and observed decay inversely proportional to $(t)^a$, where a was determined as 0.5. Finally, when comparing the energy storage of *Z5U* and *X7R*, it becomes apparent that high ε_r alone is not a sufficient parameter to achieve high energy storage. Interestingly, Love[30] stressed that the capacitor industry was rather conservative in terms of perfecting the BDS of ceramics to reach values near those of single-crystals, which would significantly enhance the energy storage in ceramic capacitors.

Love[30] proposed that maximum energy storage density can be achieved in intermediate rather than high ε_r materials since they exhibit larger BDS. Fletcher and co-workers[32] convincingly postulated that greater energy storage densities can indeed be achieved in FE materials, whose Curie temperature (T_c) is adjusted to ensure that the material is operated in the paraelectric regime, where it shows a relatively small zero-field ε_r, an approach already mentioned by Jaffe in 1961.[28]

In 2009, Ogihara and co-workers[33] proposed the use of so-called weakly coupled relaxors, such as $0.7BaTiO_3{-}0.3BiScO_3$ (0.7BT−0.3BS), to fabricate energy storage devices. This new conceptual approach aimed at exploiting the extraordinary temperature stability of ε_r exhibit by this family of materials. When compared with commercial *X7R* capacitors, 0.7BT−0.3BS capacitors displayed superior performance, reaching a recoverable energy density (W_{rec}) of 6.1 J cm^{-3} at 730 kV cm^{-1}. Again, the large dielectric BDS played a decisive role in this performance. More recently, in 2019 Wang, Reaney and co-workers[34] unveiled a novel approach to enhance energy storage characteristics via the fabrication of chemically heterogeneous but electrically homogeneous ceramics, with W_{rec} reaching 10.5 J cm^{-3}, as detailed later in this review.

Here, we present the principles of energy storage performance in ceramic capacitors, including an introduction to electrostatic capacitors, key parameters for evaluating energy storage properties, microstructural considerations, and critical electrical factors. Second, we will review the current state-of-the-art for lead and lead-free electroceramics for energy storage capacitors with bulk ceramics, ceramic multilayers (MLs), ceramic films and glass ceramics evaluated separately. Third, we will describe strategies for optimizing energy storage in electroceramics. Finally, we will demonstrate, with appropriate examples, a guide to the future development for electroceramics in energy storage capacitors.

2. PRINCIPLES OF ENERGY STORAGE IN ELECTROCERAMICS

2.1. Electrostatic Capacitors

The simplest dielectric capacitor consists of two parallel metallic plates separated by an insulator, which becomes polarized under the application of an electric field. This is the defining behavior of a dielectric material. The actual capacitance, C (i.e., ability to store charge), of an ideal capacitor is given by the ratio of the charge, Q, stored on each metallic plate and the applied voltage, V, as shown by eq 1.

$$C = \frac{Q}{V}(F) \tag{1}$$

Nevertheless, from a practical viewpoint, a more useful equation to compute the C of a real device, as illustrated in Figure 2, encompassing a dielectric material between two parallel plates of area, A, separated by a distance, d, subject to a V, can be obtained through the application of Gauss's law

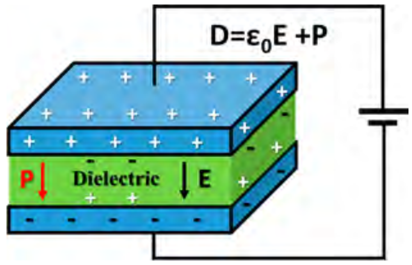

Figure 2. Schematic representation of an electrostatic capacitor, where D, P, and ε_0 are electric displacement, polarization, and electric permittivity of free space (electric constant), respectively.

$$V = \frac{Qd}{\varepsilon A} \tag{2}$$

where ε is the permittivity of the dielectric, and a measure of its polarizability. Combination of eqs 1 and 2 provides the relationship:

$$C = \frac{A}{\varepsilon\ d}(\mathrm{F}) \tag{3}$$

From eq 3, it becomes immediately apparent that the ability of dielectric capacitor to charge and, therefore store energy, is ultimately associated with ε of the dielectric.

2.2. Key Parameters for Evaluating Energy Storage Properties

During the application of a V, the electrostatic energy stored, W, in the dielectric can be estimated by

$$W = \int_0^{Q_{max}} V\ dq\ (\mathrm{J}) \tag{4}$$

where Q_{max} is the maximum charge achieved at the end of the charging cycle and dq is the incremental charge increase during the charging cycle. The volumetric energy density, W_{st} (i.e., the energy stored per volume unit, $A\ d$), is a common key performance indicator, expressed by

$$W_{st} = \frac{W}{A\ d} = \frac{\int_0^{Q_{max}} V dq}{A\ d} = \int_0^{D_{max}} E\ dD\ (\mathrm{Jm^{-3}}) \qquad (5)$$

where E is the electric field and D_{max} is the electric displacement in the material under the maximum applied field, E_{max}. The electrical displacement (D) corresponds to the charge density (Q/A) on the metallic plates and is expressed by $D = \varepsilon_0 E + P$ (Figure 2), where P is the polarization (surface charge density).

For high ε materials, D is approximately equal to P, and it follows that $D = \varepsilon E = \varepsilon_0 \varepsilon_r E$, where ε_0 is the permittivity of free space ($= 8.854 \times 10^{-12}$F m^{-1}) and ε_r is the relative permittivity, which is the $\varepsilon/\varepsilon_0$ ratio. This approximation allows stored energy density (W_{st}) to be defined in terms of P, as follows

$$W_{st} = \int_0^{P_{max}} E\ dP = \int_0^{E_{max}} \varepsilon_0 \varepsilon_r E\ dE \qquad (6)$$

where P_{max} is the maximum polarization reached at the E_{max}. From a practical viewpoint, eq 6 is prevalent in the calculation of W_{st} because several experimental methods exist to determine P under an applied E. In 1961, Jaffe[28] pointed out that the recoverable energy (W_{rec}) corresponds to the area above the discharging curve, whose upper limit is given by the P_{max}. Essentially, the mathematical integration of the area above a polarization-electric (P–E) loop provides an estimate of W_{rec}, as schematically illustrated in Figure 3 for four distinct types of polarization response.

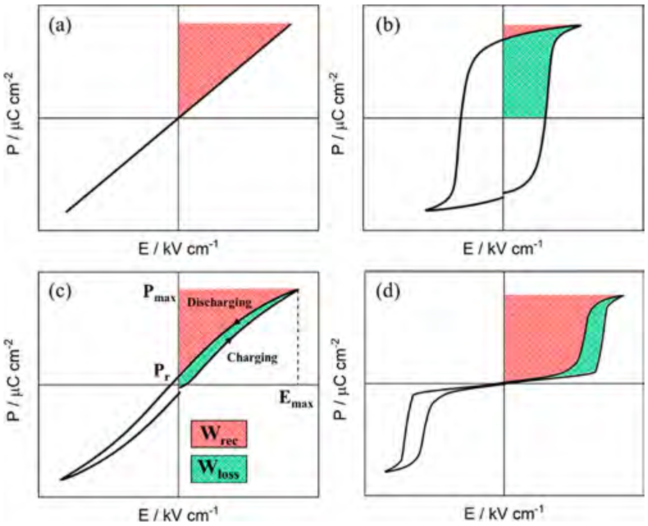

Figure 3. Four distinctive P–E hysteresis loops and their energy storage behavior: (a) linear, (b) FE, (c) relaxor-ferroelectric (with the schematic of energy storage calculation), and (d) antiferroelectric materials. *W_{loss} is loss energy density.

For linear dielectrics such as Al_2O_3, where ε_r is independent of the applied E. The calculation of W_{rec} from the P–E response illustrated in Figure. 3a, is given by

$$W_{rec} = \frac{1}{2} \varepsilon_0 \varepsilon_r E^2 \qquad (7)$$

which clearly shows that W_{rec} is dependent on ε_r and E. Parts b–d of Figure 3 show cases where polarization responses deviate from linearity, and consequently, the computation of W_{rec} needs to be carried out using eq 6. The response illustrated in Figure 3b is typical of a classical FE material, such as BT, where the hysteresis is linked to polarization switching of macroscopic FE domains, as explained in detail in the review by Damjanovic.[35] Already in 1961, Jaffe[28] stressed that in FEs, charging energy is mainly absorbed by domain switching and is retained as remanent polarization (P_r). The typically high remanence of classical FEs can be effectively minimized via chemical doping, giving rise to the response shown in Figure 3c, which is characteristic of relaxor-ferroelectrics (RFEs), such as doped-BT and $Pb(Mg_{1/3}Nb_{2/3})O_3$.[36]

It is now generally accepted that relaxor behavior originates from the response of polar nanoregions (PNRs) to an alternating E. RFEs remain unsaturated at high applied E, and therefore, any increment of the E will have a contribution to energy storage. Remanence-free materials are therefore, preferable for achieving high W_{rec}. Linear dielectric materials meet this requirement but due to their low ε_r, energy storage is limited. Antiferroelectrics (AFEs) display low-remanence under low E but at large E the P–E loop opens due to the stabilization of an FE with respect to AFE phase and they display a saturated polarization, as illustrated in Figure 3d. In principle, therefore, as suggested by Jaffe,[28] AFEs should afford advantages for high energy storage, providing that dielectric breakdown issues are eliminated (i.e., the BDS should be high enough to induce the AFE-FE phase transition).

From the above, it becomes evident that nonlinear dielectric materials such as FEs, RFEs, and AFEs exhibit energy dissipation (W_{loss}); therefore, the W_{rec} is actually the most important parameter, as schematically illustrated in Figure 3c (red area). Hence, W_{rec} becomes

$$W_{rec} = \int_{P_r}^{P_{max}} E\ dP \qquad (8)$$

Energy conversion efficiency of a capacitor can then be calculated as

$$\eta = \frac{W_{rec}}{W_{rec} + W_{loss}} \qquad (9)$$

where W_{loss} is the energy loss during discharging, which correlates to the area enclosed by the P–E loop (Figure 3c green area).

Electric-field induced polarization can be determined via the measurement of charge, current, and voltage responses, typically achieved using either the Sawyer–tower, the virtual ground, the

Table 2. Comparison of Different Hysteresis Measurement Methods for FEs[37]

method	measured quantity	reference component	integration necessary	bandwidth requirement	influence of parasitics
Sawyer–tower	charge Q	capacitor	no	moderate	high
virtual ground	current I	no	yes	high	low
shunt	current I	resistor	yes	high	high
current step	voltage V	no	no	moderate	moderate

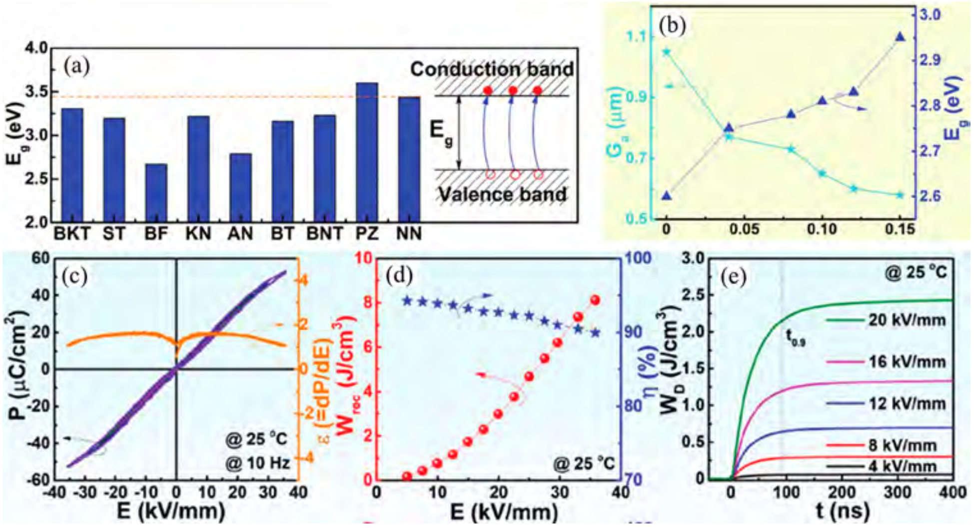

Figure 4. (a) Comparison of the E_g among dielectric perovskites and a schematic of electronic breakdown. (b) Variation of average grain size and E_g as a function of NN concentration. (c) P−E loops and dP/dE under different E, (d) W_{rec} and η values, and (e) pulsed overdamped discharging energy density (W_D) of the BF−BT−0.10NN ceramic. (a) Reproduced with permission from ref 42. Copyright 2019 John Wiley and Sons. (b-e) Reproduced with permission from ref 43. 2020 John Wiley and Sons.

shunt or the current step methods. Each presents advantages and disadvantages as listed in Table 2. For details of each method, the reader is referred to Prume and co-workers.[37] Prume, Schmitz, and Tiedke proposed that overall the virtual ground method offers the highest precision for the measurement of FEs.

2.3. Key Factors for Optimizing Energy Density

The microstructural features of electroceramics, such as density, grain size, secondary phases and core−shell structures, play an important role in energy storage properties. Simultaneously, the intrinsic electrical response, e.g., band gap, alongside the electrical microstructure, i.e., the distribution of conductive and resistive elements, are equally critical factors for the optimization of energy density. The following section reviews these factors, and gives examples of where and how they may be optimized.

2.3.1. Intrinsic Band Gap. The band gap (E_g) is the forbidden energy between the top of the valence band and bottom of the conduction band. E_g is commonly used to define insulator ($E_g > 4.0$ eV), semiconductor ($0.0 \text{ eV} < E_g < 4.0$ eV), and metal ($E_g = 0.0$ eV). For semiconductor, the intrinsic BDS can be defined as

$$\text{BDS} = 1.36 \times 10^7 \times (E_g/4.0)^3 \text{ (V/cm)} \tag{10}$$

where BDS is direct proportional to E_g.[38] Thus, semiconductors with wider E_g have higher intrinsic BDS. The electronic structure and band gaps of semiconductor can be studied theoretically using, e.g., linear discriminant analysis, or experimentally, e.g., absorbance spectroscopy and diffuse reflectance spectroscopy.[39] A general rule of thumb is that the activation energy (E_a) for conduction is approximately half E_g. Both may be increased by doping or through the formation of solid solutions, often delivering higher BDS and W_{rec}.[40,41]

For example, the highest $E_g \sim 3.58$ eV among all different kinds of lead-free electroceramics was found in NaNbO$_3$ (NN), as shown in Figure 4a.[42] Thus, NN was introduced into Na$_{0.5}$Bi$_{0.5}$TiO$_3$ (NBT) and BiFeO$_3$−BaTiO$_3$ (BF−BT) to enhance E_g. The E_g for BF−BT−xNN ceramics increased from 2.5 eV up to 2.95 eV for $x \leq 0.15$, as shown in Figure 4b accompanied by significant enhanced $W_{rec} \sim 8.12$ J cm^{-3} under electric field ~400 kV cm^{-1}, along with greater thermal stability (±10%, −50 to +250 °C) and ultrafast discharge rate ($t_{0.9} < 100$ ns), Figure 4.[43]

2.3.2. Electrical Microstructure. The distribution of regions with different conductivity and ε_r are important aspects of the so-called "electrical microstructure" of electroceramics.[44] In many instances, such as the core−shell microstructure or grain boundary response of BT based ceramics, the distributions are markedly heterogeneous and lead to localization of the electrical field strength in lower ε_r regions or pathways for breakdown through interconnected conducting regions. In 2019, electrical homogeneity was for the first-time proposed by Wang, Reaney and co-workers in the BF−BT system as a key factor to optimize BDS and as a consequence W_{rec}. Electrical heterogeneity was effectively eliminated by alloying with a third end-member so that it became more difficult to form a conductive pathway at high field, resulting in higher BDS and W_{rec}.[34]

A homogeneous electrical microstructure may be obtained in many different ways such as heat-treatment in the appropriate atmosphere (N$_2$, Air, O$_2$) provided the type and magnitude of electrical conductivity is affected by oxygen stoichiometry. Practically, however, in production, a suitable dopant strategy is utilized once the conduction type is known (p vs n type). For example, the conductivity of BF-ST-based compositions is suppressed by doping with 3 mol % Nb on the B-site to compensate for Bi volatilization and the formation of oxygen vacancies ($V_O^{\cdot\cdot}$), through variation of the Fe valence (Fe^{3+} to Fe^{4+}).[45]

For materials with more than one bulk-like region, e.g., phase mixtures, core−shell microstructures, or surface layers, alternating current (AC) impedance spectroscopy (IS) is able to show multiple responses and the resistance (R) and C can be extracted.[46−53] Both the volume fraction and difference in magnitude of R and C for multiple electrical responses are equally important in influencing energy storage performance. Given the importance of the electrical microstructure, a brief outline of the role of IS is described and its advantages with respect to direct current methods are emphasized.

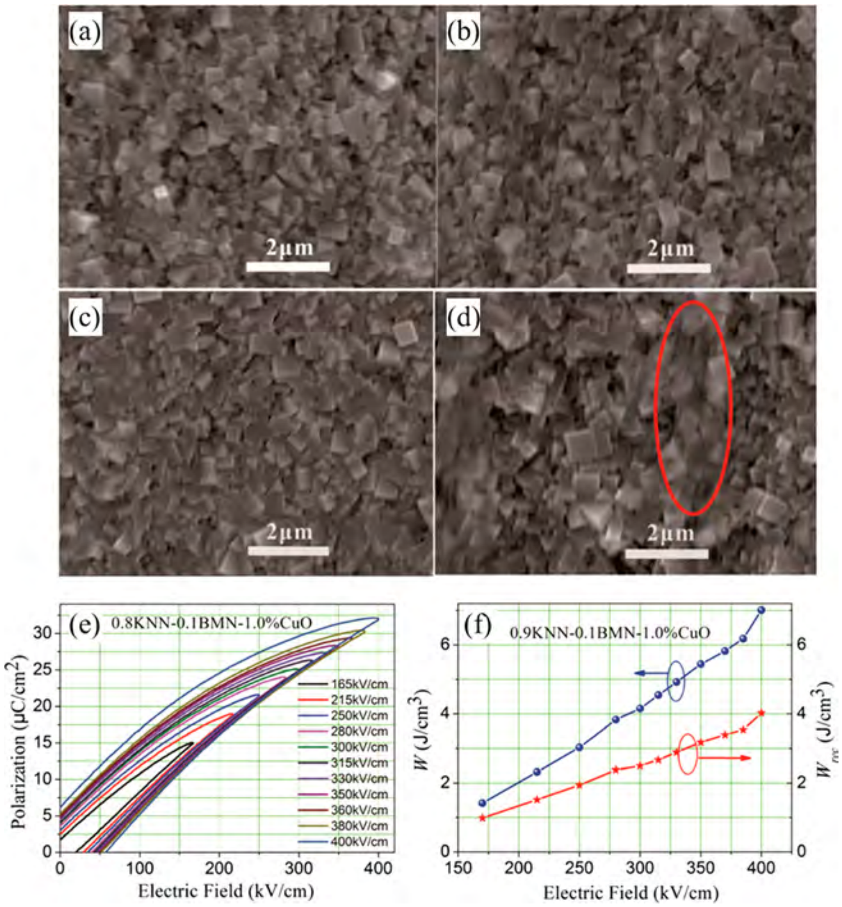

Figure 5. Scanning electron microscopy (SEM) images of the 0.9KNN-0.1BMN-x mol % CuO ceramics with (a) $x = 0.25$; (b) $x = 0.5$; (c) $x = 1.0$; (d) $x = 1.5$, as liquid phase is circled in red. (e) Unipolar $P-E$ hysteresis loops and (f) Calculated W and W_{rec} under different E of 0.9KNN-0.1BMN-1 mol % CuO ceramics.[66] Reproduced with permission from ref 66. Copyright 2017 John Wiley and Sons.

Direct current (DC) electrical measurements are the most commonly employed technique to evaluate the electrical characteristics of materials. However, they merely give the overall response instead of the properties of specific regions (e.g., grains and grain boundaries) unless microprobe techniques are employed.[54,55] Such techniques are useful but the sample volume is small, which casts doubt on their ability to represent global behavior and they are difficult to implement experimentally.

An alternative and much more convenient technique is IS. In IS measurements, an AC signal with small voltage over a wide range of frequency, typically 10^{-2} to 10^{7} Hz, is applied on the sample.[44,56] The small voltage prevents any permanent change to the sample as well as yielding a (near) linear relationship between input and output. The wide range of frequencies allows separation of the response of different electro-active regions according to their relaxation times. For energy storage capacitors, impedance is capable of: (i) establishing the contributions to the electrical microstructure (grains, grain boundaries, core−shell structure and electrode−sample interface) and determine their individual conductivity and ε_r which give an insight into the distribution of electrical components within the sample; (ii) verifying the origin of the dominant electrical behavior (i.e., grains, grain boundary or interfacial layer response);[57,58] and (iii) determining the conduction mechanism and charge carrier type which helps further interpret the electrical response of the material.[47]

Impedance can be defined as a complex number which usually contains both resistive and reactive (capacitive and/or inductive) components:

$$Z^* = Z'(\text{resistive}) - jZ''(\text{reactive}) \tag{11}$$

Different electro-active regions of a material are characterized by a R and a C, usually in parallel. Then the electric relaxation time or time constant, τ, of each region can be expressed as its R and C

$$\tau = RC \tag{12}$$

at the frequency of maximum loss, ω_{max}, it holds the relation:

$$\omega_{max}RC = \omega_{max}\tau = 1 \tag{13}$$

Due to their different R and C values, electro-active regions can be separated in the frequency domain. Once the value of R and C are extracted, they can then be assigned to appropriate regions of the sample.

Normally the impedance measurement needs to be taken over a temperature and/or oxygen partial pressure ($p\text{O}_2$) range to gain a better understanding of the conduction mechanism and the charge carrier. The associated activation energy, E_a, can be estimated using Arrhenius equation

$$\sigma = \sigma_0 \exp(E_a/kT) \tag{14}$$

where σ is the conductivity, σ_0 is pre-exponential factor, k is the Boltzmann constant, and T is temperature. E_a may be related to predominant charge carrier and conduction mechanism. The type of charge carrier may also be determined to some extent by

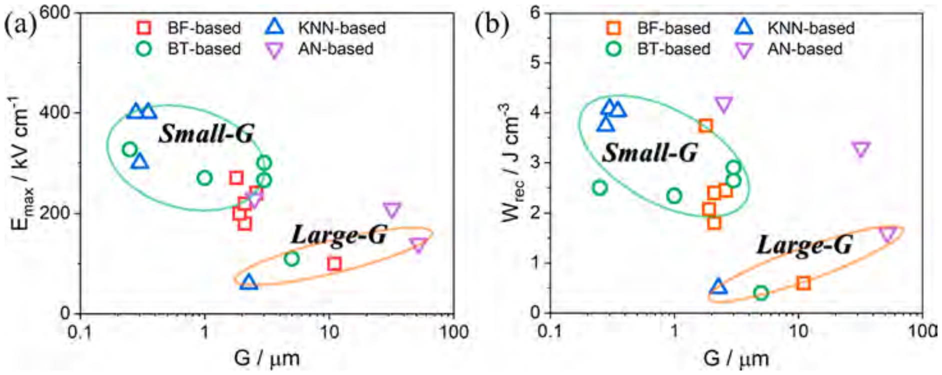

Figure 6. Relationship between energy storage properties of ceramics and *G*: (a) *G* vs E_{max} and (b) *G* vs W_{rec}. *AN: $AgNbO_3$.

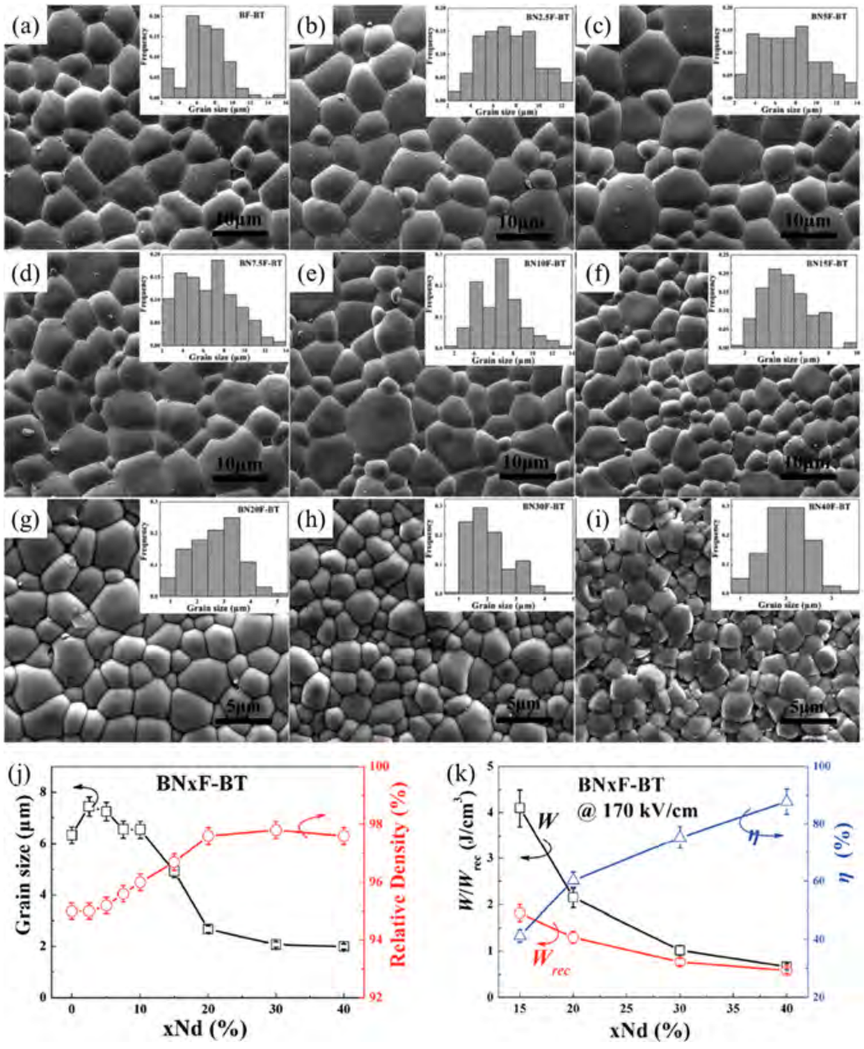

Figure 7. SEM images of *x* mol % Nd-doped BF−BT with different Nd concentrations: (a) BF−BT, (b) 2.5 mol % Nd−BF−BT, (c) 5 mol % Nd−BF−BT, (d) 7.5 mol % Nd−BF−BT, (e) 10 mol % Nd−BF−BT, (f) 15 mol % Nd−BF−BT, (g) 20 mol % Nd−BF−BT, (h) 30 mol % Nd−BF−BT, and (i) 40 mol % Nd−BF−BT; the *G* distributions of Nd-doped BF−BT are shown in the insets of the SEM images.[90] (j) *G*, density and (k) energy storage performance at 170 kV cm^{-1}, as a function of *x*(Nd) mol % in BF−BT ceramics. Reproduced with permission from ref 90. Copyright 2017 Royal Society of Chemistry.

the pO_2 dependence of conductivity, i.e., *p*-type: conductivity increases with increasing pO_2; *n*-type: conductivity decreases with increasing pO_2; ionic charge carrier: conductivity is independent with pO_2.

2.3.3. Density and Porosity. The density of the ceramic materials plays an essential role on electrical performance, especially BDS. Ceramics with higher density tend to support higher *E* closer to the intrinsic/theoretical BDS. In contrast, low density ceramics exhibit conductive pathway composed of pores/voids which result in short circuit under modest field strengths. The relationship between the voltage across the pore and the external *E* based on a "slab" model is shown below

Table 3. Summary of Energy Storage Properties for Lead-Based Ceramics[a]

compositions	E (kV cm^{-1})	ΔP (μC cm^{-2})	W_{rec} (J cm^{-3})	η (%)	ref
$(Pb_{0.89}Ba_{0.08}La_{0.02})(Zr_{0.7}Sn_{0.27}Ti_{0.03})O_3$	135	22.6	2.1	76.5	150
$(Pb_{1.067}La_{0.02})(Zr_{0.95}Ti_{0.05})O_3$	90	39.5	2.12	92.98	141
$0.90(Pb_{0.97}La_{0.02})(Zr_{0.65}Sn_{0.30}Ti_{0.05})O_3{-}0.10Bi(Zn_{2/3}Nb_{1/3})O_3$	115	29	2.19	95.6	162
$Pb_{0.97}La_{0.02}(Zr_{0.58}Sn_{0.35}Ti_{0.07})O_3$	118	29.0	2.35	86.1	158
$Pb_{0.91}La_{0.02}Ba_{0.06}(Zr_{0.65}Sn_{0.3}Ti_{0.05})O_3$	150	29.5	2.4	82	159
$(Pb_{0.93}Ba_{0.04}La_{0.02})(Zr_{0.65}Sn_{0.3}Ti_{0.05})O_3{-}0.005Mn_2O_3$	308	31.5	2.64	73	161
$Pb_{0.97}La_{0.02}(Zr_{0.33}Sn_{0.55}Ti_{0.12})O_3@0.05SiO_2$	238	34.6	2.68	83.5	87
$(Pb_{0.87}Ba_{0.1}La_{0.02})(Zr_{0.65}Sn_{0.3}Ti_{0.05})O_3{-}0.75Y$	130	46.5	2.75	71.5	149
$(Pb_{0.88}La_{0.08})(Zr_{0.91}Ti_{0.09})O_3$	170	31.5	3.04	92	112
1.7 mol % Pr^{3+} doped $0.24Pb\ (In_{1/2}Nb_{1/2})O_3{-}0.42Pb(Mg_{1/3}Nb_{2/3})O_3\text{-}0.34PbTiO_3$	50	20	3.1	90	109
$0.92Pb(Tm_{0.5}Nb_{0.5})O_3{-}0.08Pb(Mg_{1/3}Nb_{2/3})O_3$	310	17.03	3.12		136
$(Pb_{0.87}Ba_{0.1}La_{0.02})(Zr_{0.68}Sn_{0.24}Ti_{0.08})O_3$	180	58.2	3.2		151
$Pb_{0.97}La_{0.02}(Zr_{0.50}Sn_{0.46}Ti_{0.04})O_3$	150	43	3.2	86.5	124
$0.55(Pb_{0.97}La_{0.02})(Zr_{0.93}Sn_{0.05}Ti_{0.02})O_3{-}0.45(Pb_{0.93}Ba_{0.04}La_{0.02})\ (Zr_{0.65}Sn_{0.3}Ti_{0.05})O_3$	180	25	3.2	74.4	160
$Pb_{0.97}La_{0.02}(Zr_{0.56}Sn_{0.35}Ti_{0.09})O_3$	175	39.4	3.3	80	166
$(Pb_{0.895}La_{0.07})(Zr_{0.9}Ti_{0.1})O_3$	175	42.3	3.38	86.5	115
$0.9PbHfO_3{-}0.1Pb(Mg_{0.5}W_{0.5})O_3$	155	43.5	3.7	72.5	134
$Pb_{0.94}La_{0.04}(Lu_{0.5}Nb_{0.5})O_3$	681		3.85		137
$(Pb_{0.955}La_{0.03})(Zr_{0.50}Sn_{0.42}Ti_{0.08})O_3$	180	41	3.99	79.2	127
$Pb_{0.97}La_{0.02}(Zr_{0.60}Sn_{0.35}Ti_{0.05})O_3$	200	34.48	4.1		121
$(Pb_{0.97}La_{0.02})(Zr_{0.5}Sn_{0.44}Ti_{0.06})O_3$	250	29.3	4.2	82	117
$(Pb_{0.97}La_{0.02})(Zr_{0.5}Sn_{0.44}Ti_{0.06})O_3$	250	29.3	4.2	82	118
$Pb_{0.955}La_{0.03}(Zr_{0.5}Sn_{0.43}Ti_{0.07})O_3$	200	36	4.2	78	126
$(Pb_{0.97}La_{0.02})(Zr_{0.8}Sn_{0.145}Ti_{0.055})O_3$	225	34	4.38	73	124
$(Pb_{0.858}Ba_{0.1}La_{0.02}Y_{0.008})(Zr_{0.65}Sn_{0.3}Ti_{0.05})O_3\text{-}\ (Pb_{0.97}La_{0.02})(Zr_{0.9}Sn_{0.05}Ti_{0.05})O_3$	200	46.8	4.65	60	152
$La_{0.02}Pb_{0.97}[(Yb_{0.5}Nb_{0.5})_{0.92}Ti_{0.08}]O_3$	240	34	5.18	65	135
$(Pb_{0.97}La_{0.02}Zr_{0.85}Sn_{0.12}Ti_{0.03}O_3){-}0.5$ wt % Al_2O_3	315	35.5	5.3	88.3	72
$(Pb_{0.955}Sr_{0.015}La_{0.02})(Zr_{0.75}Sn_{0.195}Ti_{0.055})O_3$	350	33.5	5.56	70	156
$Pb_{0.97}La_{0.02}(Zr_{0.5}Sn_{0.45}Ti_{0.05})O_3$	400	36.2	5.6	63	116
$(Pb_{0.858}Ba_{0.1}La_{0.02}Y_{0.008})(Zr_{0.65}Sn_{0.3}Ti_{0.05})O_3{-}(Pb_{0.97}La_{0.02})(Zr_{0.9}Sn_{0.05}Ti_{0.05})O_3$	306	48.5	6.4	62.4	173
$Pb[(Lu_{0.5}Nb_{0.5}){-}(Mg_{0.5}W_{0.5})]O_3$	340	46	6.4	71	132
$Pb_{0.91}La_{0.06}(Zr_{0.552}Sn_{0.368}Ti_{0.08})O_3@1$ wt $\%PbO{-}B_2O_3{-}SiO_2{-}Al_2O_3{-}ZnO{-}MnO_2$	380	43	7.4	91.6	77
$PbHfO_3$	270	44.5	7.6	80.8	133
$Pb_{0.98}La_{0.02}(Hf_{0.45}Sn_{0.55})_{0.995}O_3$	380	36	7.63	94	138
$(Pb_{0.91}La_{0.06})(Zr_{0.96}Ti_{0.04})O_3{-}1.0$ mol % $MnCO_3$	300	43.5	7.65	87	145
$(Pb_{0.98}La_{0.02})(Zr_{0.55}Sn_{0.45})_{0.995}O_3$	400	41.5	10.4	87	131
$(Pb_{0.94}La_{0.02}Sr_{0.04})(Zr_{0.9}Sn_{0.1})_{0.995}O_3$	400	44	11.18	82.2	130

[a] t of the bulk ceramics is commonly >0.1 mm.

$$V_c = \frac{V_{ext}}{\left[1 + \frac{\varepsilon_c}{\varepsilon_d}\left(\frac{td}{tc} - 1\right)\right]} \tag{15}$$

where V_c and V_{ext} are the voltage applied cross the cavity pore and external applied voltage, ε_c and ε_d are the permittivity of the cavity and the dielectric, respectively,[59,60] and *td* and *tc* are the thicknesses of the dielectric and cavity, respectively. Thus, the local E increases markedly for materials with larger pores and pore volumes, resulting in lower BDS.

High density electroceramic materials are commonly obtained by optimization of the sintering conditions, including sintering temperature/time and heating/cooling rate. For ceramics that are difficult to densify using a conventional approach, sintering aids are often added.[61−64] Higher density ceramics may be obtained by the addition of ZnO,[65] CuO,[66] and MgO,[62] which enhances BDS and W_{rec}. For $K_{0.5}Na_{0.5}NbO_3{-}Bi(Mg_{2/3}Nb_{1/3})O_3$ (KNN−BMN), small amounts of CuO help densify ceramics through the formation of a transient liquid phase, as reported by Qu and co-workers (Figure 5).[64] The sintering temperature was also reduced from 1150 to 930 °C, allowing compatibly with Cu or Ag/Pd internal electrode in MLs and giving rise to $W_{rec} \sim 4.02$ J cm^{-3} at 400 kV cm^{-1} for 0.9KNN-0.1BMN with 1% mol CuO.[66]

Different sintering technologies, such as spark plasma sintering (SPS), two-step sintering,[67] and the formation of coatings using chemical methods,[68−81] have also been shown to improve density and give rise to higher BDS and W_{rec}.

2.3.4. Grain Size.

The effect of grain size (G) on energy storage properties has been discussed for several electroceramics because of the relationship between BDS and G, expressed in eq 16

$$\text{BDS} \propto (G)^{-a} \tag{16}$$

where a is the exponent values being in the range of 0.2−0.4.[31,82−84] Waser explained that leakage current in fine-G ceramics is lower than coarse-G ceramics due to the high grain boundary density which act as barriers for charge carriers.[85] Thus, dielectric materials with high density and fine-G are required to optimize energy storage. G may be tailored by chemical doping and the formation of solid solution. It may also be modified by the application of an ultrathin coating on the primary particles prior to sintering via chemical coating methods, e.g., SiO_2 on BT ceramics.[67,77,86−89] The optimization on E_{max} and W_{rec} via grain size-engineering for several materials is illustrated in Figure 6.

For example, an average $G \sim 10\ \mu m$ was reported for BF−BT ceramics, which was reduced to $<2\ \mu m$ after A-site Nd doping, as shown in Figure 7. Meanwhile, improved $W_{rec} \sim 1.8$ J cm^{-3} and $\eta \sim 88\%$ were obtained for 15 mol % Nd−BF−BT and 40 mol % Nd−BF−BT, respectively.[90] Similar optimization behavior has also been found in KNN−BMN and KNN−ST ceramics, resulting in BDS ∼ 400 kV cm^{-1} and $W_{rec} > 3.5$ J cm^{-3}.[91,92]

2.3.5. Core−Shell Structure. Core−shell subgrain microstructures are observed in many lead-free ceramics, due to either kinetic limitations of the diffusion process (typical for BT based ceramics) or immiscibility on cooling from high temperature for perovskite end members with dissimilar ion size and bonding (BF based ceramics).[22,34,45] The effect of core−shell microstructures on energy storage performance is still unclear. In BT-based ceramics, the cores are often more conducting than the doped shells and core to core conductive pathways lead to breakdown.[93−96] For BF based ceramics, the defect chemistry of the cores and shells remains to be elucidated, but initial work suggests that further dopants are needed to create electrical homogeneity and thus eliminate the conducting pathways.[34,45] The theoretical modeling has reported a positive influence of core−shell microstructure but none have been unambiguously validated experimentally.[97]

3. STATE-OF-THE-ART IN ELECTROCERAMICS FOR ENERGY STORAGE

3.1. Bulk Ceramics

3.1.1. Lead-Based Ceramics. Lead-based ceramics are used commercially as energy storage materials for high-power pulsed capacitors due to their excellent W_{rec} and η.[98−101] The energy storage properties of RFE and AFE lead-based ceramics are summarized in Table 3.

3.1.1.1. Lead-Based Relaxor-Ferroelectrics. Many lead-based RFEs, including $Pb(Mg_{1/3}Nb_{2/3})O_3$−$PbTiO_3$ (PMN−PT), $Pb(Zn_{1/3}Nb_{2/3})O_3$−$PbTiO_3$ (PZN−PT), and $(Sr,Pb,Bi)TiO_3$ (SPBT)-based materials, have been reported as potential candidates for energy storage capacitors.[102−110] Zhang and co-workers investigated the relaxation behavior and energy storage properties of $(1-x)$PMN−xPT ceramic, obtaining $W_{rec} \sim 0.47$ J cm^{-3} at room temperature.[102] Li and co-worker probed the effect of domain structure on W_{rec} and thermal stability of $0.2PMN-0.8Pb(Sn_xTi_{1-x})O_3$ ($PMN-PS_xT_{1-x}$) ceramics, as illustrated in Figure 8. 0.2PMN−0.8PST ceramics exhibited $W_{rec} \sim 0.85$ J cm^{-3} with excellent thermal stability which was attributed to the coexistence of ferroelectric domains and PNRs.[111]

3.1.1.2. Lead-Based Antiferroelectrics. $PbZrO_3$ (PZ) is the first known AFE and exhibits a double $P-E$ hysteresis loop below T_C. However, the high critical switching field required for an AFE−FE phase transition at room temperature limits applications for energy storage. Chemical substitution to reduce switching field is an effective strategy to overcome the problem and three well-known $PbZrO_3$ based compositions are reviewed: (i) $(Pb,La)(Zr,Ti)O_3$ (PLZT);[112−115] (ii) $(Pb,La)(Zr,Sn,Ti)O_3$ (PLZST);[116−129] and (iii) $(Pb,La)(Zr,Sn)O_3$ (PLZS).[130,131] Additionally, some new AFEs have also been identified based on $PbHfO_3$, $Pb(Lu_{0.5}Nb_{0.5})O_3$, $Pb(Yb_{0.5}Nb_{0.5})O_3$, and $Pb(Tm_{0.5}Nb_{0.5})O_3$.[132−138]

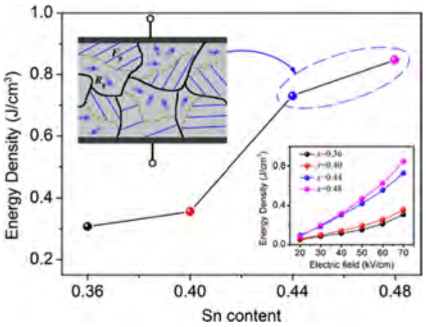

Figure 8. W_{rec} of $0.2PMN-0.8PS_xT_{1-x}$ ceramics with different Sn (x) contents at 70 kV cm^{-1}. The insets show the mechanism of enhanced energy storage due to coexistent-phase structure and the W_{rec} for $PMN-PS_xT_{1-x}$ ceramics under different electric fields. Reproduced with permission from ref 111. Copyright 2018 Elsevier.

3.1.1.2.1. $(Pb,La)(Zr,Ti)O_3$ (PLZT). According to the phase diagram (Figure. 9), PLZT exists as homogeneous compositions over a wide range of mol % La in the $PbZrO_3$−$PbTiO_3$ solid solution.[139,140]

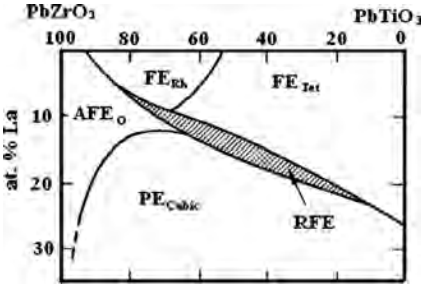

Figure 9. Phase diagram of PLZT at room temperature.[139] Reproduced with permission from ref 139. Copyright 2014 Elsevier.

When Pb ions are replaced by ≤30 mol % La on the A-site in accordance with a lead vacancy ($V_{pb}^{''}$) ionic compensation model, an orthorhombic AFE phase similar to $PbZrO_3$ occurs for Zr rich compositions. However, only PLZT with <10 mol % La is typically utilized for energy storage applications[141−147] since higher concentrations have lower polarization and therefore lower W_{rec}. Li and co-workers prepared $(Pb_{0.97}La_{0.02})(Zr_{0.95}Ti_{0.05})O_3$ ceramics via a solid-state reaction route, yielding $W_{rec} \sim 0.83$ J cm^{-3} and $\eta \sim 70\%$ under an electric field of 55 kV cm^{-1}.[114] Jo and co-workers found that AFE and RFE behavior can both be obtained by substitution of La and excess PbO in PLZT, resulting in the enhancement of W_{rec} by promoting a slim and slanted hysteresis loop. Both high $W_{rec} \sim 3.04$ J cm^{-3} and $\eta \sim 92\%$ were obtained along with no performance degradation after 10^5 cycles.[112] Tuning the Zr/Ti ratio has also shown to be an effective way to improve W_{rec} of PLZT ceramics. Qiao and co-workers reported slimmer $P-E$ loops giving a $W_{rec} \sim 3.38$ J cm^{-3} in $(Pb_{0.895}La_{0.07})(Zr_xTi_{1-x})O_3$ ceramics by changing the Zr/Ti ratio (Figure 10), which was attributed to the reduction of tolerance factor and "enhancement of antiferroelectricity".[115] Mn doping is also suggested to improve W_{rec} of PLZT by "enhancing antiferroelectricity".[143−145]

3.1.1.2.2. $(Pb,La)(Zr,Sn,Ti)O_3$ (PLZST). To further optimize the energy storage properties of PLZT ceramics, Sn may be substituted on the B-site of PLZT, which broadens the AFE compositional range,[72,77,87,116,122,148−166] in accordance with phase diagram from 1989 (Figure 11).[167] $(Pb_{0.97}La_{0.02})$-

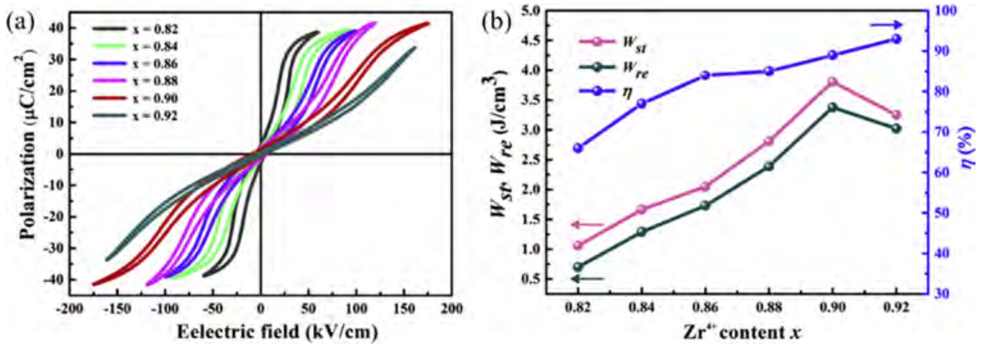

Figure 10. Effect of Zr/Ti ratio on P−E loops and energy storage properties of PLZT.[115] Reproduced with permission from ref 115. Copyright 2019 Elsevier.

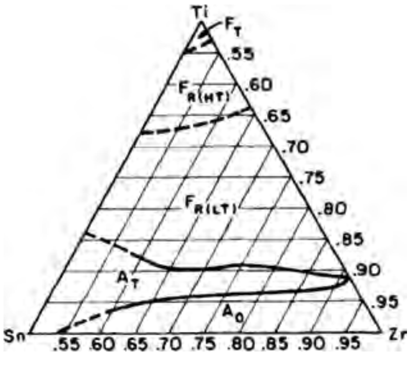

Figure 11. Phase diagram of $(Pb_{0.97}La_{0.02})(Zr,Sn,Ti)O_3$, where T, R, and O represent the tetragonal, rhombohedral, and orthorhombic structure, respectively, and HT and LT represent high and low temperature, respectively. Reproduced with permission from ref 167. Copyright 2005 John Wiley and Sons.

$(Zr,Sn,Ti)O_3$ with 2 mol % La has been most commonly studied in which the Zr/Ti/Sn ratio is varied to give a complex phase diagram that contains FE tetragonal (F_T), high-temperature nontilted FE rhombohedral ($F_{R(HT)}$), low temperature FE rhombohedral ($F_{R(LT)}$) AFE tetragonal (A_T), and AFE orthorhombic (A_O) phases.

We note that the A_T phase in both PLZT and PLZST has been shown to be incommensurate by a number of researchers and might be better described as a A_O phase in which there is disorder of antipolar coupling.[168−170] PLZST is AFE for concentrations with <15 mol % Ti. For compositions with A_O structure, the critical phase switching fields are above BDS but ceramics with the A_T phase undergo electric field-induced AFE-FE switching at room temperature, for which the switching field increases with increasing Sn concentration (Figure 12).[118] Adjusting the Zr/Sn/Ti ratio leads to optimization of W_{rec} in PLZST ceramics[116,118,148,157] with an increase in Sn concentration leading to a reduction in switching field (forward threshold electric field, E_F, and backward threshold electric field, E_B) and weakening ferroelectricity.[171] W_{rec} ~ 5.6 J cm^{-3} and high thermal stability have been obtained in PLZST ceramics with a Zr/Sn/Ti ratio of 0.5:0.45:0.05[116] while Wang and coworkers reported, in their study of the $(Pb_{0.97}La_{0.02})(Zr_{0.5}Sn_{0.5\text{-}x}Ti_x)O_3$ solid solution, superior W_{rec} of 4.2 J cm^{-3}

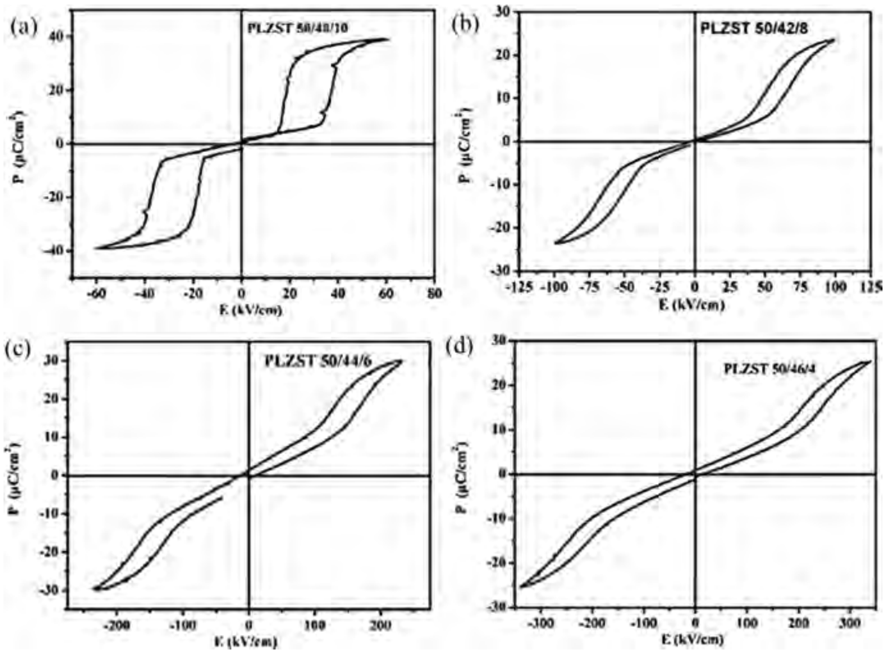

Figure 12. AFE-type P−E hysteresis loops of $Pb_{0.97}La_{0.02}(Zr_{0.5}Sn_{0.5-x}Ti_x)O_3$ with x = (a) 0.10, (b) 0.08, (c) 0.06, and (d) 0.04.[118] Reproduced with permission from ref 118. Copyright 2016 Elsevier.

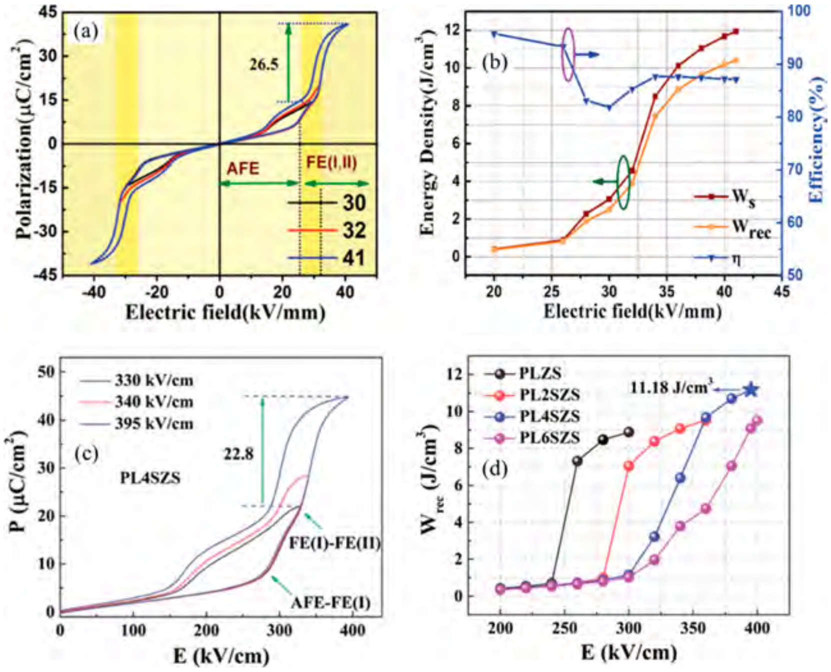

Figure 13. (a) Bipolar $P-E$ hysteresis loops and (b) energy storage properties of $(Pb_{0.98}La_{0.02})(Zr_{0.55}Sn_{0.45})_{0.995}O_3$ ceramics under different applied fields.[131] (c) Unipolar $P-E$ hysteresis loops of the $(Pb_{0.94}La_{0.02}Sr_{0.04})(Zr_{0.9}Sn_{0.1})_{0.995}O_3$ ceramic under different applied fields. (d) W_{rec} of $(Pb_{0.98\text{-}x}La_{0.02}Sr_x)(Zr_{0.9}Sn_{0.1})_{0.995}O_3$ with Sr concentration ($x = 0-0.06$) as a function of the E.[130] (a, b) Reproduced with permission from ref 131. Copyright 2019 John Wiley and Sons; (c, d) Reproduced with permission from ref 130. Copyright 2019 Royal Society of Chemistry.

Table 4. Energy Storage Properties of BT-Based Materials[a]

compd	E (kV cm^{-1})	ΔP (μC cm^{-2})	W_{rec} (J cm^{-3})	η (%)	ref
0.9BT−0.1BMN	143.5	∼16	1.13	95	192
$Ba_{0.85}Ca_{0.15}Zr_{0.1}Ti_{0.9}O_3$	200	∼15	1.153		182
$0.9BT-0.1(Bi_{0.9}Na_{0.1})(In_{0.8}Zr_{0.2})O_3$	180	∼20	1.33	88	202
$0.88(Ba_{0.8}Sr_{0.2})TiO_3-0.12\ Bi(Zn_{2/3}Nb_{1/3})O_3$	225	17	1.62	99.8	210
$0.9BT-0.1BMN-0.3$ wt % $MnCO_3$	205	16.28	1.7	88.5	191
$0.92(0.65BT-0.35NBT)-0.08(Na_{0.73}Bi_{0.09}NbO_3)$	172	∼25	1.7	82	194
$0.92(0.92BT-0.08K_{0.5}Bi_{0.5}TiO_3)-0.08NN$	220	∼23	1.96	67.4	207
$0.88BT-0.12Bi(Li_{0.5}Nb_{0.5})O_3$	270	∼19	2.03	88	197
$0.9BT-0.1Bi(Li_{0.5}Ta_{0.5})O_3$	280	∼11.9	2.2	88	203
$0.85BT-0.15Bi(Zn_{0.5}Sn_{0.5})O_3$	280	∼23	2.41	91.6	205
$0.9BT-0.1Bi(Zn_{0.5}Zr_{0.5})O_3$	264	∼25	2.46		199
$0.85BT-0.15Bi(Mg_{0.5}Zr_{0.5})O_3$	280	∼23	2.9	86.8	204
$0.9Ba_{0.65}Sr_{0.35}TiO_3-0.1BMN$	400	23	3.34	85.71	211
$0.65(Ba_{0.98}Li_{0.04})Ti_{0.98}O_3-0.35(Sr_{0.7}Bi_{0.2})TiO_3$	410	35	3.54	77	212
$0.6BT-0.4Bi(Mg_{0.5}Ti_{0.5})O_3$	340	∼40	4.49	93	208
$BT-0.06Bi_{2/3}(Mg_{1/3}Nb_{2/3})O_3$	520	25	4.55	91	209

[a] t of the bulk ceramics is commonly >0.1 mm.

with η of 82% for $(Pb_{0.97}La_{0.02})(Zr_{0.5}Sn_{0.44}Ti_{0.06})O_3$ ceramics with good temperature stability.[118] Recently, a ferrielectric (FIE) configuration was reported in PLZST which consists of ferroelectric ordering segments with either magnitude or angular modulation of dipoles.[172] The net polarization of field-induced FE order can be tailored by adjusting the Sn/Ti ratio.

The performance of PLZST ceramics is also influenced by the Pb/La ratio.[117,122,126] The AFE phase becomes more stable with a commensurate increase in the AFE−FE switching field as La concentration increases. The energy storage properties of $(Pb_{1-1.5x}La_x)(Zr_{0.5}Sn_{0.43}Ti_{0.07})O_3$ ceramics were optimized (W_{rec} of 4.2 J cm^{-1}) by Dan and co-workers for compositions with $x = 0.03$ due to a large switching electric field and high BDS.[3,126] Furthermore, doping with Ba and Sr (A-site) improves fatigue behavior and temperature stability, suppresses the stress sensitivity, and enhances energy storage.[148,150−153,155,161,173]

3.1.1.2.3. (Pb,La)(Zr,Sn)O$_3$ (PLZS). Wang and co-workers reported a unique E-induced multiphase transition in PLZS for which a conventional AFE−FE phase transition at low E, followed by a second FE-FE phase transition at a higher E, leads to an increase in polarization.[131] W_{rec} of 10.4 J cm^{-3} and η of 87% were achieved at 400 kV cm^{-1} for $(Pb_{0.98}La_{0.02})(Zr_{0.55}Sn_{0.45})_{0.995}O_3$ ceramics, along with superior discharge current density of 1640 A cm^{-2} and ultrafast discharge speed (75 ns discharge period) (Figure 13a,b).[131] Subsequently, a record-high $W_{rec}\sim$ 11.2 J cm^{-3} and a high $\eta\sim$ 82% were realized in $(Pb_{0.98-x}La_{0.02}Sr_x)(Zr_{0.9}Sn_{0.1})_{0.995}O_3$ ceramics, as illustrated in (Figure 13c,d). The substitution of Pb by Sr gave rise to an increase in BDS and AFE/FE switching fields, leading to further enhancement of energy storage performance.[130]

3.1.2. Lead-Free Ceramics. In the last decades, extensive research has focused on lead-free electroceramics due to concerns over the toxicity of lead/lead oxide-based compounds.[174−176] As a result, there has been a steady but continuous improvement in their energy storage performance,[31,103,177−180] with a view to replacing existing lead-based materials. Several lead-free ceramic systems are considered as potential candidates to replace PLZT for energy storage applications, including those based on BT, ST, KNN, BF, NBT, $AgNbO_3$ (AN), and NN.

3.1.2.1. $BaTiO_3$-Based Ceramics. BT-based dielectric ceramics have been studied for decades and dominate the commercial market of ceramic capacitors.[81,181] Several studies have reported improvements in energy storage performance of BT-based ceramics through (i) substituting oxides to improve BDS, such as Al_2O_3, La_2O_3, MgO, SiO_2;[79,80,182−184] (ii) employing different sintering techniques, such as SPS, citrate precursor, and cold sintering (CS) to increase ceramic density or control grain growth;[68,76,185] (iii) adding sintering aids such as $ZnNb_2O_6$ and $NiNb_2O_6$ to increase density;[186,187] (iv) introducing further end-members in the solid solution, $Bi(Mg_{1/2}Ti_{1/2})O_3$,[188,189] $BiYbO_3$,[190] BMN,[191−193] NBT−$Na_{0.73}Bi_{0.09}NbO_3$,[194] $Nd(Zn_{1/2}Ti_{1/2})O_3$,[195] $Bi(Zn_{2/3}Nb_{1/3})O_3$,[196] $Bi(Li_{1/2}Nb_{1/2})O_3$,[197,198] $Bi(Zn_{1/2}Zr_{1/2})O_3$,[199] $Bi(Zn_{1/2}Ti_{1/2})O_3$,[200] $YNbO_4$,[201] $Bi_{0.9}Na_{0.1}In_{0.8}Zr_{0.2}O_3$,[202] $Bi(Li_{1/2}Ta_{1/2})O_3$,[203] $Bi(Mg_{1/2}Zr_{1/2})O_3$,[204] $Bi(Zn_{1/2}Sn_{1/2})O_3$,[205] $K_{0.5}Bi_{0.5}TiO_3$−$KNbO_3$,[206] and $K_{0.5}Bi_{0.5}TiO_3$−NN[207] to promote RFE behavior. The energy storage properties of BT-based materials are summarized in Table 4.

The most effective approach, however, is the introduction of a Bi-based perovskite end member in which the B-site contains multiple cations. Doping with a Bi ion that has a lone pair electronic $6s^2$ configuration into the Ba-site increases P_{max}. P_r is minimized by forming a so-called "weakly coupled relaxor" state in which long-range polar coupling is disrupted by the multiple B-site ions which have different valence and ionic radius to Ti. Using this principle, Hu and co-workers[208] reported high W_{rec} of 4.49 J cm^{-3} with a η of 93% for 0.6BT−0.4 $Bi(Mg_{0.5}Ti_{0.5})O_3$ (BT−BMT) ceramics that were temperature stable to 170 °C (variation W_{rec} < 5% and η < 4%).

Of greater commercial potential, Yang and co-workers reported similar properties with BT−0.06 $Bi_{2/3}(Mg_{1/3}Nb_{2/3})O_3$ (BT−$0.06B_{2/3}$MN) but in compositions compatible with Ag/Pd electrodes due to the presence of only 4 mol % Bi on the A-site.[209] Similar energy storage properties, W_{rec} ∼ 4.6 J cm^{-3} and η ∼ 92% (Figures 14a,b) to BT−BMT were obtained for BT−$0.06B_{2/3}$MN ceramics which also benefited from the highest BDS, ∼520 kV cm^{-1}, among all reported BT-based compositions.[209] BT−$0.06B_{2/3}$MN is not electrically homogeneous but BDS and W_{rec} were still optimized by reducing, though not completely eliminating, the difference between the bulk and grain boundary responses with respect to undoped BT, Figures 14c,d.[209]

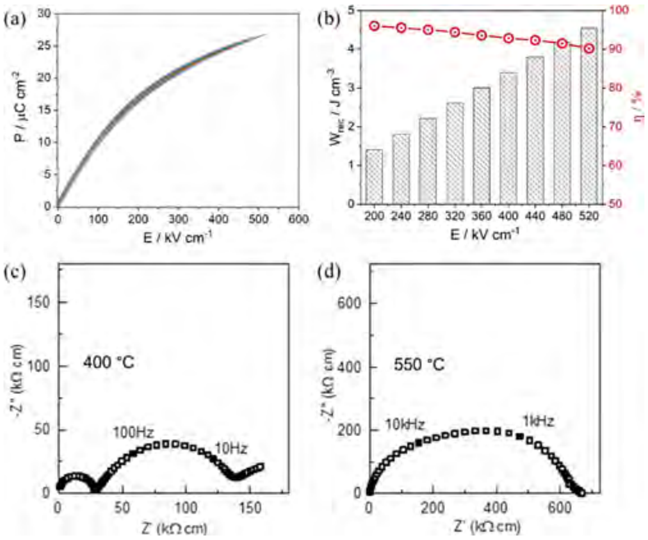

Figure 14. (a) Unipolar P−E loops under E_{max} and (b) calculated W_{rec} and η at different electric field for BT−$0.06B_{2/3}$MN ceramics. (c) Z^* plots of (c) BT at 400 °C and (d) BT−$0.06B_{2/3}$MN at 550 °C.[209] Reproduced from ref 209. Copyright 2020 American Chemical Society.

3.1.2.2. $SrTiO_3$-Based Ceramics. ST, which is an incipient ferroelectric, is considered as a promising candidate for energy storage applications due to its relatively high permittivity (ε_r ∼ 300) and low dielectric loss (<1%) at room temperature. Extensive efforts have been made to improve the energy storage performance of ST-based ceramics, including (i) doping with Ba,[213−216] Dy,[217] Mg,[218] Ce,[64] and Bi[219−222] on the A-site or Mn[223] and Sn[224,225] on the B-site; (ii) using sintering aids, such as ZnO,[65] MgO,[226−228] SiO_2,[63,229] SrO−B_2O_3−SiO_2,[230] ZnO−Li_2O,[231] Bi_2O_3−B_2O_3−SiO_2,[232] B_2O_3−SiO_2−Bi_2O_3−CaO−BaO,[233] Al_2O_3,[234] BaO−TiO_2−SiO_2,[75] $BaCu(B_2O_5)$,[235] and $NiNb_2O_6$;[236] (iii) employing different sintering techniques such as microwave sintering[73,75] and SPS;[70] and (iv) introducing complex end-members, such as NBT,[237,238] NBT−$Ba(Al_{0.5}Nb_{0.5})O_3$,[239] NBT−BT,[118,240,241] and $Bi(Mg_{0.5}Hf_{0.5})O_3$.[242] The energy storage properties of ST-based materials are summarized in Table 5.

From a review of the literature, doping commonly increases both ε_r and P_{max} but decreases the BDS, sintering aids increase BDS but lower the P_{max}. The highest energy densities have therefore been achieved through either dopants and/or alloying with "relaxor end-members" which also act as sintering aids. Adopting these protocols, a W_{rec} of 3.1 J cm^{-3} with η ∼ 93% was obtained for $0.9(Sr_{0.7}Bi_{0.2})TiO_3$−0.1 $Bi(Mg_{0.5}Hf_{0.5})O_3$ ceramic at 360 kV cm^{-1}, Figures 15a,b,[242] which was also fatigue-resistant up to 10^5 cycles and temperature stable from 25 to 200 °C, Figures 15c−f.[242]

3.1.2.3. $K_{0.5}Na_{0.5}NbO_3$-Based Ceramics. In 2016, the energy storage properties of KNN−(Bi,Na)HfO_3 solid solutions were first investigated, and W_{rec} ∼ 0.54 J cm^{-3} was achieved at 129 kV cm^{-1}.[249] ZnO and CuO were introduced as sintering aids improved W_{rec} in KNN-based ceramics[66,250] by decreasing porosity and restricting grain growth. BDS of 400 kV cm^{-1} was obtained in 0.8KNN-0.2$Sr(Sc_{0.5}Nb_{0.5})O_3$ ceramic with 0.5 mol % ZnO[250] and CuO reduced the sintering temperature and enhanced the density of 0.9KNN−0.1BMN ceramics.[66] A third perovskite end-member, e.g., ST, BF, and BMN, has also been shown to optimize energy storage properties.[91,92,251] W_{rec} of 4.03 J cm^{-3} at 400 kV cm^{-1} was obtained in 0.85KNN−0.15ST bulk ceramics[92] with similar energy storage performance realized in 0.90KNN−0.10BMN ceramic with a large P_{max} (41 μC cm^{-2}) obtained at 300 kV cm^{-1}, Figure 16.[91] The energy storage properties of KNN-based materials are summarized in Table 6.

3.1.2.4. $BiFeO_3$-Based Ceramics. BF-based ceramics are best known as multiferroics but have also been explored for high-temperature ferroelectric and piezoelectric applications due to

https://doi.org/10.1021/acs.chemrev.0c01264
Chem. Rev. XXXX, XXX, XXX−XXX

Table 5. Energy Storage Properties of ST-Based Materials[a]

compounds	E (kV cm^{-1})	ΔP (μC cm^{-2})	W_{rec}(J cm^{-3})	η (%)	ref
95 wt % $Ba_{0.4}Sr_{0.6}TiO_3$−5 wt %MgO	300	11.88	1.5	88.5	227
$Ba_{0.4}Sr_{0.6}TiO_3$−8 mol % SiO_2	400	9.11	1.6	90.9	229
0.6ST−0.4NBT	210	~20	1.7	69.93	237
0.45ST−0.2NBT−0.35BT	170	~25	1.78	77.06	243
$(Sr_{0.99}Mg_{0.01})TiO_3$	362	~12	1.86	89.3	218
0.5ST−0.5(0.94 $Bi_{0.54}Na_{0.46}TiO_3$−0.06BT)	180	~30	1.88	79	239
0.5ST−0.5(0.95NBT−0.05$BaAl_{0.5}Nb_{0.5}O_3$)	190	~28	1.89	77	240
$Ba_{0.4}Sr_{0.6}TiO_3$−9 wt %(Bi_2O_3−B_2O_3−SiO_2)	279	~17	1.98	90.57	232
0.95($Sr_{0.5}Na_{0.25}Bi_{0.25}TiO_3$)−5 wt %MgO−0.05$KNbO_3$	178.5	~27	2	76.34	244
$Ba_{0.4}Sr_{0.6}(Ti_{0.996}Mn_{0.004})O_3$−2 wt % MgO	300	~16	2.014	88.6	228
$Ba_{0.3}Sr_{0.6}Ca_{0.1}TiO_3$−2 wt %MgO	194.33	~23	2.223		245
$Sr_{0.985}Ce_{0.01}TiO_3$−3 wt % SiO_2	290	~10	2.23		64
$SrTi_{0.985}(Zn_{1/3}Nb_{2/3})_{0.015}O_3$−4.5 wt %$ZnNb_2O_6$	422	9.34	2.35	77	246
0.9ST−0.1($Bi_{0.48}La_{0.02}Na_{0.48}Li_{0.02}Ti_{0.98}Zr_{0.02}O_3$)	323	~20	2.59	85	247
0.8ST−0.2(NBT− $Ba_{0.94}La_{0.04}Zr_{0.02}Ti_{0.98}O_3$)	320	~22	2.83	85	248
0.995(0.6ST−0.4NBT)−0.005ZrO_2	285	~25	2.84	71.54	74
0.9($Sr_{0.7}Bi_{0.2}$)TiO_3−0.1 Bi($Mg_{0.5}Hf_{0.5}$)O_3	360	~22	3.1	93	242
$Ba_{0.3}Sr_{0.7}TiO_3$−1.6 wt % ZnO	400		3.9		65
98.5 wt %$Ba_{0.4}Sr_{0.6}TiO_3$−1.254 wt %Al_2O_3−0.246 wt %SiO_2	493		5.09		234

[a] The t of the bulk ceramics is commonly >0.1 mm.

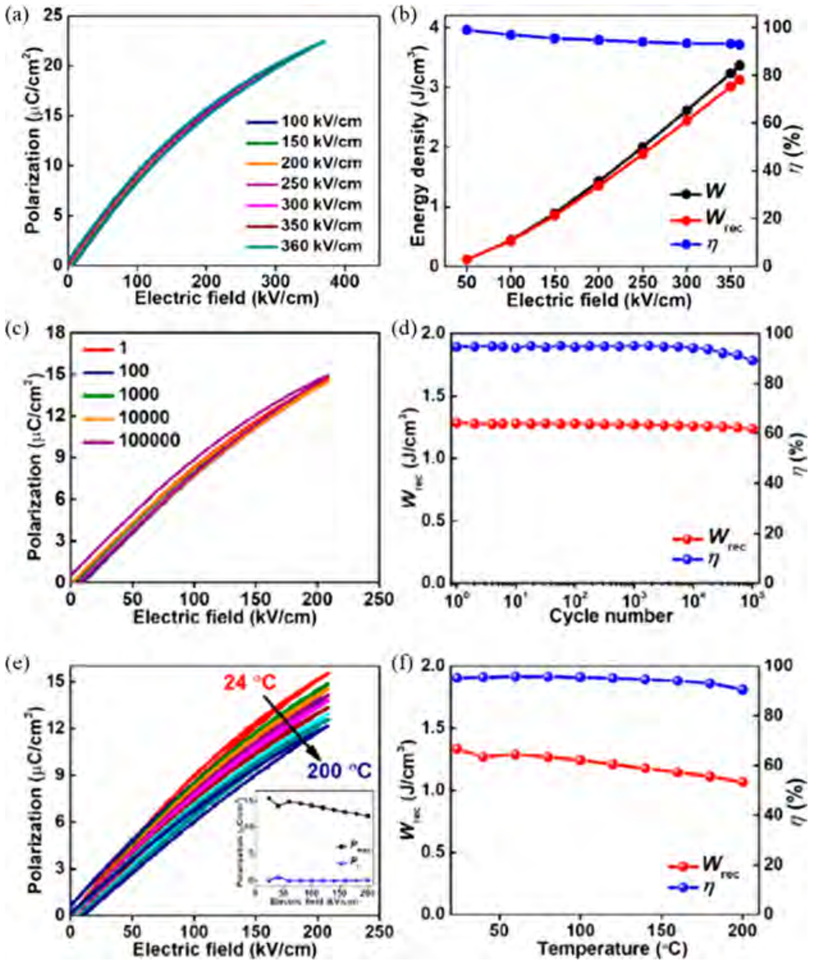

Figure 15. (a) Unipolar P−E loops and (b) W, W_{rec}, and η of 0.9($Sr_{0.7}Bi_{0.2}$)TiO_3−0.1Bi($Mg_{0.5}Hf_{0.5}$)O_3 ceramic as functions of E. (c) Unipolar P−E loops and (d) W_{rec} and η of 0.9($Sr_{0.7}Bi_{0.2}$)TiO_3−0.1Bi($Mg_{0.5}Hf_{0.5}$)O_3 ceramic as functions of cycle numbers up to 10^5. (e) Unipolar P−E loops, with the inset shows the P_{max} and P_r as functions of temperature, and (f) W_{rec} and η of 0.9($Sr_{0.7}Bi_{0.2}$)TiO_3−0.1Bi($Mg_{0.5}Hf_{0.5}$)O_3 ceramics as a function of temperature. Reproduced with permission from ref 242. Copyright 2019 John Wiley and Sons.

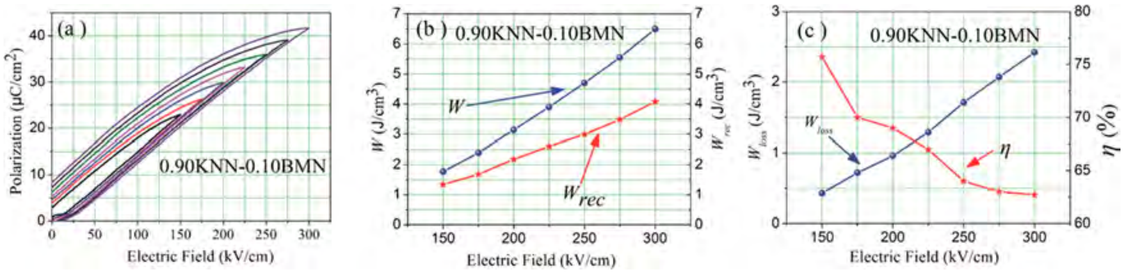

Figure 16. (a) Unipolar $P-E$ hysteresis loops and (b) calculated W and W_{rec} and (c) W_{loss} and η for 0.90KNN−0.10BMN ceramics under different E. Reproduced with permission from ref 91. Copyright 2017 Royal Society of Chemistry.

Table 6. Energy Storage Properties of KNN-Based Materials[a]

compounds	E (kV cm^{-1})	ΔP (μC cm^{-2})	W_{rec} (J cm^{-3})	η (%)	ref
$(K_{0.48}Na_{0.52})_{0.88}Bi_{0.04}NbO_3$	189	~12.7	1.04		252
0.93KNN−0.07BMN	150	~22.5	1.3	58.8	253
0.9KNN−0.1BF	206	23.7	2	61	251
0.8KNN−0.2Sr$(Sc_{0.5}Nb_{0.5})O_3$−0.5%ZnO	400	~11.6	2.6	73.2	250
$K_{0.14}Bi_{0.12}Na_{0.5}NbO_3$−1 mol % CuO	300	29	2.89	80	254
0.85KNN-0.15 Bi$(Zn_{0.5}Zr_{0.5})O_3$	325	30	3.5	86.8	255
0.9KNN−0.1BMN−1.0 mol % CuO	400	~21	4.02	57.3	66
0.85KNN−0.15ST	400	~26	4.03	~52	92
0.9KNN−0.1BMN	300	~34	4.08	~62.7	91

[a] t of the bulk ceramics is commonly >0.1 mm.

Table 7. Energy Storage Properties of BF-Based Materials[a]

compounds	E (kV cm^{-1})	ΔP (μC cm^{-2})	W_{rec} (J cm^{-3})	η (%)	ref
3 mol % Nb_2O_5−0.65BF−0.35BT	90	19	0.71		265
0.61BF−0.33BT−0.06Ba$(Mg_{2/3}Nb_{1/3})O_3$	125	32.3	1.56	75	269
0.61BF−0.33BT−0.06La$(Mg_{0.5}Ti_{0.5})O_3$	130	33.3	1.66	82	267
0.6BF−0.34BT−0.06Sr$(Al_{0.5}Nb_{0.5})O_3$	150	35	1.75	81	270
15%Nd−0.70BF−0.30BT	170	30.7	1.82	41.3	90
0.65BF-0.30BT−0.05Ba$(Zr_{0.5}Zn_{0.5})O_3$	190	32	2.04	54	34
0.65BF−0.30BT−0.05Bi$(Zn_{2/3}Nb_{1/3})O_3$	180	32.8	2.06	53	266
0.56BF−0.30BT−0.14AN	195	26	2.11	84	268
0.60BF−0.30BT−0.10Nd$(Mg_{2/3}Nb_{1/3})O_3$	220	24	2.4	77	34
0.7(0.67BF−0.34BT)−0.3$(Sr_{0.7}Bi_{0.2})TiO_3$	180	37	2.4	90.4	271
0.62BF−0.3BT−0.08Nd$(Zr_{0.5}Zn_{0.5})O_3$	240	26	2.45	72	34
0.6BF−0.34BT−0.06Ba$(Zn_{0.5}Ta_{0.5})O_3$	160	41	2.56	71	272
$0.67Bi_{0.9}Sm_{0.1}FeO_3$−0.33BT	200	48	2.8	55.8	273
$0.25Bi_{0.83}Sm_{0.17}Fe_{0.95}Sc_{0.05}O_3$−0.75[0.85BT-0.15Bi$(Mg_{0.5}Zr_{0.5})O_3$]	206	36	3.2	92	274
0.61BF−0.33BST−0.06La$(Mg_{2/3}Nb_{1/3})O_3$	230	36.5	3.38	59	275
0.57BF−0.30BT−0.13 Bi$(Li_{0.5}Nb_{0.5})O_3$	280	30	3.64	74	276
0.57BF−0.33BT−0.10NN	360	51	8.12	90	42
0.5BF−0.4ST−0.1BMN-0.03Nb	460	45	8.2	74.1	45

[a] The t of the bulk ceramics is commonly >0.1 mm.

their high T_C and large spontaneous polarization.[256−259] Compared with other lead-free ceramics, BF-based were not initially considered as good candidates for energy storage applications due to their high leakage current.[260] p-type electrical conductivity due to the volatilization of Bi and the variation of Fe valence states has been reported frequently in BF system, which limits the BDS and restricts energy density.[261−263] However, the introduction of dopants and alloying with end-members suppresses the leakage current, reduces the electrical conductivity, increases intrinsic E_g and induces transitions from a FE to RFE state. The energy storage properties of BF-based materials are summarized in Table 7.

BF−BT-based materials are purported as potential energy storage compositions due to their excellent BDS and high P_{max}.[34,45,90] Undoped BF−xBT ceramics exhibit optimized ferroelectric and piezoelectric properties in a mixed-phase region of $0.25 \leq x \leq 0.35$.[264] The majority of studies have focused on this region and modified compositions either by (i) A and/or B-site chemical doping, including Nd, Nb, $Zn_{0.5}Zr_{0.5}$, $Zn_{2/3}Nb_{1/3}$, and $Li_{0.5}Nb_{0.5}$ or (ii) alloying with a third end-member, such as Nd$(Zn_{0.5}Zr_{0.5})O_3$, Nd$(Mg_{2/3}Nb_{1/3})O_3$, La$(Mg_{0.5}Ti_{0.5})O_3$, Ba$(Mg_{1/3}Nb_{2/3})O_3$, AN, and NN.[34,43,90,265−269]

The importance of electrical homogeneity was first postulated in 2019 by Wang, Reaney, and co-workers as a key factor to optimize BDS as well as W_{rec}.[34] Two electrical components with

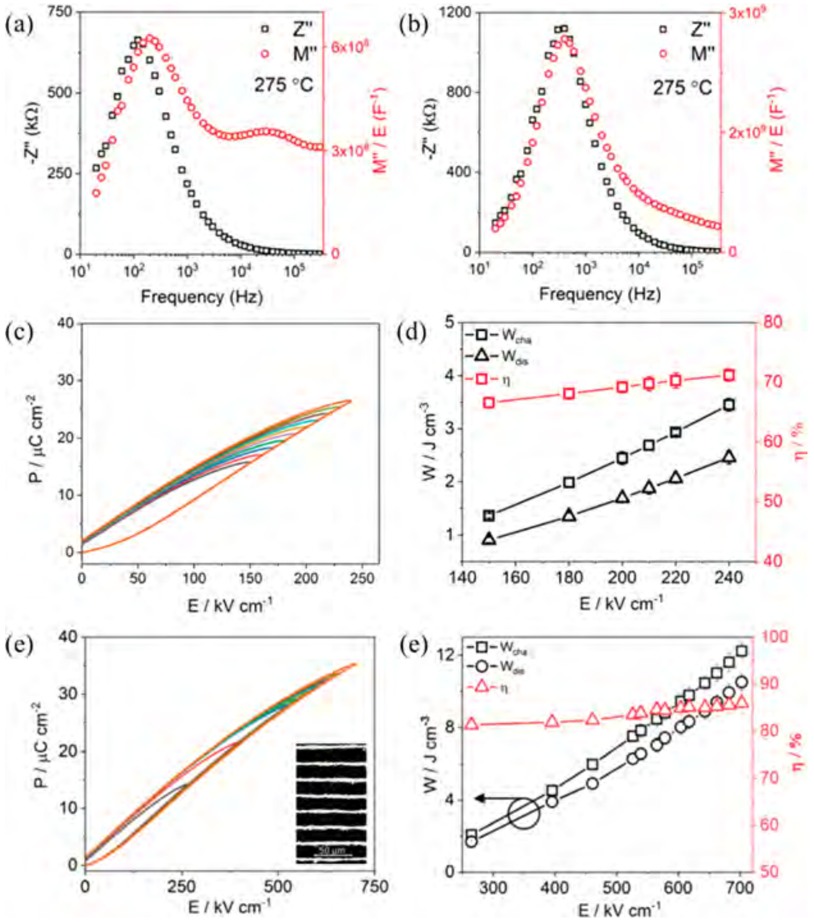

Figure 17. Combined Z'' and M'' spectroscopic plots at 275 °C for (a) BF−BT and (b) BF−BT−0.08NZZ. Unipolar P−E loops of BF−BT−0.08NZZ (c) bulk ceramics and (e) ceramic MLs, with cross-section SEM image as shown in inset figure. Calculated energy storage properties of BF−BT−0.08NZZ (d) bulk ceramic and (e) ceramic MLs. Reproduced from ref 34. Copyright 2019 Royal Society of Chemistry.

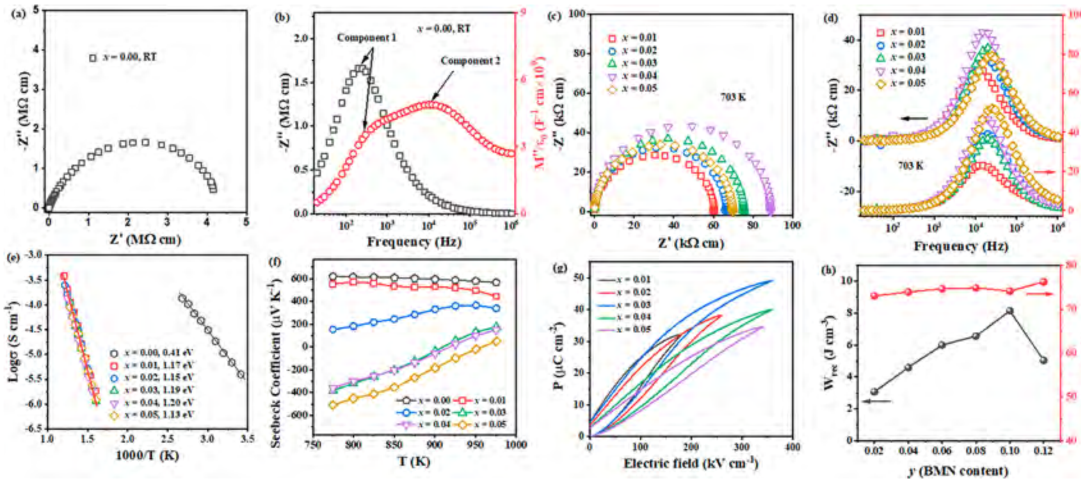

Figure 18. (a) Z^* plots and (b) Combined Z'' and M'' spectroscopic plots of 0.54BF−0.4ST−0.06BMN−xNb (x = 0); (c) Z^* plots and (d) Combined Z'' and M'' spectroscopic plots of x = 0.01−0.05; (e) Arrhenius plots, (f) Seebeck coefficients, and (g) unipolar P−E loops under E_{max} of x = 0.01−0.05. (h) W_{rec} and η of (0.6−y)BF−0.4ST−0.03Nb−yBMN. Reproduced from ref 45. Copyright 2020 Royal Society of Chemistry.

similar capacitance value, $C \sim 8 \times 10^{-10}$ F cm^{-1} and 1.4×10^{-9} F cm^{-1}, were found in 0.7BF−0.3BT ceramics, as illustrated Figure 17a,b. However, the associated resistances, $R_1 \sim 3.8$ kΩ cm and $R_2 \sim 1.3$ MΩ cm, were vastly different. The presence of a large volume fraction of conductive cores (R_1) easily led to electrical breakdown at lower electrical field. In contrast, only one single electrical component with $C \sim 1.87 \times 10^{-9}$ F cm^{-1} and resistivity of ∼2.3 MΩ cm was observed for 8% Nd(Zr$_{0.5}$Zn$_{0.5}$)O$_3$ (NZZ)-doped BF−BT ceramics (Figures 17c,d). The conductive electrical component was effectively eliminated by forming a solid solution with NZZ, inhibiting the formation of conductive pathways at higher electric field (>500

Table 8. Energy Storage Properties of NBT-Based Materials[a]

compounds	E (kV cm^{-1})	ΔP (μC cm^{-2})	W_{rec} (J cm^{-3})	η (%)	ref
0.95(0.76NBT−0.24ST)-0.05AN	120	43.5	2.03	61.8	324
$Bi_{0.41}Na_{0.35}Sr_{0.21}TiO_3$	135	~35.8	2.04	82.4	290
$0.75Na_{0.25}Sr_{0.5}Bi_{0.25}TiO_3-0.25MgO$	200	~35	2.06	84	317
$0.8(0.775NBT-0.225BaSnO_3)-0.2BaZrO_3$	245	20	2.08	88.8	315
$0.85NBT-0.15BaHfO_3$	175	29	2.1	66.1	310
$0.775NBT-0.225BaSnO_3-5$ wt %MgO	215	~28	2.13	67.8	326
Sn−0.45ST−0.2NBT−0.35BT	240	~21	2.25	79.51	328
$0.9NBT-0.1Li_2TiO_3$	200	~25	2.3	74.2	291
$(0.5NBT-0.5ST)-1\%SnO_2$	180	37.37	2.35	~80	238
$(Na_{0.5}Bi_{0.5})_{0.8}Ba_{0.2}Ti_{0.8}Sn_{0.8}O_3$	195	~34	2.35	71.04	338
$\{Bi_{0.5}[(Na_{0.8}K_{0.2})_{0.9}Li_{0.1}]_{0.5}\}_{0.96}Sr_{0.04}(Ti_{0.975}Ta_{0.025})O_3$	143	~43	2.42	~64	339
$0.55NBT-0.45(Bi_{0.2}Sr_{0.7}TiO_3)$	200	25	2.5	95	222
$0.94(BNT-Bi_{0.2}Sr_{0.7}TiO_3)-0.06KNN$	180	37	2.65	84.6	298
0.95(0.6ST−0.4NBT)−0.05Zr	285	~25	2.84	71.54	74
$0.85(0.95NBT-0.05SrZrO_3)-0.15NN$	210	~30	2.93	72	325
$0.96(0.65NBT-0.35Sr_{0.85}Bi_{0.1}TiO_3)-0.04NN$	220	50.46	3.08	81.4	323
$0.6(Bi_{0.51}Na_{0.47})TiO_3-0.4Ba(Zr_{0.3}Ti_{0.7})O_3$	280	~25	3.1	91	299
0.9(0.76NBT−0.24NN)−0.1SBT	200	43	3.12	75	340
$0.93NBT-0.07LaAlO_3$	210	43	3.18	60	320
$(Na_{0.25}Bi_{0.25}Sr_{0.5})(Ti_{0.8}Sn_{0.2})O_3$	310	26.5	3.4	90	321
$0.85(Na_{0.5}Bi_{0.5})_{0.7}Sr_{0.3}TiO_3-0.15BMN$	250	38	3.45	88.01	316
$0.95(0.6\ Bi_{0.5}Na_{0.5}TiO_3-0.4Sr_{0.7}Bi_{0.2}TiO_3)-0.05AN$	246	41	3.62	89	322
$0.65(0.84NBT-0.16K_{0.5}Bi_{0.5}TiO_3)-0.35(Bi_{0.2}Sr_{0.7}TiO_3)$	350	~33.99	4.06	87.3	288
0.55NBT−0.45SBT	315	19.1	4.14	92.2	295
$0.90(Na_{0.5}Bi_{0.5})_{0.7}Sr_{0.3}TiO_3-0.10\ Bi(Ni_{0.5}Sn_{0.5})O_3$	270	47	4.18	83.64	341
$0.75Bi_{0.58}Na_{0.42}TiO_3-0.25ST$	535	41	5.63	94	342
0.78NBT−0.22NN	390	45	7.02	85	297
0.62NBT−0.30SBT−0.08BMN	470	48	7.5	92	337

[a] t of the bulk ceramics is commonly >0.1 mm.

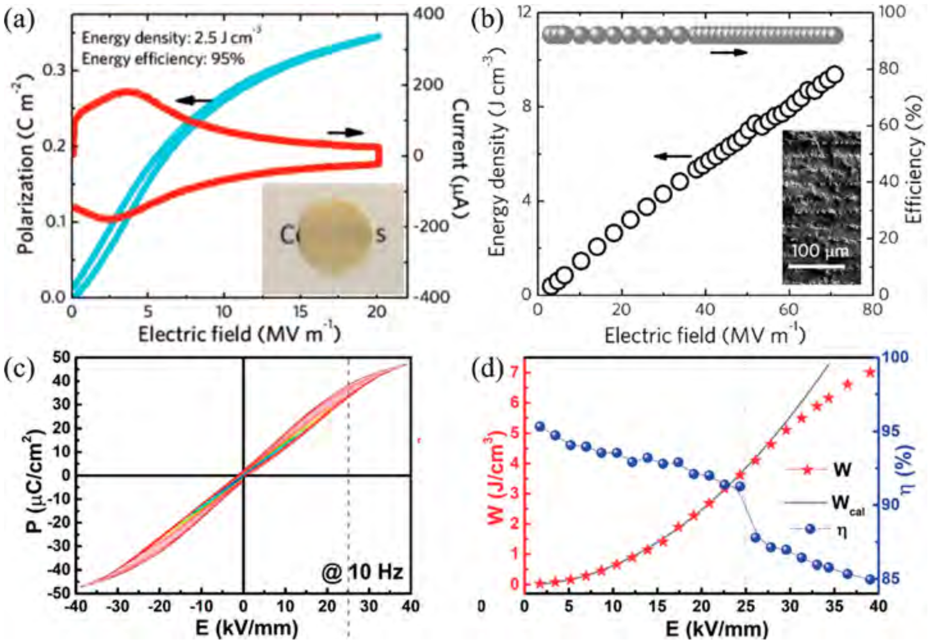

Figure 19. (a) Unipolar $P-E$ loop and the current−E curve for NBT−0.45SBT bulk ceramics. (b) W_{rec} and η for NBT−0.45SBT ceramic MLs; inset SEM image of the ceramic MLs (c) Bipolar $P-E$ loops and (c) calculated W_{rec} and η of 0.78NBT−0.22NN ceramic.[222,297] (a, b) Reproduced with permission from ref 222. Copyright 2018 John Wiley and Sons; (c, d) Reproduced with permission from ref 297. Copyright 2019 Royal Society of Chemistry.

kV cm^{-1}). As a result, optimized W_{rec} ~ 2.45 and 10.5 J cm^{-3} were realized at E_{max} ~ 240 and 700 kV cm^{-1} for 0.08NZZ-BF−BT bulk ceramics and MLs, respectively.

Recently, superior energy density through tailored dopant strategies was achieved in BF−ST−xNb−yBMN ceramics, by promoting electrical homogeneity, enhancing E_a and suppress-

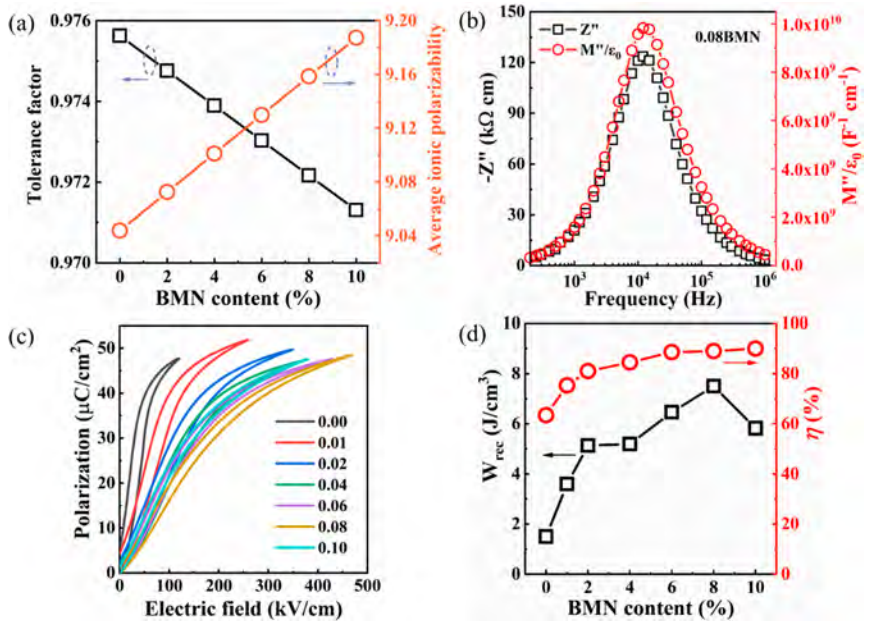

Figure 20. (a) Tolerance factor and average ionic polarizability per unit cell of NBT−SBT−xBMN as a function of BMN concentration. (b) Combined Z'' and M'' spectroscopic plots for NBT−SBT−0.08BMN ceramics at 660 °C. (c) P−E loops at the E_{max}, and (d) W_{rec} and η for NBT−SBT−xBMN ceramics. Reproduced with permission from ref 337. Copyright 2021 Elsevier.

ing the p-type conduction, all of which resulted in significantly enhanced BDS. The ceramic without Nb (BF−ST−0.06BMN, x = 0) exhibits a broadened arc in Z^* at room temperature (Figure 18a) with at least two electrical components observed in combined Z'' and M'' spectroscopic plots (Figure 18b). By donor doping Nb on the B-site, only one ideal semicircle in the Z^* plots with a single Debye peak at the same frequency in both Z'' and M'' spectroscopic plots was observed for all doped samples (Figures 18c,d), suggesting electrical homogeneity. Nb doping suppresses the formation of Fe^{4+} associated with the loss of Bi_2O_3 or/and $V_O^{\cdot\cdot}$ during ceramic processing, thus reducing electrical conductivity with respect to x = 0 by several orders of magnitude, coupled with enhanced E_a (Figure 18e). A reduction in Seebeck coefficient from ∼ 600 μV K^{-1} to zero indicates a commensurate decrease in charge carrier concentration as Nb concentration increases. At x = 0.03, the BDS increases to 360 kV cm^{-1} (Figures 18g) which is insufficient on its own to optimize W_{rec} but when combined with an increase in BMN (y) concentration to reduce polar coupling, results in W_{rec} ∼ 8.2 J cm^{-3} at E_{max} ∼ 460 kV cm^{-1} for BF−ST−0.03Nb−0.1BMN ceramics, Figure 18h.[45]

3.1.2.5. $Na_{0.5}Bi_{0.5}TiO_3$−Based Ceramics.

NBT-based ceramics are promising candidates of lead-free dielectrics due to their high P_{max} and T_c. However, their large hysteresis and low BDS are not ideal for high energy density capacitor applications.[277−284] Attempts to improve their properties generally fall into the following approaches: (i) doping on the A-site (Ba, Sr, K, Li, La, Dy, Nd)[222,239,243,285−296] and B-site (commonly Nb)[297] and codoping (K,Sr/Nb; K,La/Zr; Li,K,Sr/Ta,Nb; K,Mg/Nb; Ba/Nb; Ba/Sn; Ba/Sn,Zr; Ba/Ta; Ba/Zr; Ba,Ca/Zr; Ba,K,Ca/Nb,Zr; Ba/Mg,Nb; Ba/Mg; Ba,La/Al,Nb; Ba,Sr/Yb,Nb; Ba/Hf; La/Al; La,Ba/Nb; Sr/Sn; Sr/Zr; Sr/Mg; Sr/Mg,Nb);[194,298−321] (ii) forming solid solution with other end-members, such as AN, NN, and SBT;[297,322−325] (iii) using additives such as MnO, Fe_2O_3, MgO, SnO_2, ZnO, CaO, and ZrO_2[62,74,238,326−334] and (iv) employing different processing methods such as hot-pressing[59] and synthesis using sol−gel derived powders.[69,71,74,335,336] The energy storage properties of NBT-based materials are summarized in Table 8.

Notably, Li and co-workers reported that 0.55NBT−0.45-$(Sr_{0.7}Bi_{0.2})TiO_3$(SBT) achieved W_{rec} of 2.5 and 9.5 J cm^{-3} with η > 90% for bulk ceramic and MLs at 200 and 720 kV cm^{-1} (Figure 19a,b), respectively.[222] Superior W_{rec} ∼ 7.02 J cm^{-3} and η ∼ 85%, were also reported for 0.78NBT−0.22NN ceramics at E_{max} ∼ 360 kV cm^{-1}, Figures 19c,d, with <10% variation from 25−250 °C and from 0.1 to 100 Hz.[297]

Recently, Ji and co-workers[337] proposed that the key factors for designing an ideal RFE with high energy density were as follows: (i) utilization of a highly polar base system (e.g., NBT); (ii) disruption of long-range polar coupling through forming solid solutions with, e.g., SBT and BMN without sacrificing average ionic polarizability, Figure 20a, and (iii) simultaneously inducing or retaining electrical homogeneity with a highly resistive single component in IS (∼250 kΩ cm at 660 °C), Figure 20b. These factors combined to give E_{max} ∼ 470 kV cm^{-1}, W_{rec} ∼ 7.5 J cm^{-3}, and η ∼ 92% for 0.62NBT−0.30SBT−0.08BMN, Figure 20c,d.

3.1.2.6. $AgNbO_3$−Based Ceramics.

AFEs have long been considered as the prime candidate for energy storage capacitors due to their large P_{max} and small P_r. There are only a handful of lead-free AFE systems, with AN showing particular promise because it possesses a large saturation polarization of 52 μC cm^{-2} under an E_{max} ∼ 220 kV cm^{-1}.[343] Recent research on AN ceramics has focused on stabilizing the AFE phase so that switching field is moved to higher fields while simultaneously optimizing P_{max}.[344,345]

There have been a number of recent studies on AN focusing on (i) substitution of aliovalent B-site oxides such as MnO_2 and WO_3;[346,347] (ii) doping Ba, Sr, Ca, Bi, La, Sm, and Gd on the A-site[348−356] often with isovalent Ta doping on the B-site;[357−359] and (iii) forming solid solutions with end-members, such as $BiMnO_3$ and $Bi(Zn_{2/3}Nb_{1/3})O_3$.[360,361] Most dopants reduce the G of AN which maximizes BDS but delay the onset of the AFE-FE transition to higher field while simultaneously narrowing

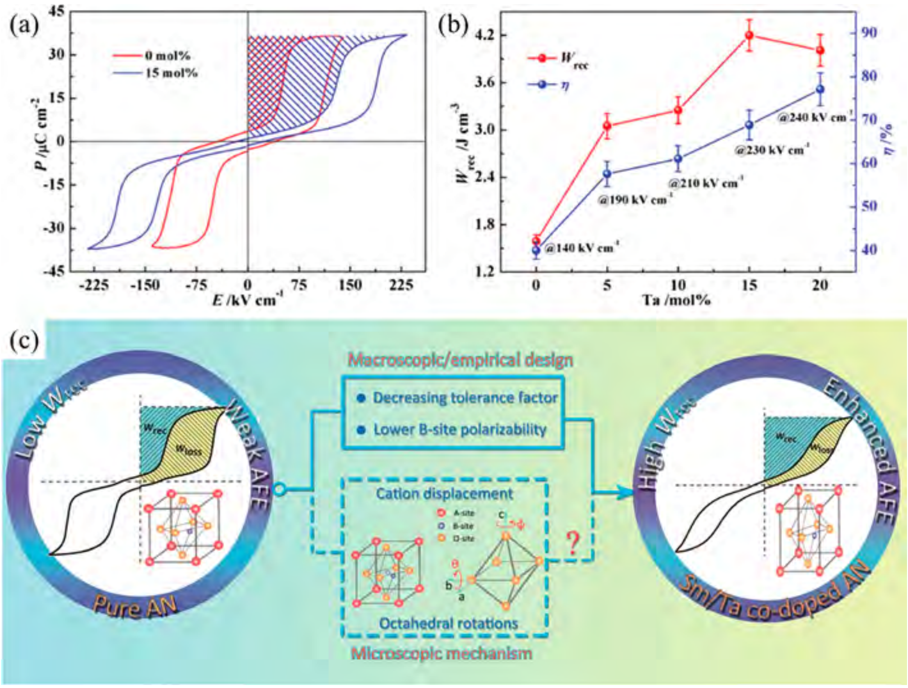

Figure 21. (a) Bipolar *P*−*E* loops of AN and $Ag(Nb_{0.85}Ta_{0.15})O_3$ ceramics. (b) Energy storage performance of $Ag(Nb_{1-x}Ta_x)O_3$ ceramics prior to their breakdown. (c) Schematic of the underlying principles for enhancing energy storage property in AN-based materials. (a, b) Reproduced with permission from ref 357. Copyright 2017 John Wiley and Sons; (c) Reproduced with permission from ref 359. Copyright 2019 Royal Society of Chemistry.

Table 9. Energy Storage Properties of AN-Based Materials[a]

compounds	*E* (kV cm^{-1})	Δ*P* (μC cm^{-2})	W_{rec} (J cm^{-3})	η (%)	ref
AN	150	∼34	2.0	46	345
AN	175	∼33	2.1	40−50	343
$Ag_{0.96}Ba_{0.02}NbO_3$	∼180	∼34	2.3	46	356
0.6 mol % $BiMnO_3$−AN	175	∼36	2.4	54	360
0.1 wt % Mn−AN	150	∼37.2	2.5	57	346
$Ag_{0.91}Bi_{0.03}NbO_3$	200	∼30	2.6	86	353
$Ag_{0.90}Sr_{0.05}NbO_3$	190	∼38	2.9	56	354
$Ag_{0.94}La_{0.02}NbO_3$	230	∼28	3.12	63	352
0.3 wt % Mn-doped $Ag_{0.97}La_{0.01}NbO_3$	142	37.8	3.2	62	351
0.1 wt % W-AN	200	∼42.5	3.3	50	347
AN−0.03NBT	220	33	3.4	62	364
$Ag_{0.90}Ca_{0.05}Nb_{0.95}Ta_{0.05}O_3$	210	37	3.36	58	363
$Ag_{0.92}Ca_{0.04}NbO_3$	220	∼37.6	3.55	63	349
$Ag(Nb_{0.8}Ta_{0.2})O_3$	270	∼30	3.7	∼65	358
$AgNb_{0.85}Ta_{0.15}O_3$	233	∼35.1	4.2	69	357
2 mol % La-doped AN	273	∼30	4.4	70	350
$Ag_{0.88}Gd_{0.04}NbO_3$	290	∼32.5	4.5	∼63	355
$Ag_{0.94}Sm_{0.02}NbO_3$	310	31	4.5	63	362
0.99AN−0.01 $Bi(Zn_{2/3}Nb_{1/3})O_3$	220	46.8	4.6	57.5	115
$(Sm_{0.02}Ag_{0.94})(Nb_{0.9}Ta_{0.1})O_3$	280	∼36	4.87	63.5	359
$Sm_{0.03}Ag_{0.91}NbO_3$	290	∼36	5.2	69.2	348
$AgNb_{0.45}Ta_{0.55}O_3$	460	∼29	6.3	90	365
$Ag_{0.97}Nd_{0.01}Nb_{0.80}Ta_{0.20}O_3$	370	38	6.5	71	366
$Ag_{0.76}La_{0.08}NbO_3$	476	33	7.01	77	367

[a] *t* of the bulk ceramics is typically >0.1 mm.

hysteresis in the induced FE phase. W_{rec} of 4.4, 4.5, and 5.2 J cm^{-3} with η of 70, 63, and 69.2% has been obtained for La, Gd, and Sm A-site doped AN ceramics,[348,351,355,359,362] respectively, and B-site Ta-doped AN was reported to exhibit W_{rec} of 4.2 J cm^{-3} with η of 69% (Figure 21a,b).[357] A-site doping with ions smaller in radius than Ag is suggested to decrease tolerance factor and enhance AFE stability, while donor doping is compensated by A-site vacancies which reduce antipolar and polar coupling of the AFE and field induced FE phases, respectively. Some authors postulate that substituting B-site ions

Table 10. Energy Storage Properties of NN-Based Materials[a]

compounds	E (kV cm^{-1})	ΔP (μC cm^{-2})	W_{rec} (J cm^{-3})	η (%)	ref
NN−0.09Bi($Zn_{0.5}Ti_{0.5}$)O_3	200	29	2.1	76	375
0.9NN−0.10BMN	300	~23	2.8	82	371
0.8NN−0.2ST	323	34.5	3.02	80.7	372
0.78NN−0.22Ba($Mg_{2/3}Nb_{1/3}$)O_3	540	18.7	3.51	87	376
$Na_{0.7}Bi_{0.1}NbO_3$	250	~30	4.03	85.4	377
NN−MnO_2	360	33	4.3	90	378
$Na_{0.84}Bi_{0.08}Nb_{0.92}Zr_{0.08}O_3$	430	30	4.9	88	67
0.9NN−0.1 Bi($Ni_{0.5}Sn_{0.5}$)O_3	550	25	5	68	379
0.78NN−0.22 Bi($Mg_{2/3}Ta_{1/3}$)O_3	620	17	5.01	86.8	373
0.92NN−0.08 Bi($Mg_{0.5}Ti_{0.5}$)O_3	480	38	5.57	71	374
($Na_{0.91}La_{0.09}$)($Nb_{0.82}Ti_{0.18}$)O_3	550	42	6.5	65.9	380
0.75[0.9NN−0.1 Bi($Mg_{0.5}Ta_{0.5}$)O_3]−0.25($Bi_{0.5}Na_{0.5}$)$_{0.7}Sr_{0.3}TiO_3$	800	22	8	90.4	381
0.76NN−0.24NBT	680	~55	12.2	69	42

[a] t of the bulk ceramics is commonly >0.1 mm.

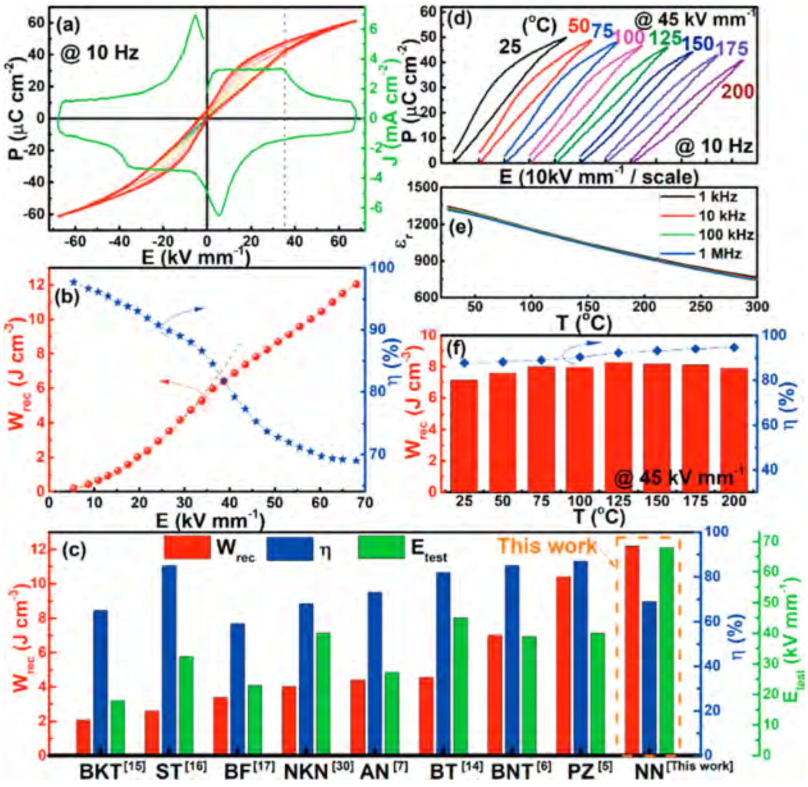

Figure 22. (a) Bipolar P−E loops with corresponding current density-field (J−E) curves and (b) W_{rec} and η values of under different E for the 0.76NN−0.24BNT ceramic at 10 Hz (c) a comparison of W_{rec}, η, and E_{max} among the recently reported bulk ceramics; (d) temperature-dependent P−E hysteresis, (e) temperature- and frequency-dependent ε_r and (f) W_{rec} and η as a function of temperature for the 0.76NN-0.24NBT ceramic at 450 kV cm^{-1}. Reproduced with permission from ref 42. Copyright 2019 John Wiley and Sons.

with a lower polarizability than Nb also stabilizes the AFE phase and moves the switching field higher.[348,350,359,363] The underlying principles are schematically represented in Figure 21c. The energy storage properties of AN-based materials are summarized in Table 9.

3.1.2.7. NaNbO$_3$-Based Ceramics. Recently, AFE NN has received attention as a potential candidate for energy storage applications. An AFE double hysteresis loop is difficult to observe in NN because (i) the energy difference between the AFE phase and field-induced FE phase is very small and (ii) E-induced FE phase is metastable. Thus, AFE behavior in NN based materials is commonly stabilized by chemical substitution with end members such as BS and $CaHfO_3$.[344,368−370]

E_{max} > 250 kV cm^{-1} and W_{rec} > 2.5 J cm^{-3} have been reported for NN in solid solution with BMN, ST, Bi($Mg_{2/3}Ta_{1/3}$)O_3, and Bi($Mg_{0.5}Ti_{0.5}$)O_3 by stabilizing the AFE phase or inducing relaxor behavior,[371−374] as summarized in Table 10. Zuo and coworkers[42] have also proposed the concept of an "AFE relaxor" to explain the energy storage properties of 0.78NN−0.22NBT ceramics. They argue that the local AFE phase transforms reversibly into an FE monoclinic phase at~ 400 kV cm^{-1}, giving a large ΔP (P_{max} > 50 μC cm^{-2} and P_{rem} < 5 μC cm^{-2}). W_{rec} of ~12.2 J cm^{-3} was reported with η ~ 69%, at 680 kV cm^{-1}, Figure 22.[42] However, the term "AFE relaxor" has little physical significance since an antipolar phase cannot form short-range polar features characteristic of a relaxor. 0.78NN−0.22NBT

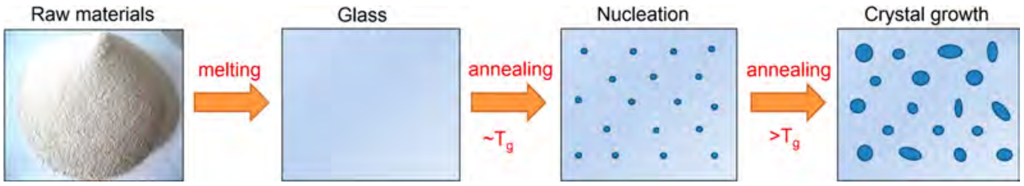

Figure 23. Schematic of the processing step of glass-ceramics.

Table 11. Energy Storage Properties of Glass Ceramics[a]

compounds	ε_r (1 kHz, 300 K)	E (kV cm^{-1})	W_{rec} (J cm^{-3})	ref
$14.4SrO-17.6BaO-32Nb_2O_5-36B_2O_3$	117	1050	5.71	386
$25.6BaO-6.4Na_2O-32Nb_2O_5-36SiO_2$	~90	1248	~6.2	409
$14.3SrO-17.5BaO-31.9Nb_2O_5-35.8B_2O_3-0.5ZnO + 0.5La_2O_3$	131	1127	7.1	400
$20BaO-20SrO-20Nb_2O_5$-$5Al_2O_3-1.5B_2O_3-33.5SiO_2 + 0.2La_2O_3$	92.4	1326	7.2	406
$20SrO-20BaO-10Nb_2O_5-10TiO_2-32SiO_2-8Al_2O_3$	52.9	1817	7.73	410
$14.3SrO-17.5BaO-$ $31.9\%Nb_2O_5-35.8\%B_2O_3-0.5ZnO + 0.5Sm_2O_3$	143.8	1132	8.15	402
$14.4SrO-17.6BaO-32Nb_2O_5-36B_2O_3 + 1\%Yb_2O_3$	98.3	1398	8.5	403
$15K_2CO3-15SrCO3-30Nb_2O_5-32SiO_2-4Al_2O_3-4B_2O_3$	102 (10 kHz)	1411	8.99	407
$20BaO-20SrO-20Nb_2O_5-5Al_2O_3-1.5B_2O_3-33.5SiO_2 + 0.05MnO_2$	95.8	1471	9.2	411
$42[0.2Na_2O-0.8SrO]-28Nb_2O_5-30SiO_2$	53 (100 kHz)	2074	10.09	412
$9.6K_2O-22.4BaO-32Nb_2O_5-36SiO_2$	75	1937	12.06	393
$25.6BaO-6.4K_2O-32Nb_2O_5-36SiO_2 + 1Gd_2O_3$	83	1818	12.14	405
$20BaO-12K_2O-32Nb_2O_5-36SiO_2$	83	1859	12.7	413
$15.16SrO-6.736BaO-10.104K_2O-32Nb_2O_5-28B_2O_3-8P_2O_5$	85.2	1844	12.83	395
$6.4K_2O-25.6SrO-32Nb_2O_5-36SiO_2 + 3CaF_2$	114	1623	13.5	414
$31.2SrO-7.8Na_2O-26Nb_2O_5-35SiO_2$	91	1941	15.2	390
$15\ Bi_2O_3-15Nb_2O_5-40SiO_2-30Al_2O_3$	100	1861	15.3	391
$65(48SrO-12Na_2O-40Nb_2O_5)-35SiO_2$	124	1669	15.3	392
$24BaO-6Na_2O-30Nb_2O_5-10Al_2O_3-30SiO_2$	~70	2322	16.6	388
$15.4Na_2O-15.4PbO-23.1Nb_2O_5-46.2SiO_2$	175	1486	17	385
$25.6(0.4SrO-0.6BaO)-6.4K_2O-32Nb_2O_5-36SiO_2$	118	1828	17.45	394
$21.25BaO-1PbO-12.75Na_2O-34Nb_2O_5-32SiO_2$	154	1638	18.29	389
$25.6BaO-3.2Na_2O-3.2K_2O-32Nb_2O_5-36SiO_2$	22	4433	19	396
$21.6BaO-2.4PbO-6Na_2O-30Nb_2O_5-10Al_2O_3-30SiO_2$	137	1848	20.7	384
$63SiO_2-12BaO-16B_2O_3-9Al_2O_3$	6	12,000	38.5	397

[a] t of the bulk ceramics is commonly >0.1 mm.

may, therefore, be better described as either a relaxor or a short-range AFE phase that undergoes a field induced transition. This intriguing behavior is interesting, but it is the large E_{max} (680 kVcm^{-1}) that is most likely responsible for the exceptional W_{rec} rather than the intrinsic crystal chemistry. The underpinning reasons for the large E_{max} most likely relate to the defect chemistry, band gap and electrical homogeneity, consistent with the key factors proposed by Ji and co-workers.[337]

3.1.3. Glass Ceramics. Glass-ceramics are composed of one or more crystallized phases (ceramics) dispersed uniformly in amorphous phase (glass). They often exhibit the combined properties of ceramics and glass depending on the induced crystalline phases and their microstructures. Glass-ceramics are prepared by melting the requisite raw materials, cooling to room temperature to form a glass, followed by two step annealing to induce crystal nucleation (approximately at the glass transition temperature, T_g) and growth > T_g Figure 23.[179,382] The microstructure of a glass ceramic is typically dominated by a largely 2D and 3D defect-free (e.g., no grain boundaries) glass phase and a uniformly distributed (provided the system undergoes homogeneous rather than heterogeneous nucleation) ceramic phase. W_{rec} and η are both large due to the high BDS associated with the absence of 2D and 3D defects accompanied by a near zero value of P_r. The energy storage properties of glass-based glass ceramics are summarized in Table 11.

As discussed above, the crystallization of glass ceramics is controlled by the annealing procedure, where the annealing temperature and time are critical for nucleation and growth of the ceramic phase, the microstructure and the properties. Generally, the volume fraction of crystalline phase increases with increasing annealing temperature and time, accompanied by an increase of ε_r and decrease of BDS. The optimized W_{rec} is a balance between ε_r and BDS. Chen and co-workers[383] reported that tungsten bronze structured, $Ba_{0.27}Sr_{0.75}Nb_2O_{5.78}$ phase formed from the $Na_2O-BaO-SrO-Nb_2O_5-SiO_2-B_2O_3$ glass matrix at 800 °C and a secondary phase $NaSr_{1.2}Ba_{0.8}Nb_5O_{15}$ emerged when crystallization temperature exceeded 850 °C. Remarkably high BDS ~ 1400 kV cm^{-1} with ε_r of ~50 were obtained, leading to a W_{rec} = 4 J cm^{-3}. Besides, Wang and co-workers reported ultrahigh W_{rec} of 20.7 J cm^{-3} in $BaO-PbO-Na_2O-Nb_2O_5-SiO_2-Al_2O_3$ (BPNN-AS) glass ceramics at the optimized crystallization temperature of 900 °C, as shown in Figure 24.[384] With increasing crystallization temperature from 850 to 1000 °C, the BDS decreased from 1890 to 1440 kV cm^{-1} and the crystallinity increased from 64.5 to 97.3% (Figure 24b). Similar results were also reported in other glass ceramic systems, including $Na_2O-PbO-Nb_2O_5-SiO_2$,[385] $SrO-BaO-Nb_2O_5-$

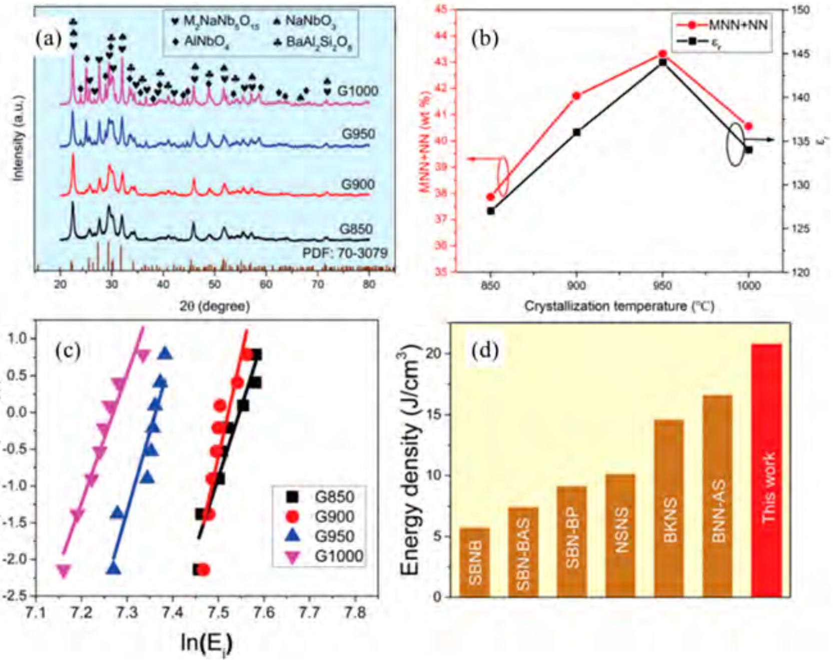

Figure 24. (a) X-ray diffraction (XRD) patterns of BPNN-AS glass ceramics annealed from 850 to 1000 °C; (b) ε_r and $M_2NaNb_5O_{15}$ + NN phase proportion with increasing annealing temperature; (c) BDS Weibull distribution plots; (d) W_{rec} of 900 °C annealed BPNN-AS glass ceramics, compared with other kinds of ferroelectric glass ceramics. Reproduced with permission from ref 384. Copyright 2018 Royal Society of Chemistry.

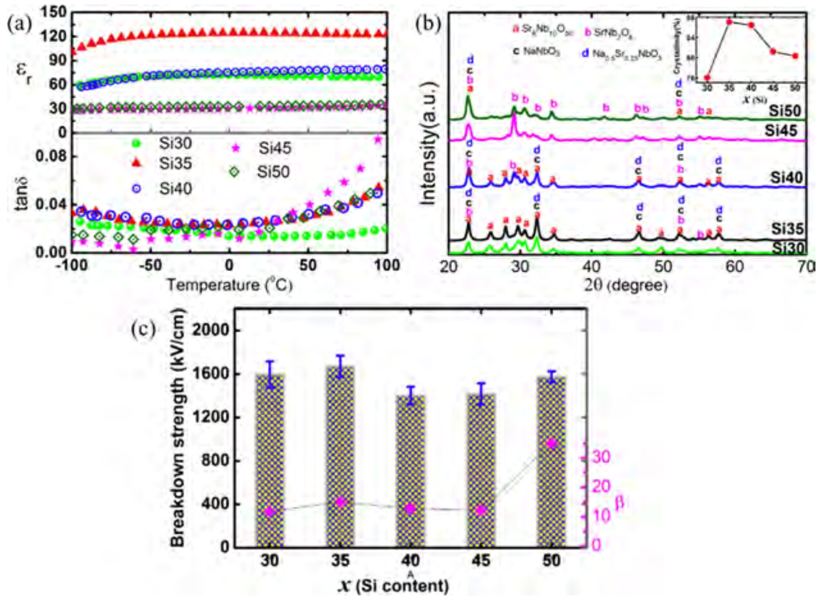

Figure 25. (a) Dielectric properties, (b) XRD patterns, and (c) BDS of SNN-Si glass ceramics as a function of SiO_2 concentration (β). Reproduced with permission from ref 392. Copyright 2017 Elsevier.

B_2O_3,[386] $K_2O{-}SrO{-}Nb_2O_5{-}SiO_2{-}Al_2O_3{-}B_2O_3$,[387] $BaO{-}Na_2O{-}Nb_2O_5{-}SiO_2{-}Al_2O_3$,[388] $BaO{-}PbO{-}Na_2O{-}Nb_2O_5{-}SiO_2$,[389] $SrO{-}Na_2O{-}Nb_2O_5{-}SiO_2$,[390] and $Bi_2O_3{-}Nb_2O_5{-}SiO_2{-}Al_2O_3$.[391]

Each constituent oxide in the glass matrix has an important effect on the crystal phase, microstructure, BDS, and energy storage properties. For example, SiO_2 is an important and active studied constituent oxide in glass matrix. With increasing SiO_2 content, ε_r of $SrO{-}Na_2O{-}Nb_2O_5{-}SiO_2$ (SNN-Si) glass ceramics first increased and then decreased as shown in Figure 25a, which was attributed to the change of volume fraction $Sr_6Nb_{10}O_{30}$ (Figure 25b). The optimal ε_r of 120 and BDS ~ 1700 kV cm^{-1} were obtained with 35 mol % SiO_2 (Figures 25a,c), resulting in the highest theoretical W_{rec} of 15.2 J cm^{-3}.[392] Wang and co-workers reported that, as K_2O concentration increased in $K_2O{-}BaO{-}Nb_2O_5{-}SiO_2$ glass ceramics, grain boundary R and activation energy decreased, indicating the decrease of interfacial polarization, leading to the enhancement of BDS to ~1900 kV cm^{-1} and W_{rec} ~ 12 J cm^{-3}.[393] They also reported that substitution of Sr for Ba in $SrO{-}BaO{-}K_2O{-}Nb_2O_5{-}SiO_2$ led to the formation of solid phase $Sr_{0.5}Ba_{0.5}Nb_2O_6$ and improvement of dielectric properties.[394] The highest BDS of ~1800 kV cm^{-1} and W_{rec} of 17.5 J cm^{-3} were achieved with Sr = 0.4 due to a uniform and dense microstructure and lower interfacial polarization. Li and co-workers reported substitution of K with Ba in $SrO-BaO-K_2O-Nb_2O_5-B_2O_3-P_2O_5$ glass ceramics transformed $Ba_{0.5}Sr_{0.5}Nb_2O_6$ to a solid solution of $K_{2xy}Ba_{(1-x)y}Sr_{5-y}Nb_{10}O_{30}$ and then $KSr_2Nb_5O_{15}$ phase, leading to a decrease in ε_r.[395] A maximum theoretical W_{rec} of 12.8 J cm^{-3} was obtained under BDS ~ 1800 kV cm^{-1}, along with dielectric loss <0.3%. Liu and co-workers studied the effect of R_2O (R = Li, Na, K) on the phase structure, dielectric properties and BDS in $BaO-R_2O-Nb_2O_5-SiO_2$ glass ceramics, where the highest W_{rec} ~ 19 J cm^{-3} was achieved with ε_r ~ 22 and superior BDS of ~4400 kV cm^{-1} in composition of $BaO-Na_2O-K_2O-Nb_2O_5-SiO_2$.[396]

Compared with alkali based compositions, alkali-free glass compositions were found to deliver lower dielectric loss and fewer defect microstructure. For example, Smith and co-workers reported both ultrahigh E_{max} ~ 12000 kV cm^{-1} and W_{rec} ~ 35 J cm^{-3} in $BaO-B_2O_3-Al_2O_3-SiO_2$ glass.[397] The effect of Al/Si ratio on the modification of the microstructure and properties of $SrO-BaO-Nb_2O_5-SiO_2-Al_2O_3$ glass ceramics was also studied by Xiu and co-workers.[398]

Additionally, rare-earth oxides, such as La_2O_3,[399−401] Sm_2O_3,[402] Yb_2O_3,[403,404] and Gd_2O_3,[405] are also commonly substituted into glass formulations for energy storage applications. Rare-earth oxides are mainly reported to act as nucleating agents[399,402] or crystal growth inhibitors.[400,406] Zhang and co-workers revealed that La_2O_3 leads to a homogeneous microstructure in the $BaO-SrO-TiO_2-Al_2O_3-SiO_2$ glass-ceramics which improved BDS ~ 1600 kV cm^{-1} and W_{rec} ~ 3.2 J cm^{-3} (2.5 times of the glass-ceramics without La_2O_3).[399] Zheng and co-workers reported that 0.5 mol % La_2O_3 in $SrO-BaO-Nb_2O_5-B_2O_3-ZnO$ glass-ceramics also optimized ε_r (~130) and W_{rec} ~ 7.1 J cm^{-3} through achieving a BDS ~ 1100 kV cm^{-1} due to a reduction in crystallite size and precipitation of high ε_r phase, $Sr_{0.5}Ba_{0.5}Nb_2O_6$.[400] A similar effect was reported for Sm_2O_3 by Chen and co-workers in the $SrO-BaO-Nb_2O_5-B_2O_3-ZnO$ glass ceramics with W_{rec} of 8.2 J cm^{-3} at 1100 kV cm^{-1}.[402] Moreover, Yb_2O_3 is reported to eliminate the impurity phases and form a uniform microstructure in $BaO-SrO-TiO_2-Al_2O_3-B_2O_3-SiO_2$ glass-ceramics, leading to W_{rec} of 3.5 J cm^{-3}, ~ 1.8 times higher than undoped compositions.[404]

Apart from the conventional annealing, novel methods such as microwave treatment have been reported to improve the energy storage properties of glass ceramics. Zhang and co-workers found that microwave treatment restrained the formation of the dendritic microstructure in $Ba_xSr_{1-x}TiO_3-(Ba-B-Al-Si-O)$ (BST−BBAS) glass-ceramics (Figure 26), leading to the improvement of BDS from 1200 kV cm^{-1} to 1500 kV cm^{-1}, corresponding to W_{rec} of 2.8 J cm^{-3} (950 °C anneal).[408] Xiao and co-workers further reported that the precipitation of impurity phases in the $K_2O-SrO-Nb_2O_5-SiO_2-Al_2O_3-B_2O_3$ glass-ceramics was limited by controlling the crystallization time using microwave sintering, with optimum ε_r, BDS of 1400 kV cm^{-1} and maximum theoretical W_{rec} (~9 J cm^{-3}) obtained after 10 min.[407]

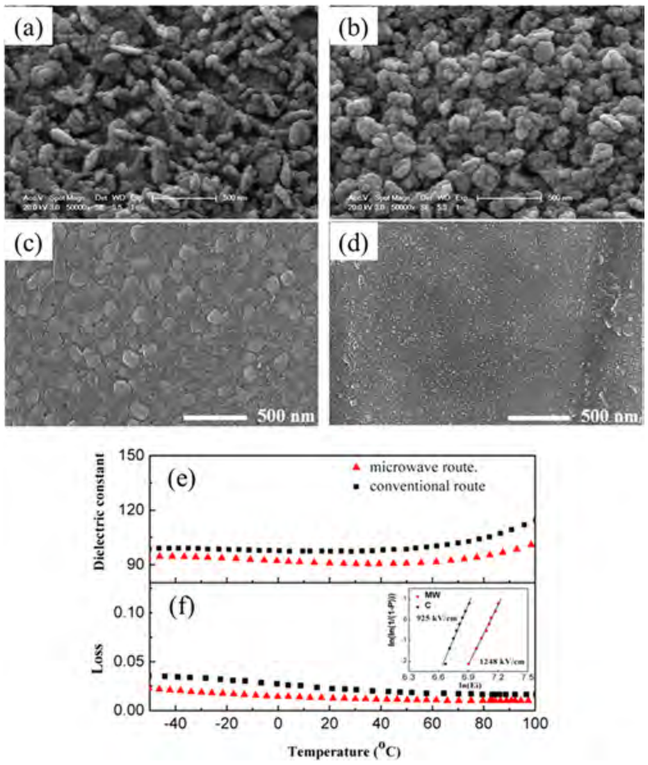

Figure 26. SEM images of BST-BBAS samples annealed at 950 °C by (a) conventional method and (b) microwave treatment.[408] SEM images of BNNS samples annealed at 1000 °C by (c) conventional method and (d) microwave treatment. (e, f) Temperature dependence of dielectric properties of BNNS samples. The BDS plot is inset in (f).[409] (a, b) Reproduced with permission from ref 408. Copyright 2014 Elsevier; (c−f) Reproduced with permission from ref 409. Copyright 2017 Elsevier.

3.1.4. Summary of State-of-the-Art in Ceramics.

The debate over whether lead-free electroceramics can replace their lead-based counterparts has been ongoing for over two decades. Lead based compositions generally outperform their lead-free counterparts on most metrics. Moreover, lead-free compositions are disparate with a large number of different formulations potentially required to cover the properties achieved with essentially doped PZT. Provided, however, that the performance, reliability and cost of lead-free are competitive with PZT, it is highly likely that lead-free electroceramics will begin to replace their lead-based equivalents and attain large scale production in the coming years as a consequence of environmental legislation.[31,103,415]

Of all the applications, lead-free high energy density capacitors are the most likely to see large-scale production since (i) the performance of lead-free compositions is approaching that of lead-based; (ii) reduction in intrinsic electrical properties may be compensated by increasing the BDS often through decreasing layer thickness (see section 3.1.2); and (iii) the capacitor industry is dominated by lead-free BT-based MLCCs, and thus, there is an expectation that the related products will not contain lead.[34,45,90,209,276,416] This latter statement does not hold for piezoelectric ceramics market which is dominated by PZT and its derivatives.[174,417−419]

The energy storage performances, E_{max}, ΔP, W_{rec}, and η, for lead-based and lead-free ceramics are summarized and plotted in Figure 27 (note: glass ceramics are not included). A comparison of W_{rec} vs E_{max} for different lead-based/lead-free bulk ceramics is displayed in Figure 27a. Lead-based bulk ceramics have the advantage of both high E_{max} (up to ~400 kV cm^{-1}) and W_{rec} (up to ~12 J cm^{-3}) with respect to lead-free candidates. NN-based ceramics currently offer the highest W_{rec} under high E (>350 kV cm^{-1}) for lead-free compositions, followed by AN-, NBT-, BF-, and KNN-based materials. BT and ST-based ceramics display the lowest W_{rec} in spite of their high E_{max} of ~450 kV cm^{-1}, but

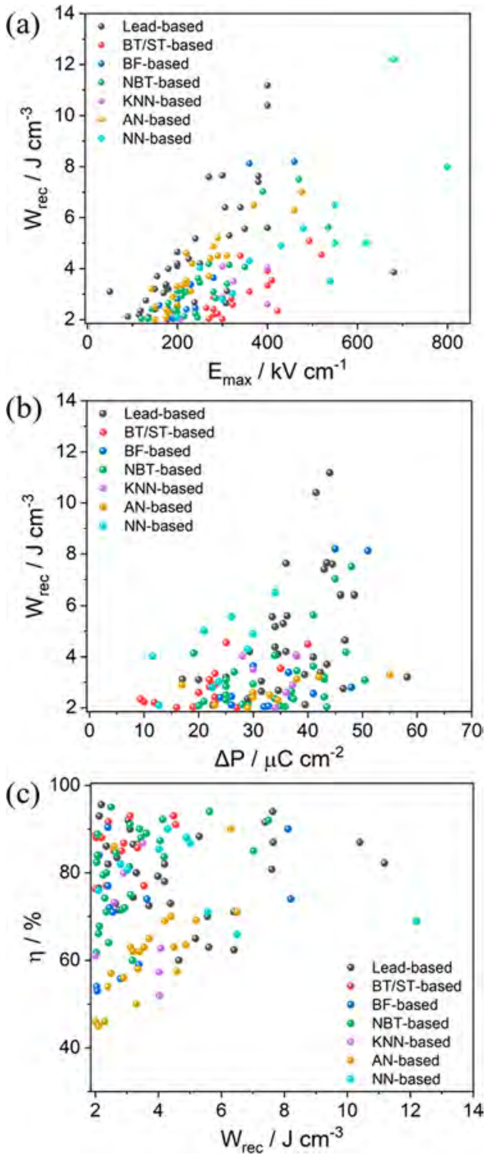

Figure 27. Comparison of (a) E_{max} vs W_{rec}; (b) ΔP vs W_{rec}; and (c) W_{rec} vs η for lead-based/lead-free bulk ceramics. **t* of the bulk ceramics is commonly >0.1 mm.

they are perhaps the most appealing dielectrics commercially since they are the current basis of MLCC production.

ΔP vs W_{rec} is compared in Figure 27b. Lead-, NBT-, and BF-based materials exhibit extraordinarily high ΔP (up to ∼60 μC cm^{-2}), followed by AFE NN- and AN-based (up to ∼40 μC cm^{-2}) and KNN-based materials (up to ∼35 μC cm^{-2}) with the lowest (up to ∼25 μC cm^{-2}) for BT- and ST-based materials. Bicontaining electroceramics such as NBT and BF, have been heavily studied recently as potential lead-free electroceramic materials due to their large polarization.[260,266,281,282,284,420−423] A high ΔP (60 μC cm^{-1}) is obtained in NBT and BF based by reducing the P_r through chemical substitution with other perovskite end members to form a relaxor with an ultraslim P−E loop. To some extent therefore, the advantage of a high intrinsic polarization end member such as BF is weakened. Intermediate $\Delta P \sim 40\ \mu$C cm^{-2} values are observed for AFEs such as AN- and NN-based materials but P_{max} is often limited as compositions exhibit polarization saturation as a function of applied field.

Figure 27c compares W_{rec} vs η for a wide range of compositions. ST-based materials display the best η (∼90%) due to their linear-like dielectric behavior. For BT-, NBT-, and lead-based materials, η varies with the material composition since it is a function of many factors. Dielectric loss associated with defects such as $V_O^{\cdot\cdot}$ play a role but primarily at high field and high frequency, energy is dissipated during the transition to a field induced long-range ordered state which is manifested by the opening of the P−E loop. If the transition is smeared over for the operational range through alloying or doping to create a so-called "weakly coupled relaxor state", η > 90% can be achieved.[43,209,337]

High leakage current and electrical conductivity are considered as major challenges in BF and KNN-based materials but are addressed by appropriate doping, e.g. donor doping to mitigate *p*-type conductivity in BF-based ceramics.[45] In addition, AFE based materials generally suffer from opening of the polarization loop above switching field to form a field induced FE phase which is detrimental to η. Compositional modifications to AN and NN ceramics aim not only to push the AFE-FE transition to higher field and stabilize the AFE phase but also to disrupt the long-range ordering in the field induced FE phase, thereby creating a slimmer portion of the P−E loop (higher η) than that being observed in unmodified materials.[366]

Apart from the parameters discussed above (E_{max}, ΔP, W_{rec}, and η), temperature and frequency stability are also important for practical applications. In the future, high energy density ceramic capacitors will be placed closer to the core engine electronics to optimize the equivalent circuit resistance. Therefore, the temperature requirement for energy storage ceramics is anticipated to increase. According to the white paper "Multilayer Ceramic Capacitors for Electric Vehicles" published by Knowles capacitors in 2017,[424] the explosive development of EVs has prompted the appearance of new 200 °C-stable C0G type I dielectric ceramic capacitor on the market. However, these materials still do not fulfill the required high power/voltage, energy density, and temperature requirements (∼250 °C) to facilitate use near-engine. Better frequency stability from 100 Hz to 100 kHz is required to reduce power fluctuations when capacitors are used for DC/DC conversion for battery charging and DC/AC conversion for propulsion.[425−429] Enhanced frequency stability also enables the capacitor to be compatible with diodes and thyristors for power switching and control.[430]

The temperature and frequency stabilities of many high energy density ceramics are evaluated, as shown in Figure 28. Only two compositions to date deliver W_{rec} > 3.5 J cm^{-3} up to 250 °C, 0.57BF−0.33BT−0.1NN[43] and 0.78NBT−0.22NN.[297] Most other compositions either do not sustain or do not have properties reported >200 °C. Typical issues associated with operating at higher temperature include, widening of the P−E loop or early breakdown due to high leakage current and electric field and/or temperature-induced phase transitions. High leakage currents above 200 °C typically arise from oxygen vacancy diffusion.[45]

Most compositions have been shown to deliver W_{rec} at a few hundred Hz but higher frequencies (>kHz) are rarely reported. Wang and co-workers, for example, discussed frequency stability from 10^{-2} to 10^{2} Hz for 0.57BF-0.3BT−0.13BLN with $W_{rec} \sim 8$ J cm^{-3} and $\eta \sim 81\%$ at 400 kV cm^{-1}. All electroceramics for capacitors appear to deliver a charging−discharging speed at or faster than 1 μs. Short times of $\tau_{0.9} \sim 0.15\ \mu$s (90% of energy discharge in 0.15 μs) were reported by Li and co-workers in BT

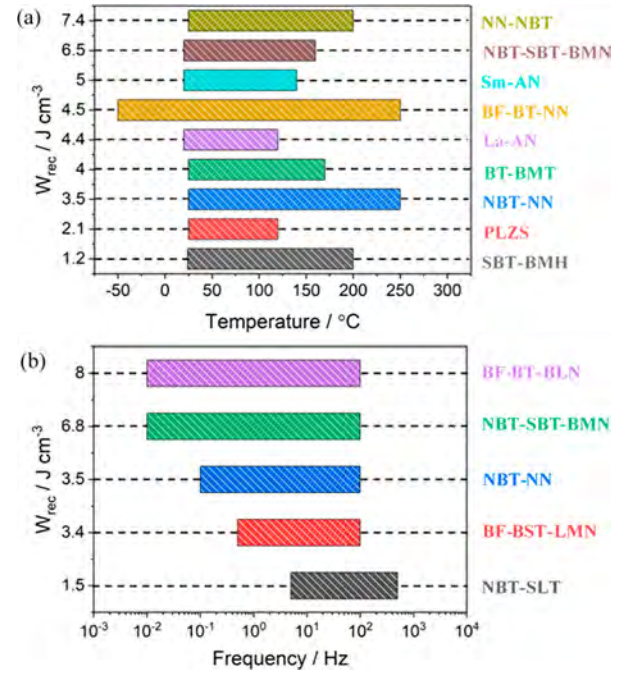

Figure 28. (a) Temperature-[42,43,130,131,208,242,297,337,348,352,357,359] and (b) frequency-dependent W_{rec} for some reported electroceramic materials for high energy density capacitors.[276,295,297,337,416]

based ceramics at 150 kV cm^{-1}[197] while Qi et al. described even faster charging−discharging speeds ($\tau_{0.9}$ ∼ 97 ns) in BF-based ceramics at 200 kV cm^{-1}.[42] Increasing attention has also been focused on fatigue-resistant behavior as a performance metric in practical applications with 10^4 cycles (W_{rec} variation <10%) reported in BF-based ceramic multilayers from 20 to 100 °C, coupled with a low value of electrostrain (<0.03%).[276]

3.2. Ceramic Multilayers and Films

3.2.1. Ceramic Multilayers. Ceramic MLs are fabricated by a series of processing steps which include slurry preparation, tape-casting, screen printing, lamination, cosintering, and termination, as shown in Figure 29.[18,176,422,431,432] This fabrication technology is a powder-based approach that accommodates scale-up from laboratory research to commercial manufacturing. The market of ceramic MLs ∼ \$5.3 billion in 2017 but will reach ∼ \$7.8 billion by 2024 for electronic applications, including but not limited to mobile phones, laptops and motor vehicles.[433] Advanced high energy density ceramic MLs, based on AFEs and RFEs materials, are being developed to facilitate power electronics within hybrid electric vehicles which require higher W_{rec} and operating temperature. Simultaneously, research into low cost internal electrodes is required so that the highest performant ceramics can be developed. The energy storage properties for different ceramic MLs are summarized in Table 12.

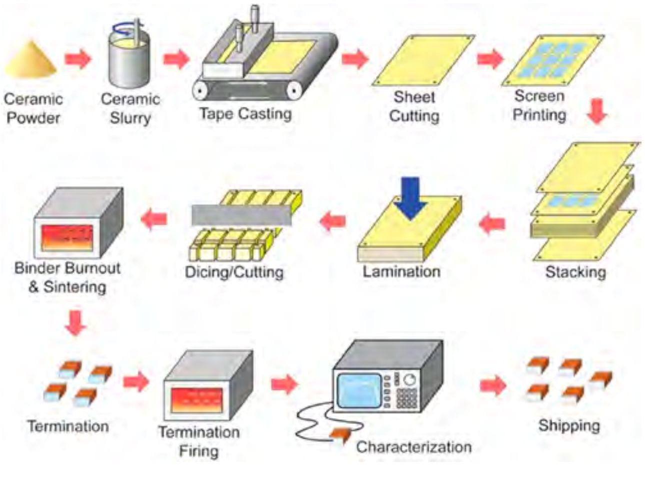

Figure 29. Ceramic MLs fabrication process (MLs cofire technology). Reproduced with permission from ref 18. Copyright 2010 IEEE.

Several lead-based AFE ceramic MLs have been reported using different internal electrodes. A giant power density ∼2000 kW cm^{-3} and W_{rec}∼ 3 J cm^{-3} was obtained in $Pb(Zr_{0.95}Ti_{0.05})_{0.98}Nb_{0.02}O_3$ MLs using Pt as internal conductive electrode.[434] Optimized performance of W_{rec} ∼ 3.8 J cm^{-3} was also reported by Hao and co-workers for $(Pb_{0.88}Ba_{0.05}La_{0.02}Dy_{0.04)}(Zr_{0.68}Sn_{0.27}Ti_{0.05})O_3$ MLs using 5% Ag/95%Pd internal electrode. However, this was accompanied by a large electric field-induced strain ∼0.71% at 300 kV cm^{-1},[435] a major drawback for practical applications due to inferior mechanical stability in operation. To date, Hao and co-workers have reported the record-high W_{rec} ∼ 12.6 J cm^{-3} and η ∼ 80% under E_{max} ∼ 560 kV cm^{-1} for $Pb_{0.98}La_{0.02}(Zr_{0.7}Sn_{0.3})_{0.995}O_3$ ceramic ML, as shown in Figure 30.[436]

Although lead-free AFE ceramics show great promise, there are no reports of ceramic MLs in the literature. Instead, lead-free RFEs have dominated recent ceramic ML research due to their excellent W_{rec} and fatigue-resistant behavior accompanied by negligible electric field induced strain. 0.87BT−0.13 $Bi(Zn_{2/3}(Nb_{0.85}Ta_{0.15})_{1/3})O_3$ ceramic MLs have been fabricated with a dielectric layer t of 11 μm using 60Ag/40Pd internal electrodes that exhibit excellent W_{rec} ∼ 8.13 J cm^{-3} and η ∼ 95% at 750 kV cm^{-1}.[437] The energy storage properties of 0.87BT−0.13 $Bi(Zn_{2/3}(Nb_{0.85}Ta_{0.15})_{1/3})O_3$ were further enhanced by Zhao and co-authors by decreasing the dielectric layer to ∼5 μm, achieving W_{rec} ∼ 10.12 J cm^{-3} at 1012 kV cm^{-1}, Figure 31a,b, as well as demonstrating good temperature stability from 75 to 175 °C.[438] NBT−0.45SBT ceramic MLs have also been reported to exhibit W_{rec} ∼ 9.5 J cm^{-3} with η ∼ 95% at 720 kV cm^{-1},[222] which were further improved by forming a solid solution with a third perovskite end-member, 10%BMN to give W_{rec} ∼ 18 J cm^{-3} with η > 90% at 1000 kV cm^{-1}, by Ji and co-workers, Figures 31c,d.[337] The highest among all lead/lead-free ceramic MLs, W_{rec} ∼ 21.5 J cm^{-3} at ∼1030 kV cm^{-1}, however, was achieved for textured NBT−0.3SBT ceramic MLs.[439] Texturing was achieved through the use of <111>-oriented ST platelets which reduced field-induced strain at high field thus enhancing the BDS greatly. Combination of texturing with alloying with a third end member (BMN) in NBT−SBT may well represent an exciting path to achieve yet higher energy densities.

Wang, Reaney, and co-workers have employed a range of different chemical dopants and alloying additions to investigate BF-(B,S)T-based ceramic multilayers.[34,45,90,276,416] In 2018, Nd-doped BF-0.3BT was reported to exhibit W_{rec} ∼ 6.74 J cm^{-3} (more than 3 times higher than the bulk value) and η ∼ 77% at 540 kV cm^{-1} with a layer t of 33 μm.[90] On the other hand, alloying BF−0.3BT with 8 mol % $Nd(Zr_{0.5}Zn_{0.5})O_3$ resulted in W_{rec} ∼ 10.5 J cm^{-3} with η of 87% at 700 kV cm^{-1} with a dielectric layer t of ∼17 μm, Figure 17.[34] Further studies focused on promoting electrical homogeneity, which was considered to prevent conductive pathways developing in these composition, thereby avoiding the breakdown at high field and facilitating the

Table 12. Summary of the Energy Storage Performance of Ceramic MLs

materials	t (μm)	electrode	E (kV cm^{-1})	ΔP (μC cm^{-2})	W_{rec} J cm^{-3}	η (%)	ref
[0.94(0.75NBT−0.25NN)−0.06BT]−0.1$CaZrO_3$	30	70Ag/30Pd	120		0.35	77	440
BT + BT@SiO_2 *layer structure	10/20		301.4	18	1.8	71.5	441
ST + Li_2CO_3)/(0.94NBT−0.06BT) *layer structure	50/12		237	30	2.41	68	442
$(Pb_{0.88}Ba_{0.05}La_{0.02}Dy_{0.04})$ $(Zr_{0.68}Sn_{0.27}Ti_{0.05})O_3$	11	95Pd/5Ag	300	28	2.7	67.4	435
0.6NBT−0.4ST	27	75Ag/25Pd	270		2.83	85	443
$Pb(Zr_{0.95}Ti_{0.05})_{0.98}Nb_{0.02}O_3$	32				3		434
Nb and Mn co-doped 0.9BT−0.1NBT	30	60Ag/40Pd	480	18	3.33	80	444
$Ca(Zr_{0.80}Ti_{0.20})O_3$	10	Pt	1500	6	4		445
BT−0.12 $Bi(Li_{0.5}Ta_{0.5})O_3$	30	Pt	466	25	4.05	95.5	203
BT−0.12 $Bi(Li_{0.5}Nb_{0.5})O_3$	29	Pt	450	25	4.5	91.5	198
0.7BT−0.3$BiScO_3$	25	Pt	730	24	6.1		33
15% Nd doped BF−BT	33	Pt	540	39	6.74	77	90
BT−0.13$Bi[Zn_{2/3}(Nb_{0.85}Ta_{0.15})_{1/3}]O_3$	11	60Ag/40Pd	790	27	7.8	88	446
BT−0.13$Bi[Zn_{2/3}(Nb_{0.85}Ta_{0.15})_{1/3}]O_3$	11	60Ag/40Pd	750	27	8.13	95	437
NBT−0.45$(Sr_{0.7}Bi_{0.2})TiO_3$	30	Pt	720	30	9.5	92	222
BF−0.3$Ba_{0.8}Sr_{0.2}TiO_3$−0.06$La(Mg_{2/3}Nb_{1/3})O_3$	8	Pt	720	43	10	77	416
BT−0.13$Bi[Zn_{2/3}(Nb_{0.85}Ta_{0.15})_{1/3}]O_3$	5	60Ag/40Pd	1047	30	10.12	89.4	438
BT−0.13$Bi[Zn_{2/3}(Nb_{0.85}Ta_{0.15})_{1/3}]O_3$	9	60Ag/40Pd	1000	30	10.5	93.7	447
BF−0.3BT−0.08$Nd(Zr_{0.5}Zn_{0.5})O_3$	17	Pt	700	34	10.5	87	34
$Pb_{0.98}La_{0.02}(Zr_{0.7}Sn_{0.3})_{0.995}O_3$	20	Pt	560	50	12.6	80	436
BF−0.3BT−0.13 $Bi(Li_{0.5}Nb_{0.5})O_3$	8	Pt	953	45	13.8	81	276
BT−0.13$Bi[Zn_{2/3}(Nb_{0.85}Ta_{0.15})_{1/3}]O_3$	4.8	Pt	1500	36	14.1	69.7	448
0.50BF−0.40ST−0.10BMN	8	Pt	1000	50	15.8	80	45
NBT−0.30$(Sr_{0.7}Bi_{0.2})TiO_3$−0.08BMN	8	Pt	1000	50	18	93	337
BT−0.13$Bi[Zn_{2/3}(Nb_{0.85}Ta_{0.15})_{1/3}]O_3$@$SiO_2$	4.7	60Ag/40Pd	1755	35	18.24	94.5	89
⟨111⟩-textured NBT−0.30SBT	20	Pt	1030	>65	21.5	80	439

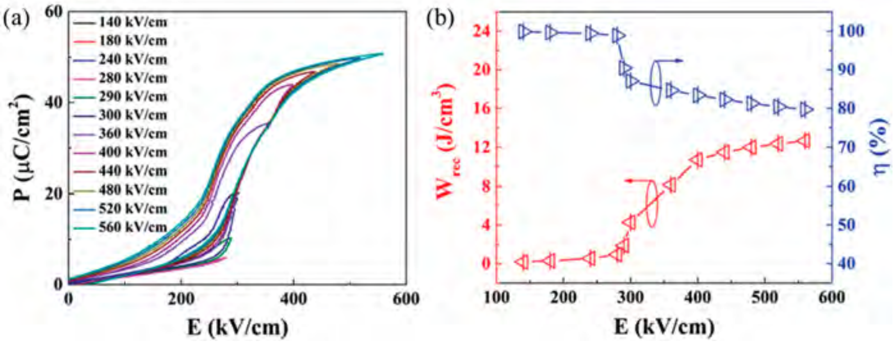

Figure 30. (a) P−E loops under electric field up to E_{max} (b) calculated W_{rec} and η values for $Pb_{0.98}La_{0.02}(Zr_{0.7}Sn_{0.3})_{0.995}O_3$ ceramic ML. Reproduced with permission from ref 436. Copyright 2020 Royal Society of Chemistry.

improvement of W_{rec} by reducing the dielectric layer thickness. Finally, W_{rec} ~ 13.8 J cm^{-1} at 953 kV cm^{-1} was achieved for BF−0.3BT−0.13 $Bi(Li_{0.5}Nb_{0.5})O_3$ (BF−BT−0.13BLN) ceramic MLs at a dielectric layer t of 8 μm, as shown in Figure 32.[276]

3.2.2. Ceramic Films.

Higher BDS and W_{rec} compared to MLs fabricated through powder-based technology have been reported for ceramic films deposited on $LaNiO_3/Si_{(100)}$ or $Pt/Ti/SiO_2/Si$ substrates by physical vapor or chemical deposition techniques, such as radio frequency magnetron sputtering,[449] spin coating,[101,450,451] pulsed laser deposition,[452] and chemical solution deposition.[453] The BDS of ceramic films is significantly improved due to the reduction of t (<1 μm) often attributed to fewer defects (grain boundaries) and/or pore/void concentration. Not only have higher figures of merit been reported for ceramic films, but several researchers have proposed novel underlying mechanisms (beyond reduction in defect density) behind the enhancement, such as the formation of polymorphic nanodomains.[452] However, nonpowder based techniques are difficult to scale up into MLCCs, which may constrain these extraordinary results to lab-based fundamental research rather than promising practical output for commercial exploitation. The energy storage properties for ceramic films are summarized in Table 13.

Lead-based ceramic films have been studied heavily in the past decade using different preparation methods, particular for PLZT. $(Pb_{0.94}La_{0.04})(Zr_{0.98}Ti_{0.02})O_3$ ceramic film with t of 2 μm was reported to exhibit 47.4 J cm^{-3} under electric field of 3700 kV cm^{-1} on a $Pt_{(111)}/TiO_2/SiO_3/Si_{(100)}$ substrate.[454] Further increasing La concentration resulted in superior W_{rec} ~ 40.2 J cm^{-3} and η ~ 62%, achieved at E_{max}~ 1998 kV cm^{-1} for $Pb_{0.91}La_{0.09}(Zr_{0.65}Ti_{0.35})_{0.9775}O_3$ on a $LaNiO_3$/F-Mica substrates.[449] In addition, for $Pb_{0.97}La_{0.02}Zr_{0.66}Sn_{0.23}Ti_{0.11}O_3$, an improved W_{rec} ~ 46.3 J cm^{-3} was achieved at ~4000 kV cm^{-1}, accompanied by excellent temperature stability (up to 380 K) and cyclic reliability (up to 10^5), Figure 33.[453]

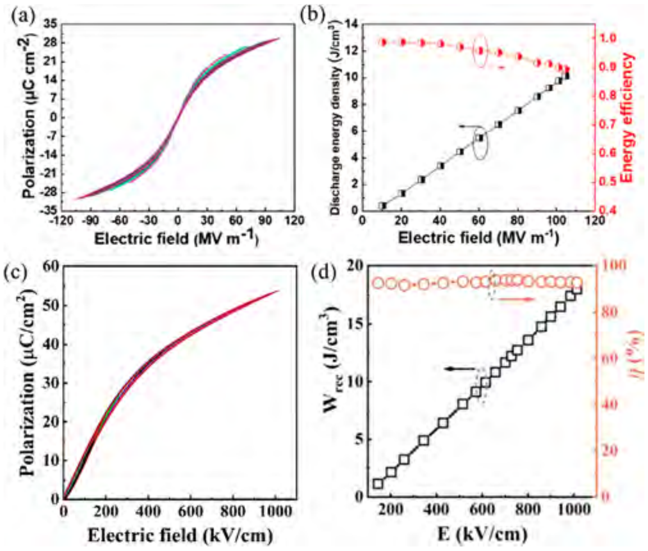

Figure 31. (a) Bipolar $P-E$ loops and (b) calculated W_{rec} and η of $0.87BT-0.13Bi[Zn_{2/3}(Nb_{0.85}Ta_{0.15})_{1/3}]O_3$ MLs under different electric fields.[438] (c) Unipolar $P-E$ loop, with inset SEM micrograph of ceramic MLs, and (d) calculated W_{rec} and η of NBT−0.45SBT−0.08BMN ceramic MLs under different E. (a, b) Reproduced with permission from ref 438. Copyright 2019 John Wiley and Sons; (c, d) Reproduced with permission from ref 337. Copyright 2021 Elsevier.

In the past few years, there has been increased focus on lead-free ceramic films due to concerns over toxicity of PbO. NBT and BF based relaxor compositions have dominated research and have competitive or even superior energy storage performance to lead-based films. Mn doped NBT ceramic films on a $LaNiO_3/Si_{(100)}$ substrates with t = 1.2 μm were reported to exhibit excellent W_{rec} ∼ 30.2 J cm^{-3} under E_{max} ∼ 2310 kV cm^{-1}.[455] Similar properties, W_{rec} ∼ 33.3 J cm^{-3} under E_{max} ∼ 2300 kV cm^{-1}, were also obtained for Fe doped NBT−$K_{0.5}Bi_{0.5}TiO_3$ ceramic film.[456] Recently, even higher W_{rec} ∼ 50.1 J cm^{-3}, η ∼ 63.9% accompanied by fast charge−discharge speed (∼210 ns) were achieved simultaneously at ∼2200 kV cm^{-1} in relaxor 0.6NBT−0.4 $Bi(Ni_{0.5}Zr_{0.5})O_3$ films.[457] In addition, an ultrahigh W_{rec} ∼ 112 J cm^{-3} with η ∼ 80% was reported by Pan and co-workers in BF−BT−ST ceramic films recently (Figure 34). Polymorphic nanodomains with competitive rhombohedral and tetragonal phases with competitive free energy were considered critical for the extraordinary electrical properties. BF was chosen as a main component due to its large spontaneous polarization. BT was introduced to form a solid solution to encourage coexistence of rhombohedral and tetragonal phases and finally ST was incorporated to further disrupt the long-range polar coupling and induce polymorphic nanodomains. By tuning the ratio of BF, BT and ST, a highly disordered composition is produced with rhombohedral and tetragonal nanodomain. The experimental observations were validated by phase-field simulations in the optimized composition, 0.20BF−0.25BT−0.55ST.[452] Apart from these perovskite lead-free relaxor candidates, HfO_2-based ceramic films have also been explored and demonstrate promising energy storage properties, stabilities/reliabilities, scalability, and integration. W_{rec} ∼ 46 J cm^{-3} with excellent temperature stability (up to 175 °C) and cyclic fatigue resistant (up to 10^9 time) was reported by Park in a 9.2 nm thick $Hf_{0.3}Zr_{0.7}O_2$ film[458] and W_{rec} ∼ 63 J cm^{-3} with η ∼ 85% were realized in 50 nm thick Al doped HfO_2 ceramic films with excellent temperature and frequency stability.[459]

3.2.3. Summary of State-of-the-Art in Ceramic MLs and Films.

The energy storage performances, W_{rec}, η, and ΔP, between bulk ceramics, ceramic MLs, and ceramic films are shown in Figure 35. The highest W_{rec} (∼130 J cm^{-3}) and E_{max} (∼5800 kV cm^{-1}) are obtained in ceramic films, followed by ceramic MLs (∼21 J cm^{-3} and E_{max} ∼ 1000 kV cm^{-1}) and bulk

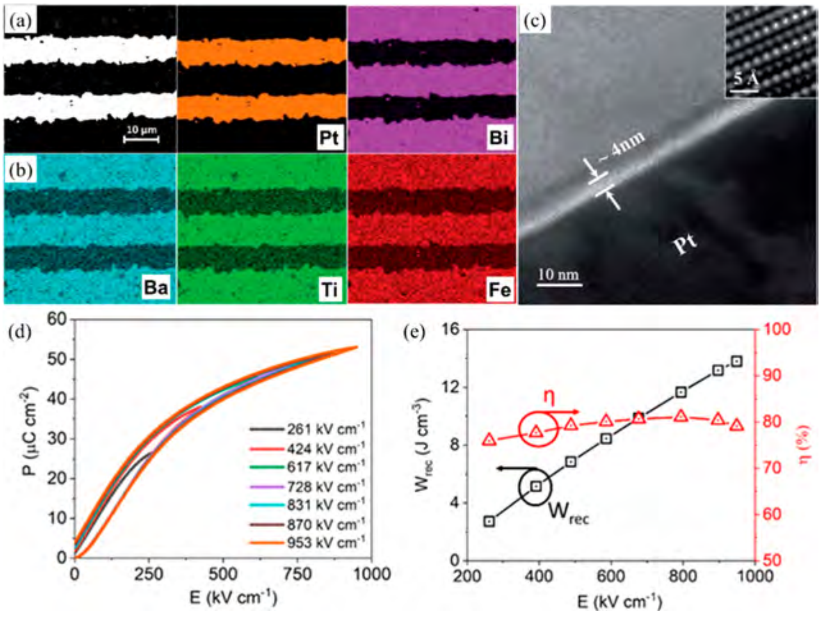

Figure 32. (a) Backscattering electron (BSE) cross section micrographs of BF−BT−0.13BLN ceramic MLs; (b) energy dispersive X-ray (EDX) mapping of all elemental distribution (c) transmission electron microscopy (TEM) micrograph obtained from an interface between a BF−BT−0.13BLN grain and a Pt grain (electrode); inset shows a high resolution TEM (HRTEM) image (filtered) obtained from the grain at a higher magnification. (d) Unipolar $P-E$ loops and (e) calculated energy storage properties for BF−BT−0.13BLN ceramic MLs. Reproduced from ref 276. Copyright 2020 Royal Society of Chemistry.

Table 13. Energy Storage Properties for Different Ceramic Films

materials	t (μm)	E (kV cm^{-1})	ΔP (μC cm^{-2})	W_{rec} (J cm^{-3})	η (%)	ref
$Pb_{0.97}La_{0.02}(Zr_{0.97}Ti_{0.03})O_3$	1.7	1158	~90	20.1	64	460
1 mol %Fe−doped 0.72NBT−0.18KBT−0.10ST	0.9	1200	58	20.34	35.17	461
$Pb_{0.97}Y_{0.02}[(Zr_{0.6}Sn_{0.4})_{0.925}Ti_{0.075}]O_3$	0.5	1300	70	21	91.9	462
$Pb_{0.92}La_{0.08}(Zr_{0.52}Ti_{0.48})O_3$	0.4	1600	35	22	77	463
$Pb_{0.85}La_{0.1}ZrO_3$	0.45	1500	45	23.1	73	464
$0.942(Na_{0.535}K_{0.480}NbO_3)-0.058LiNbO_3$	5	1400	~52	23.4	70	465
$(Sr_{0.85}Bi_{0.1})Ti_{0.99}Mn_{0.01}O_3$	0.25	1982	35	24.4		466
$Pb_{0.97}La_{0.02}(Zr_{0.98}Ti_{0.02})O_3$	2	984	~120	25.2	52	467
$Bi(Mg_{0.5}Ti_{0.5})O_3$	0.11	900	70	26	55	468
$(Pb_{0.98}La_{0.08})(Zr_{0.52}Ti_{0.48})O_3$	0.25	2200	40	27.5	62.2	469
6 mol % BF-doped $(K_{0.5}Na_{0.5})(Mn_{0.005}Nb_{0.995})O_3$	1	2000	~40	28	90	470
$PbZrO_3/PbZr_{0.52}Ti_{0.48}O_3$	0.35	2615	60	28.2	50	471
$(Pb_{0.92}La_{0.08})(Zr_{0.65}Ti_{0.35})O_3$	0.32	3000	40	29.7	50.8	472
1 mol % Mn-doped NBT	1.2	2310	~40	30.2	48	455
$(K_{0.5}, Na_{0.5})(Mn_{0.005}, Nb_{0.995})O_3$-6 mol % BF	1	1900	45	31	90.3	470
$0.9Pb(Mg_{1/3}Nb_{2/3})O_3-0.1PbTiO_3$	0.375	2640	35	31.3	40	473
0.9(0.94NBT−0.06BT)−0.1NN	0.3	3170	20	32	90	474
$0.4\ Bi(Mg_{0.5}Zr_{0.5})O_3-0.6PbTiO_3$	0.5	2000	43	32.3	51.4	475
2 mol % Fe-doped $(Na_{0.85}K_{0.15})_{0.5}Bi_{0.5}TiO_3$	1.15	2300	~35	33.3	51	456
0.95NBT−0.05ST	1.5	1950	~55	36.1	41	476
$Ba_2Bi_4Ti_5O_{18}$	0.41	2150	38	37.1	91.5	477
$Pb_{0.82}La_{0.12}Zr_{0.85}Ti_{0.15}O_3$	1	2100	~52	38	71	478
5.8 mol % SiO_2 doped HfO_2	0.01	~5800		40	72	479
$Pb_{0.91}La_{0.09}\ (Zr_{0.65}Ti_{0.35})_{0.9775}O_3$	1	1998	~65	40.2	62	449
0.89NBT−0.06BT−0.05BF	0.28	1750	150	42.9	65.7	480
$BaBi_4Ti_4O_{15}$	0.45	2000	40	43.3	87.1	481
$Bi_{3.25}La_{0.75}Ti_3O_{12}$	0.5	2040	50	44.7	78.4	482
$Hf_{0.3}Zr_{0.7}O_2$	0.0092	4500	30	46	53	458
$Pb_{0.97}La_{0.02}Zr_{0.66}Sn_{0.23}Ti_{0.11}O_3$	0.65	4000	55	46.3	84	453
$0.5\ Bi(Ni_{1/2}Ti_{1/2})O_3$-0.5PT	0.455	2250	62	46.7		483
$Pb_{0.94}La_{0.04}(Zr_{0.98}Ti_{0.02})O_3$	2	3699	~48	47.4	25	454
0.4ST-0.6 $Bi_{3.25}La_{0.75}Ti_3O_{12}$	0.3	2470	38	47.7	87.4	484
0.9 $Bi_{0.2}Sr_{0.7}TiO_3$-0.1BF	0.46	4800	25	48.5	47.57	485
Si doped $Hf_{0.5}Zr_{0.5}O_2$	0.01	~3500	~30	50	80	486
0.6NBT−0.4 $Bi(Ni_{0.5}Zr_{0.5})O_3$	1	2200	~63	50.1	64	457
$0.5\ Bi(Ni_{1/2}Ti_{1/2})O_3$-0.5PT-excess 20% PbO	0.45	2250	75	50.2		487
$(Pb_{0.97}La_{0.02})(Zr_{0.7}Sn_{0.25}Ti_{0.05})O_3$	1.8	3750	~75	56	45	488
0.6BT−0.4 $Bi_{3.25}La_{0.75}Ti_3O_{12}$	0.3	3200	45	61.1	84.2	489
6 mol % Si-doped HfO_2	0.01	4500		61.2	65	490
8 atom % Al doped HfO_2	0.05	4900	14	63	90	459
$Na_{0.485}Bi_{0.5}(Ti_{0.96}W_{0.01}Ni_{0.03})O_3$	0.6	2500	30	63.1	55	491
$BF/Bi_{3.25}La_{0.75}Ti_3O_{12}$	0.14	2753	50	65.5	74.2	492
$Bi_{0.525}Na_{0.5}(Ti_{.96}W_{0.01}Ni_{0.03})O_3$	0.4	2500	78	65.8	52.9	493
0.25BF−0.75ST	0.5	4460		70	70	494
0.97(0.93NBT−0.07BT)−0.03BF	0.35	2285	~120	81.9	64.4	495
$(Ba_{0.95}Sr_{0.05})(Zr_{0.2}Ti_{0.8})O_3$	0.1	6200		102	87	496
0.25BF−0.3BT−0.45ST	0.45	4900	90	112	80	452
0.68PMN−0.32PT	0.15	5800	~100	130	75	497

ceramics (W_{rec} (~12 J cm^{-3} and E_{max} ~ 650 kV cm^{-1}) and scale primarily with t of the dielectric layer (Figure 35d). W_{rec} in ceramic films is also improved by higher ΔP (up to ~120 μC cm^{-2}) with respect to ceramic MLs (up to ~70 μC cm^{-2}) and bulk ceramics (up to ~60 μC cm^{-2}), as shown in Figure 35b. η for bulk ceramics, ceramic MLs and ceramic films varies significantly with composition and relates to factors such as, energy dissipation through a field induced transition to a long-range polar state, domain switching, polarization rotation, and leakage current relating to the presence of $V_O^{\cdot\cdot}$ and associated defect dipoles.

From a commercial perspective, energy storage performance of lead-free ceramic MLs has improved significantly in the past few years with BF and NBT based ceramic MLs now rivalling lead-based ceramic MLs, delivering W_{rec} > 15 J cm^{-3} at ~1000 kV cm^{-1}. However, the selection of inner electrodes for these materials is limited to Pt, currently too costly for mass production. Commercial focus therefore, currently remains mainly on modified BT compositions which are compatible with Ni, Ag and Ag/Pd electrodes depending on composition and pO_2 during fabrication. A huge stride forward in the industry would be the development of a low cost equivalent to Ag/Pd

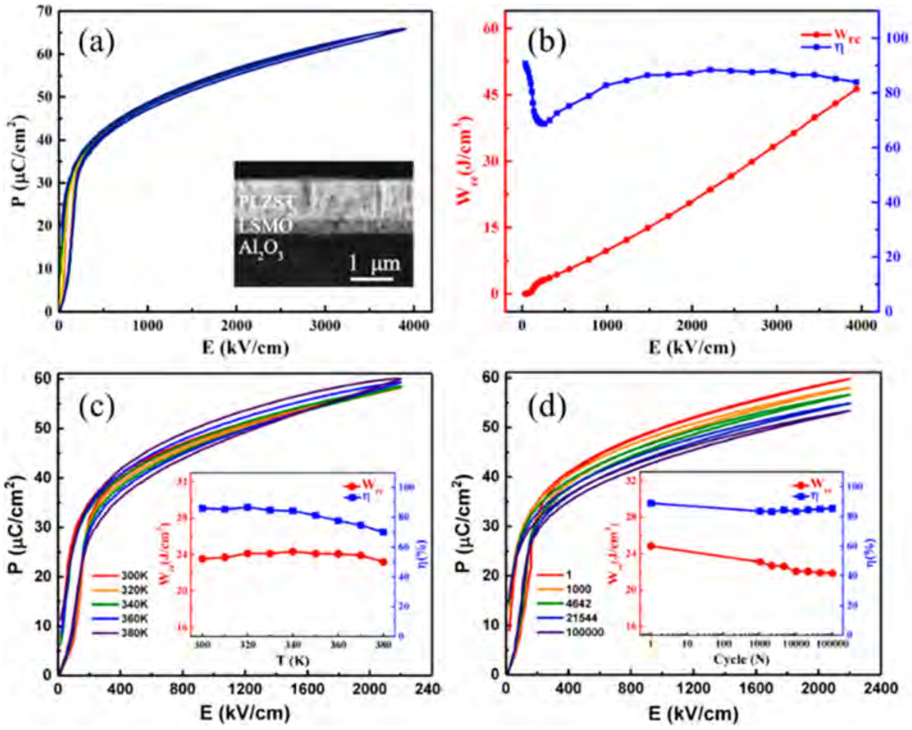

Figure 33. (a) Unipolar *P*−*E* loops, inset image is cross-section SEM image of ceramic film deposited on the substrate, and (b) W_{rec} and η of $Pb_{0.97}La_{0.02}Zr_{0.66}Sn_{0.23}Ti_{0.11}O_3$ ceramic film under various *E*. (c) Temperature and (d) cyclic unipolar *P*−*E* loops, W_{rec}, and η of $Pb_{0.97}La_{0.02}Zr_{0.66}Sn_{0.23}Ti_{0.11}O_3$ ceramic film under E~ 2200 kV cm^{-1}. Reproduced with permission from ref 453. Copyright 2018 Elsevier.

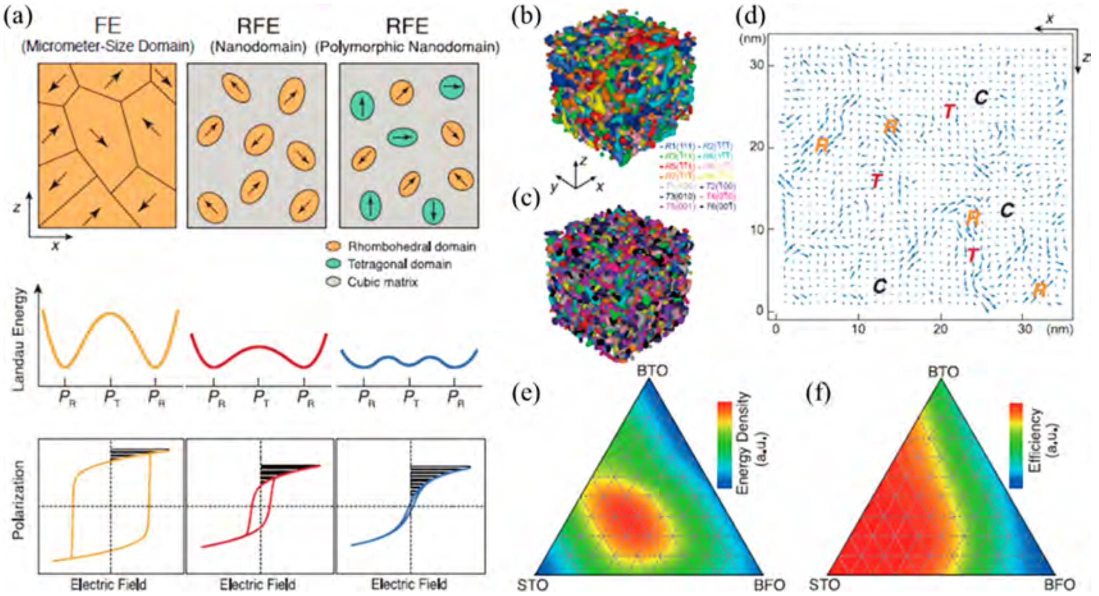

Figure 34. (a) Comparative display of Landau energy profiles and *P*−*E* loops of an FE with micrometer-size domains, an RFE with nanodomains, and an RFE with polymorphic nanodomains. Phase-field-simulated three-dimensional domain structures of (b) 0.45BF-0.55ST with rhombohedral nanodomains and (c) 0.20BF-0.25BT−0.55ST with coexisting rhombohedral and tetragonal nanodomains. (d) Simulation of the two-dimensional multiple nanodomain structure of 0.20BF-0.25BT−0.55ST in the cubic matrix. Contour plots of the simulated (e) W_{rec} and (f) η of BF−BT−ST solid solutions. Reproduced with permission from ref 452. Copyright 2019 The American Association for the Advancement of Science.

electrodes which could permit the fabrication of a wider range of MLs at higher pO_2 which would inhibit the formation of $V_{O}^{\cdot\cdot}$ and maintain high BDS.

4. STRATEGIES FOR IMPROVING ENERGY STORAGE PROPERTIES

The review of the state-of-the-art of ceramics, MLs, and films presented in section 3 clearly points to a set of criteria that are required to optimize energy storage performance. Though some of these have been alluded to in section 3 as part of the review of the state-of-the-art, it is worth collating these principals for RFE

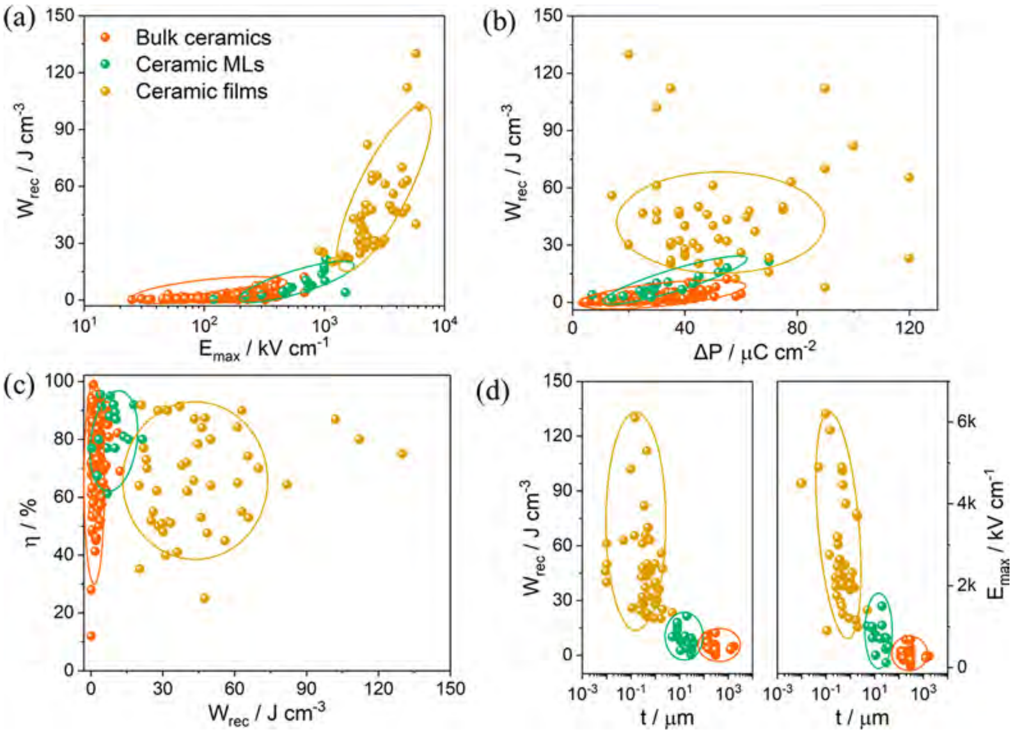

Figure 35. (a) E_{max} vs W_{rec}, (b) ΔP vs W_{rec}, (c) W_{rec} vs η, and (d) t vs W_{rec} and E_{max} between bulk ceramics, ceramic MLs and ceramic films.

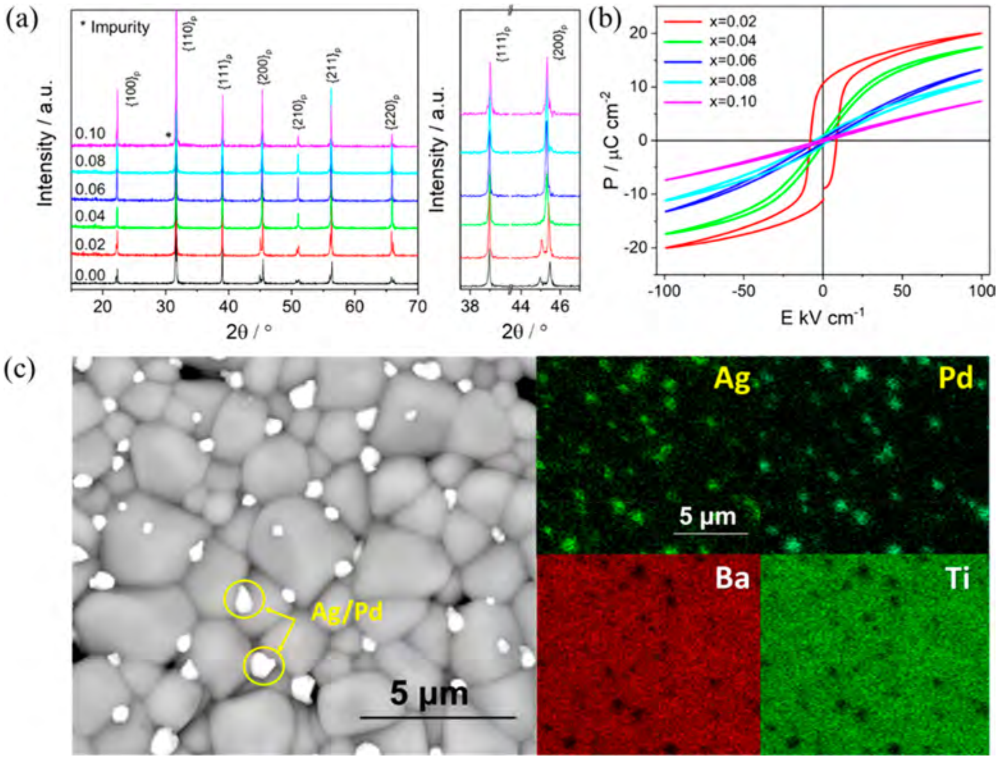

Figure 36. (a) XRD patterns with representative peaks and (b) Bipolar P–E loops for xB$_{2/3}$MN–BT ceramics with x = 0.00–0.10. (c) BSE surface micrographs of Ag–Pd cofired 0.06B$_{2/3}$MN–BT ceramics. (d) EDX mapping distribution of Ag, Pd, Ba, and Ti elements. Reproduced from ref 209. Copyright 2020 American Chemical Society.

and AFE materials to act as guide for future materials development.

4.1. Optimization through an Induced Relaxor State

The most commonly utilized strategy to optimize energy storage properties is through inducing a relaxor state within a system that contains highly polarizable ionic species. It is typically carried out through strategic doping or alloying to form a pseudoternary solid solution. Levin and co-workers proposed that long-range ferroelectric correlations can be effectively “blocked” by using designed dopants with enhanced local

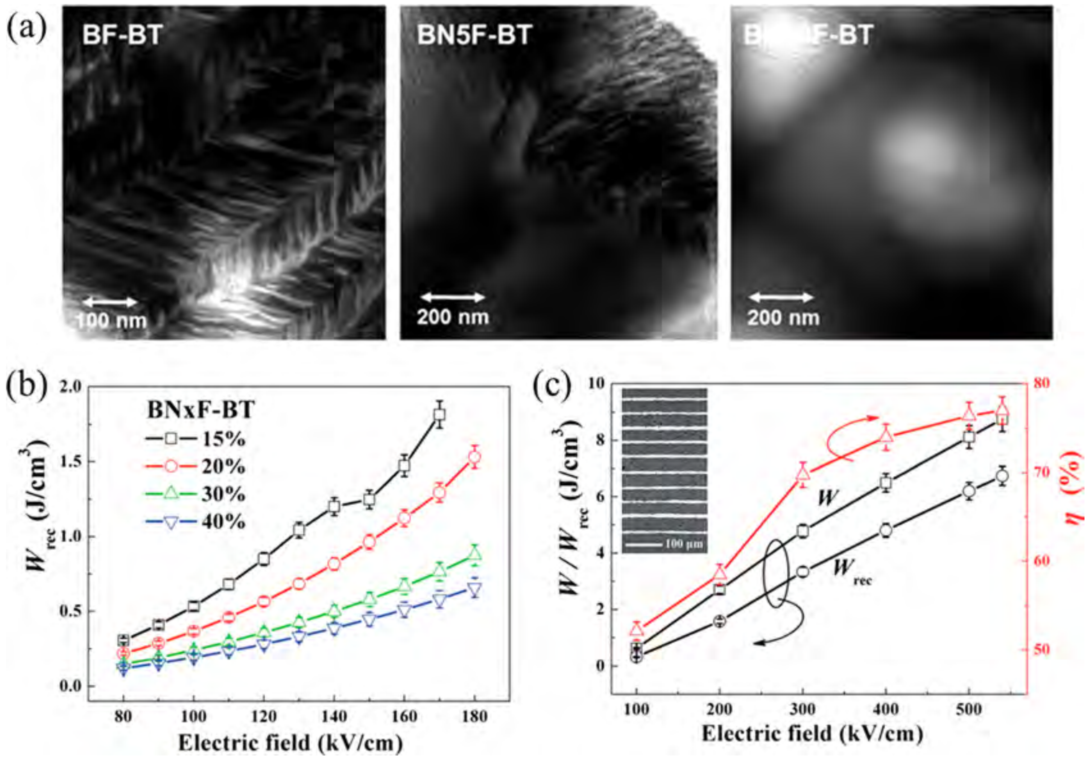

Figure 37. (a) TEM images of the domain structure in BF−BT, 5 mol % Nd−BT−BT and 10 mol % Nd−BF−BT. (b) The changes of W_{rec} as a function of electric field for x mol % Nd−BF−BT ceramics. (d) W, W_{rec}, and η for 15 mol % Nd−BF−BT MLs, with ceramic MLs microstructure as inset figure. Reproduced with permission from ref 90. Copyright 2018 Royal Society of Chemistry.

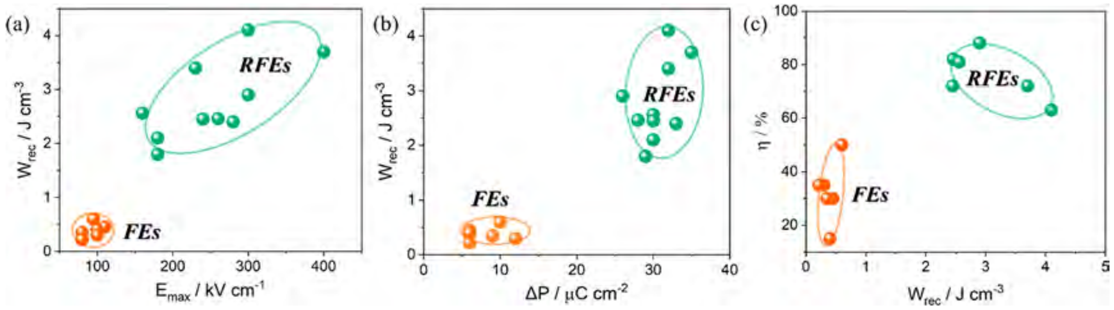

Figure 38. (a) E_{max} vs W_{rec}, (b) ΔP vs W_{rec} and (c) W_{rec} vs η for FEs and RFEs bulk ceramics to demonstrate the relaxor optimization.

polarizability.[498] If this concept is married to dopant strategies to induce or maintain a homogeneous electrical microstructure, ΔP and BDS can be optimized leading to a large W_{rec}.

These two simple precepts can be applied to most systems; e.g., a frequency dispersion of ε_r was observed after doping xBi$_{2/3}$(Mg$_{1/3}$Nb$_{2/3}$)O$_3$ (B$_{2/3}$MN) into BT ceramics, along with reduction on maximum dielectric constant (ε_m) and associated temperature (T_m).[209] After fitting the ε_r and T_m using modified Curie−Weiss law (as follows)

$$\frac{1}{\varepsilon_r} - \frac{1}{\varepsilon_m} = \frac{(T - T_m)^{\gamma}}{C} \tag{17}$$

γ was found to be within the range of 1.61 for BT−0.06B$_{2/3}$MN ceramics with a Burns temperature ∼154 °C. In addition, XRD revealed a transformation from tetragonal to an average pseudocubic structure as increasing x concentration, coupled with a reduction in P_r, confirming a relaxor state at room temperature, Figure 36a,b.

An optimum $W_{rec} \sim 4.55$ J cm^{-3} at 520 kV cm^{-1} was recorded for BT−0.06B$_{2/3}$MN (Figure 36)[209] with similar properties reported for Bi(Mg$_{0.5}$Ti$_{0.5}$)O$_3$,[208] Bi(Li$_{0.5}$Ta$_{0.5}$)O$_3$,[203] Bi(Zn$_{0.5}$Zr$_{0.5}$)O$_3$,[199] and K$_{0.73}$Bi$_{0.09}$NbO$_3$[499] doped BT ceramics. However, the advantage of BT−B$_{2/3}$MN is in the comparatively low concentration of dopant required to induce a relaxor state. The polar coupling is disrupted through a combination of A-site (Bi and $V_O^{\cdot\cdot}$) and B-site (Nband Mg) dopants which provide a range of difference in ionic size, charge and electronegativity. However, only 4 mol % Bi is present on the A-site which minimizes reaction with Ag/Pd (Figure 36c). MLs with Ag−Pd internal electrodes may then be fired in ambient pO$_2$, minimizing $V_O^{\cdot\cdot}$ and reducing leakage current at high fields.

Similar compositional modifications to induce a relaxor state have been adopted in BF-based solid solution. For example, in FE BF−BT compositions, macroscopic herringbone-type domains are observed in (Figure 37a) but doping with 5 mol % Nd, induced a nanodomain state, accompanied by a decrease in P_r and a frequency-dependent permittivity curve, confirming

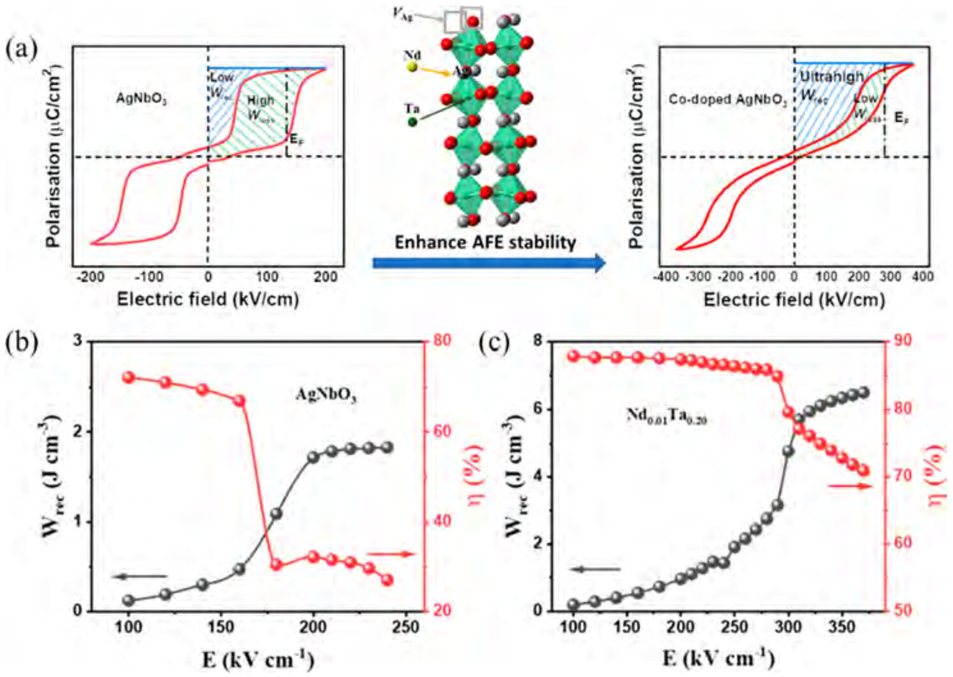

Figure 39. (a) Schematic illustrating how W_{rec} is optimized through doping in AN. Gray, yellow, green, dark green, and red spheres represent Ag, Nd, Nb, Ta, and O atoms, respectively. The W_{rec} and η of (b) AN and (c) $Nd_{0.01}Ta_{0.20}$ codoped AN under the respective electric fields.[366]

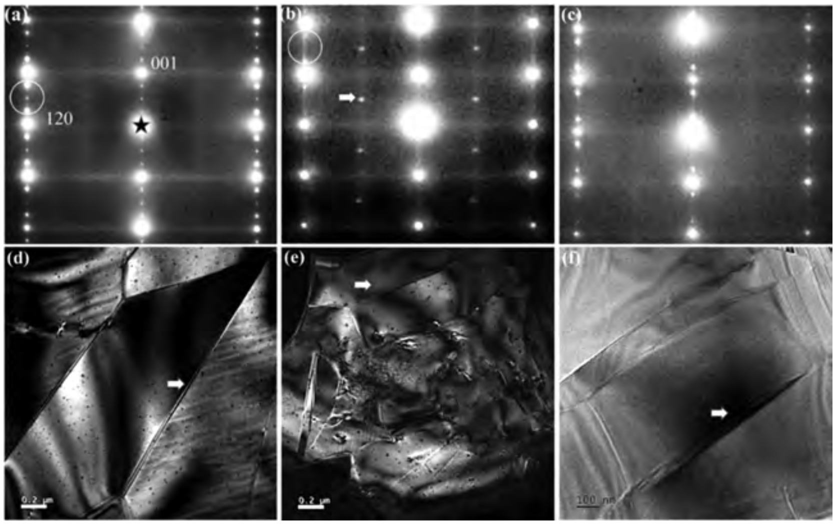

Figure 40. TEM $[210]_c$ (c = cubic) zone axis diffraction patterns and corresponding dark field images obtained using (001) reflections from (a) and (b) AN and (c) and (d) $Ag_{0.91}Nd_{0.03}NbO_3$ (e) $[210]_c$ zone axis diffraction pattern of $Ag_{0.97}Nd_{0.01}Ta_{0.20}Nb_{0.80}O_3$. (f) Bright field TEM image of domains in a grain of $Ag_{0.97}Nd_{0.01}Ta_{0.20}Nb_{0.80}O_3$.[366]

the transformation from FE to RFE. Simultaneously, average *G* was reduced from ~10 μm (BF−BT) to ~2 μm (Nd doped BF−BT). As a result, enhanced W_{rec} ~ 1.8 J cm^{-3} was obtained for 15 mol % Nd doped BF−BT, which was further improved to 6.74 J cm^{-3} by multilayering (Figure 37b,c)[90] with similar optimization reported in BF doped with $Bi(Zn_{2/3}Nb_{1/3})O_3$ and $Bi(Zr_{0.5}Zn_{0.5})O_3$.[34,266] The same design strategy of inducing an RFE state is also used in thin film BF−BT−ST compositions.[452]

In summary, the inferior energy storage performance of all FEs can be improved by forcing a RFE state through strategic doping or alloying, Figure 38.[34,66,90,92,199,204,272] P_{max} is often unsaturated in RFE and increases with *E* which means ΔP is not only a function of the slimness of the *P*−*E* loop but also of the applied *E*. RFEs are therefore, among the most promising candidates for capacitors in power electronics (E_{max} > 300 kV cm^{-1}).

4.2. Optimization of Antiferroelectrics

Many recent publications have focused on optimization of energy storage in lead-free AN-based materials,[347,353] although similar strategies date back to early studies of lead-based PLZT and PLZST AFE ceramics.[118,126,143−145] The most comprehensive study of AN AFE ceramics was performed by Lu and coworkers in which they used A and B-site substitutions to develop, $Ag_{0.97}Nd_{0.01}Nb_{0.80}Ta_{0.20}O_3$ which yielded W_{rec} ~ 6.5 J cm^{-3} at 370 kV cm^{-1} with η~ 71%, Figure 39.[366] In their study, Lu and co-workers defined several key points required to optimize AN-based ceramics:

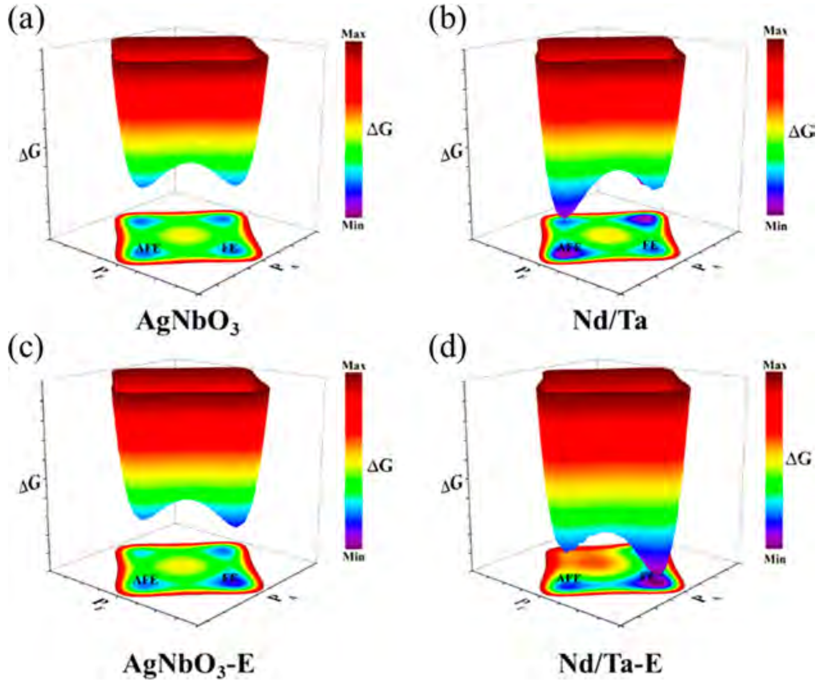

Figure 41. Schematic contour diagrams of the free energy difference (ΔG) for (a) AN- and (b) Nd/Ta-codoped AN without electric field. Schematic contour diagrams of GLD phenomenological theory of AFE-to-FIE phase transition for (c) AN- and (d) Nd/Ta-codoped AN under application of electric field.[366]

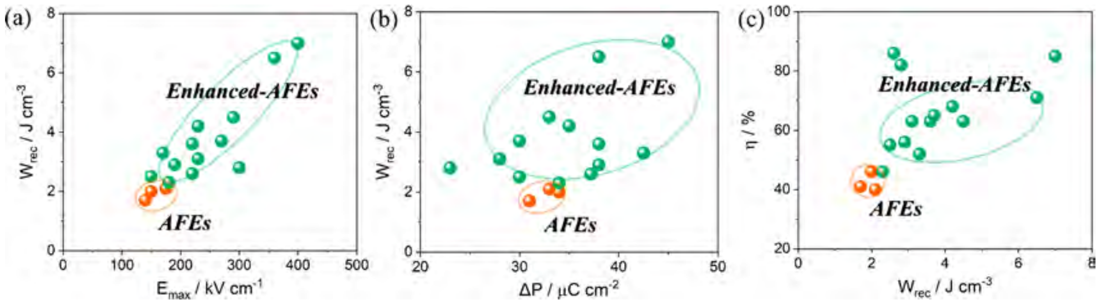

Figure 42. (a) E_{max} vs W_{rec} and (b) ΔP vs W_{rec} and (c) W_{rec} vs η for AFEs and stabilized AFEs bulk ceramics to demonstrate the AFE stabilized optimization.

i) Optimization of P_{max} through local strain/field coupling around the smaller (with respect to Ag) Nd ion the A-site and its compensating V_A, Figure 39a.

ii) Stabilization of the AFE structure through a combination of Nd and Ta doping which leads the induced AFE/FE transition to higher fields. Figure 39(a).

iii) Inducing a slim hysteresis curve in the field induced region of the P−E loop. This was also achieved, through Nd doping that disrupted polar and antipolar coupling which manifested itself as a decrease in domain width from ∼1 to 0.5 μm and streaking of $\pm 1/4(001)_c$ superstructure reflections in electron diffraction patterns for $x = 0.03$, Figure 40.

All the above maximize the area of the P−E loop to the left of the curve in the positive quadrant and thus optimize W_{rec}, Figure 39b,c.

Stabilization of the AFE structure was also confirmed by First-principles calculation and Ginzburg−Landau−Devonshire (GLD) phenomenology, as illustrated in Figure 41.

Figure 42 summarizes the properties for many AFE systems. Most conventional AFEs exhibit low W_{rec} (∼1.5−2 J cm^{-3}) and η (∼40%), which can be optimized to $W_{rec} > 3$ J cm^{-3} and $\eta >$ 50% (enhanced-AFEs) by strategies described in the work of Lu and others.[348,350−352,357,359,363,366] Similar values of ΔP (30−40 μC cm^{-2}) are found for AFEs and enhanced-AFEs which reflects an intrinsic limitation of AFE materials, i.e. when antiparallel polar coupling is fully switched to polar under electric field, P_{max} reaches saturation and is difficult to enhance unlike for RFEs (section 4.1). η is also difficult to further improve (>80%) due to the hysteresis above the AFE/FE switching field. However, at intermediate electric fields (∼300 kV cm^{-1}), much higher ΔP and W_{rec} are obtained for AFEs compared with RFEs, indicating that AFEs are more suitable for low/intermediate-voltage energy storage applications.

4.3. Other Strategies

4.3.1. Chemical Coating. Chemical coating is commonly reported as a strategy to optimize energy storage properties in BT ceramics. In general, chemical coatings are synthesized and applied using wet-chemical and sol−gel methods.[69,74,79−81] Smaller grain sizes are typically obtained (on the order of a few nm), leading to the enhanced density and BDS. BT ceramics, for example, with a 4 nm thick SiO$_2$ coating, have a good value of

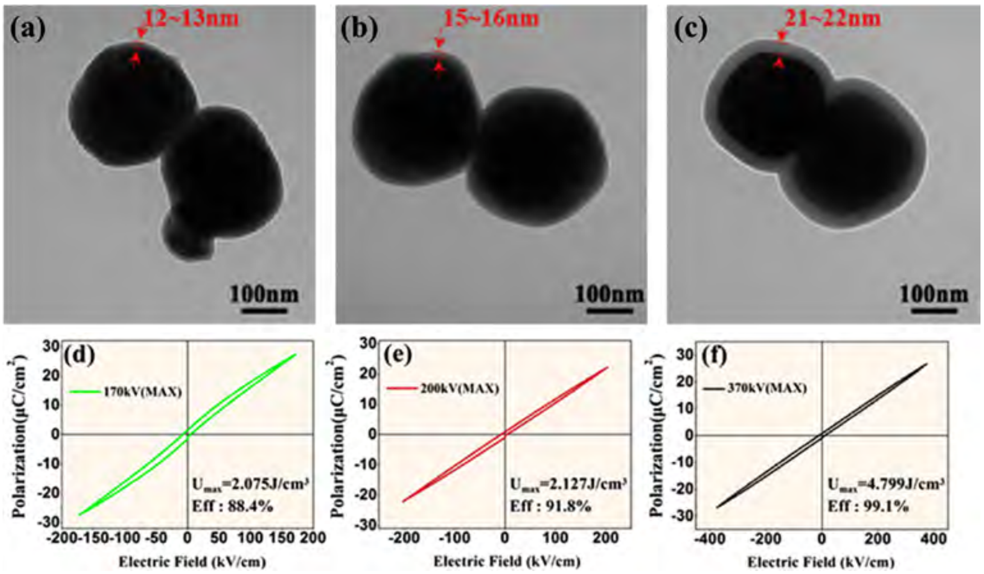

Figure 43. (a−c) TEM micrographs of BTnanoparticles coated with SiO_2: (a) BT@10 wt %SiO_2; (b) BT@15 wt %SiO_2; (c) BT@20 wt %SiO_2. The shell region is defined by red arrows and dash lines. Bipolar $P-E$ loops of BT with (d) 10 wt % (e) 15 wt % (f) 20 wt % SiO_2 composite ceramics at the highest applied electric field, measured at 10 Hz and room temperature. Reproduced with permission from ref 88. Copyright 2019 Elsevier.

Table 14. Energy Storage Performance of Chemically Coated Materials

materials	coating/thickness	E_{max} (kV cm^{-1})	W_{rec} (J cm^{-3})	η (%)	G (nm)	ref
BT	Al_2O_3/2 nm	108	0.51	80	~160	80
BT	La_2O_3 SiO_2/20 nm	136	0.54	85	~250	184
BT	$BiScO_3$/ 4 nm	120	0.68	81	~100	500
BT	SiO_2 and Al_2O_3/6 nm	190	0.725	80	~80	73
BT	SiO_2/10 nm	200	1.2	53.8	~200	501
BT	SiO_2/4 nm	290	1.43	53	~120	86
$Pb_{0.97}La_{0.02}(Zr_{0.33}Sn_{0.55}Ti_{0.12})O_3$	SiO_2/2 nm	238	2.68	95	~180	87
BT	SiO_2/21 nm	370	4.799	95	~220	88
$Pb_{0.91}La_{0.06}(Zr_{0.552}Sn_{0.368}Ti_{0.08})O_3$	$PbO-B_2O_3-SiO_2-Al_2O_3-ZnO-MnO_2$/4 nm	402	7.4		~250	77

W_{rec} (~1.43 J cm^{-3}),[233] in which SiO_2 coating inhibits grain growth, thereby modifying the microstructure and reducing DC current leakage. The effect of SiO_2 layer thickness on BT particles has been systematically investigated (Figure 43a-c). The highest W_{rec}(~4.8 J cm^{-3}) and η (~99.1%) were obtained for 20 wt % SiO_2 coated BT, as shown in Figure 43d−f.[88] Other coating materials such as Al_2O_3 and La_2O_3,[80,184] are also reported to optimize energy storage properties, as listed in Table 14.

4.3.2. Layered Structure. Layer-structures composed of multiple materials have been reported to optimize energy storage properties and are typically tape cast, followed by lamination. Both BDS and ε_r are optimized with the final properties related to the type of electroceramic material and the thickness of each layer. The BDS of BT-based ceramics was enhanced to >300 kV cm^{-1} by laminating layers between BT−x wt % SiO_2 layers (t ~ 20 μm) and BT layer (t ~ 25 μm).[441] ε_r decreased but this was compensated by an increased BDS with increasing SiO_2 concentration in the BT−x wt % SiO_2 layers. ST + Li_2CO_3 (t ~ 50 μm) and 0.93NBT−$0.07Ba_{0.94}La_{0.04}Zr_{0.02}Ti_{0.98}O_3$ (t ~ 33 μm) layered structure were also fabricated via tape-casting with improved W_{rec} ~ 2.72 J cm^{-3} at 294 kV cm^{-1}.[502] Enhanced W_{rec} ~ 2.41 J cm^{-3} at 237 kV cm^{-3} was also obtained for layer-structure ceramics with ST + Li_2O_3 (t ~ 50 μm) and NBT−0.06BT (t ~ 50 μm), Figure 44a.b.[442] The interface between the ST + Li_2O_3 and the NBT−0.06BT layer was further investigated using the finite element analysis. BDS was improved by reducing the breakdown paths between the ST + Li_2O_3 and the NBT−0.06BT layer, Figure 44c−e[442] with electrical field redistribution and interface blocking playing essential roles.[503] BDS was also influenced by the difference in ε_r and thickness ratio between the adjacent layers.

5. SUMMARY AND PERSPECTIVES

5.1. Lead-Based Energy Storage Ceramics

Lead-based ceramics have great potential as energy storage materials in modern microelectronics where high voltage and temperature are required, such as in pulsed power and power electronic applications. Lead-based AFE-type ceramics exhibit extremely high energy density but optimizing BDS, η and minimizing electrostrain is problematic. Low BDS (<300 kV cm^{-1}) is often attributed to the volatilisation of lead/lead oxide which leads the formation of lead vacancy ($V_{pb}^{''}$) and $V_{O}^{\cdot\cdot}$ that results in current leakage. Such issues may be partially solved by a combination of improved processing and dopants but achieving the values of BDS observed in lead-free materials has proved elusive. The low η in lead-based AFE-type ceramics (<80%) is mainly a result of opening of the hysteresis loop at high field due to the stabilization of a field induced FE phase. This results in a change in crystal class from tetragonal (AFE_T)

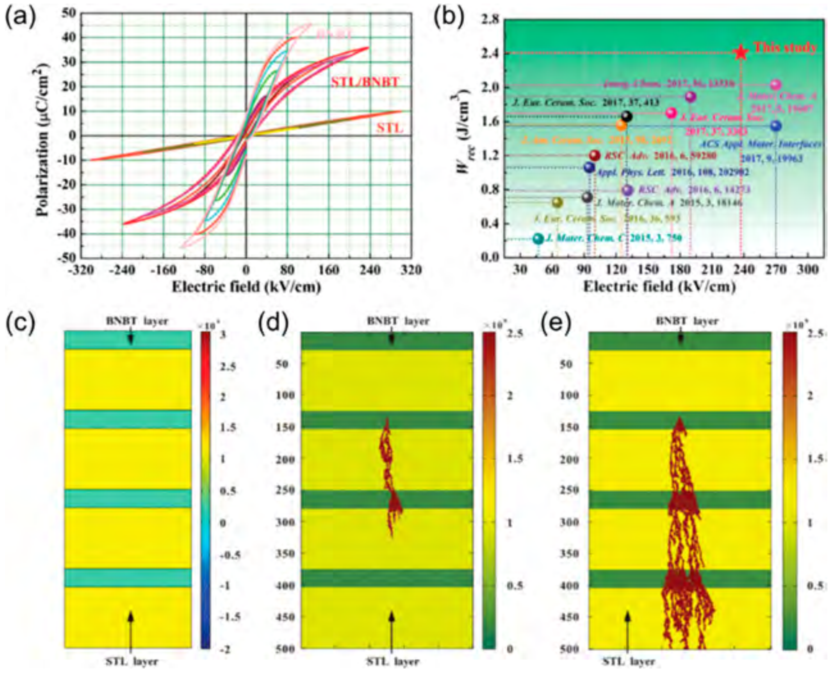

Figure 44. (a) Bipolar *P*−*E* loops of the ST+Li_2O_3, NBT−0.06BT and ST + Li_2O_3/NBT−0.06BT ceramic MLs. (b) Comparison of W_{rec} and electric field between the ST + Li_2O_3/NBT−0.06BT ceramic MLs and some recently reported lead-free ceramics. (c) Distribution of the electric field at 200 kV cm^{-1}, model of electrical tree propagation simulated using the finite element method for the ST + Li_2O_3/NBT−0.06BT MLs ceramic under (d) 200 kV cm^{-1} and (e) 250 kV cm^{-1}. Reproduced with permission from ref 442. Copyright 2018 Royal Society of Chemistry.

to rhombohedral (FE_R) giving large strains (>0.3%) which may prevent long-term cycling through mechanical fatigue.

The lack of popularity in researching lead-based compared with lead-free materials in the academic community has meant that exploration of novel systems is rather limited, but there are, for example, interesting mixed Pb- and Bi-based systems with high ε_r and a spontaneous polarization that would mirror some of the design principles adopted in lead-free ceramics, particularly in solid solutions which combine AFEs and relaxor end members. In addition, further work is required to understand crystal structure and phase transition behavior. Many systems have incommensurate modulations and their influence on AFE/FE switching needs to be explored further using *in situ* XRD and Raman (temperature/electric field), as well as utilizing advanced aberration corrected TEM to study the local structure.

5.2. Lead-Free Energy Storage Ceramics

Lead-free candidates, including BT, ST, BF, KNN, NBT, AN and NN-based systems, are extensively studied and summarized in this review. Research into lead-free materials far outweighs that in lead-based, due to how the potential environmental legislation surrounding manufacturing and the end use of lead-based products has influenced funding bodies and awards. As a result, the optimization of energy storage properties has progressed rapidly in the last 5 years. Successful strategies to improve properties include, disrupting long-range polar coupling particularly if the average ionic polarizability is increased or unaffected, construction relaxor feature (PNRs) in FEs and AFEs, enhancing E_g and as a consequence E_a, reducing the total electrical conductivity and promoting electrical homogeneity through the use of strategic dopants to modify defect chemistry. If these strategies are married with a reduction in the dielectric layer thickness, high values of W_{rec} ∼ 20 J cm^{-3} and η ∼ 90% can be achieved. Recent work on texturing of ceramic MLs has also proved successful in enhancing W_{rec} but the complexity of this approach may inhibit commercial uptake. However, the two overriding issues with the majority of lead-free compositions, particularly those whose W_{rec} are >10 J cm^{-3} are (i) the need to find an effective low cost internal electrode system that permits their commercial exploitation (currently almost all ML data is quoted with Pt internal electrodes) and (ii) pushing their operating window to >200 °C and >100 Hz. Interestingly, electrostrain, a major drawback in lead-based materials, is broadly speaking not an issue in most of the lead-free RFEs and AFEs since the measured values of strain are often significantly lower (<0.2%) even at high fields. As with lead containing ceramics, there are only a few comprehensive investigations of the energy storage mechanisms which require high field *in situ* studies to be performed. A greater understanding of the role of defect chemistry, doping and alloying is also required, particular on how this influences, E_g, resistivity and electrical homogeneity, and thus the W_{rec} and η, thermal stability and cyclic reliability. In addition, in commercial MLCCs, the ripple current, equivalent series *R*, failure mode, voltage rating, the reliability in high humidity need to be evaluated and explored.

5.3. Glass Ceramics

Glass-ceramics have the advantages of facile manufacture, high W_{rec}, ultrahigh η (low energy dissipation), ultrafast charge−discharge speed, excellent temperature/frequency stability. However, there are still challenges/problems. Generally, increasing the volume fraction of the crystal phase will increase the ε/P but decrease BDS. It is critical to balance the ε_r and BDS to obtain the highest W_{rec}. The mechanism of crystallization and control of crystal phase/microstructure is still ambiguous, which should be further investigated using, advanced TEM and *in situ* XRD/TEM as a function of applied field and temperature. Furthermore, although the theoretical W_{rec} (>15 J cm^{-3}, due to ultrahigh BDS, >1100 kV cm^{-1}) of glass-ceramics are much higher than other bulk ceramics and even MLs (15−20 J cm^{-3}), the measured/calculated W_{rec} by $P-E$ loops and discharging processes is low (<2 J cm^{-3}) due to the lower applied electric fields. As a result, we recommend using the same test method ($P-E$ loops and discharging process) to evaluate the practical energy storage performance for glass-ceramics, consistent with other dielectrics.

AUTHOR INFORMATION

Corresponding Authors

Dawei Wang − *Department of Materials Science and Engineering, University of Sheffield, Sheffield S1 3JD, U.K.; Shenzhen Institute of Advanced Electronic Materials, Shenzhen Institute of Advanced Technology, Chinese Academy of Sciences, Shenzhen 518055, China;* orcid.org/0000-0001-6957-2494; Email: wangdawei102@gmail.com

Shujun Zhang − *Institute for Superconducting and Electronic Materials, Australian Institute for Innovative Materials, University of Wollongong, Wollongong, NSW 2500, Australia;* orcid.org/0000-0001-6139-6887; Email: shujun@uow.edu.au

Ian M Reaney − *Department of Materials Science and Engineering, University of Sheffield, Sheffield S1 3JD, U.K.;* orcid.org/0000-0003-3893-6544; Email: i.m.reaney@sheffield.ac.uk

Authors

Ge Wang − *Department of Materials Science and Engineering, University of Sheffield, Sheffield S1 3JD, U.K.;* orcid.org/0000-0003-1842-8067

Zhilun Lu − *Department of Materials Science and Engineering, University of Sheffield, Sheffield S1 3JD, U.K.; The Henry Royce Institute, Sheffield S1 3JD, U.K.*

Yong Li − *Inner Mongolia Key Laboratory of Ferroelectric-related New Energy Materials and Devices, School of Materials and Metallurgy, Inner Mongolia University of Science and Technology, Baotou 014010, China*

Linhao Li − *Department of Materials Science and Engineering, University of Sheffield, Sheffield S1 3JD, U.K.*

Hongfen Ji − *Department of Materials Science and Engineering, University of Sheffield, Sheffield S1 3JD, U.K.; Laboratory of Thin Film Techniques and Optical Test, Xi'an Technological University, Xi'an 710032, China*

Antonio Feteira − *Christian Doppler Laboratory for Advanced Ferroic Oxides, Sheffield Hallam University, Sheffield S1 1WB, U.K.*

Di Zhou − *Electronic Materials Research Lab, Key Lab of Education Ministry/International Center for Dielectric Research, School of Electronic and Information Engineering, Xi'an Jiaotong University, Xi'an 710049, China;* orcid.org/0000-0001-7411-4658

Complete contact information is available at:
https://pubs.acs.org/10.1021/acs.chemrev.0c01264

Author Contributions

‡G.W., Z.L., and Y. L. contributed equally to this work.

Notes

The authors declare no competing financial interest.

Biographies

Dr. Ge Wang is currently working as a postdoctoral research associate in the Functional Materials and Devices group at the University of Sheffield (UK). He obtained his Ph.D. degree from the Department of Materials at the University of Manchester in 2017, specifically on functional and structural behavior of lead-free ferroelectrics. His research focuses on ferroelectric, piezoelectric, energy density ceramic capacitors, lithium-ion batteries, high entropy oxide materials, and structural analysis using synchrotron X-ray diffraction.

Dr. Zhilun Lu obtained his Ph.D. from the Department of Materials Science and Engineering at the University of Sheffield, in January 2016 with the High-Quality PhD Thesis Prize. He worked as a research scientist in Helmholtz-Zentrum Berlin before joining The Henry Royce Institute and Department of Materials Science and Engineering at the University of Sheffield. His work focuses on functional and energy materials such as thermoelectrics, dielectrics, high permittivity oxides, microwaves, and geometrically frustrated magnets. He has expertise in ceramics synthesis and structural and property characterization. His paper "Superior energy density through tailored dopant strategies in multilayer ceramic capacitors" was selected as a HOT Article in *Energy & Environmental Science.*

Dr. Yong Li is an Associate Professor at School of Materials and Metallurgy, Inner Mongolia University of Science and Technology. He received his PhD degree in Materials Science and Engineering from Beijing Institute of Technology in 2016. His research focuses on ferroelectric and multiferroic materials for energy storage, photoelectric conversion, and microwave attenuation.

Dr. Linhao Li obtained his Ph.D. in 2017 from the Department of Materials Science and Engineering at the University of Sheffield under the supervision of Professor Derek C. Sinclair. After graduation, he continued his research in Sheffield as a PDRA. Linhao's expertise is probing the composition−structure−electrical/thermal property relationships of functional materials, particularly using impedance spectroscopy. His current research focuses mainly on developing new materials for energy and electronic applications.

Dr. Hongfen Ji received her Ph.D. degree in 2013 in electronics science and technology from Xi'an Jiaotong University, Shaanxi, China. She has held visiting appointments at Department of Materials Science and Engineering, University of Sheffield, UK (2019−2020). Currently, she works as lecturer in the Laboratory of Thin Film Techniques and Optical Test, and School of Optoelectronic Engineering, Xi'an Technological University, China. Her main research interests are in lead-free piezoelectric and ferroelectric films and ceramics, and functional devices based on piezoelectric and ferroelectric materials.

Prof. Antonio Feteira is currently a Professor of Advanced Functional Materials at Sheffield Hallam University. He received his Ph.D. degree in Materials Science and Engineering from The University of Sheffield, where he holds a visiting position. In the past, he was a Senior Research Fellow at the University of Birmingham, having previously worked in the R&D department of TDK EPC, Austria. He held visiting research positions at Penn State University, Warwick University, Max Planck Institute, and Complutense University of Madrid, UFPeL. His research focuses on advanced ceramics for electronics, including actuators, energy storage devices, temperature sensors and wireless communication resonators. He is an Associate Editor for the *Journal of the American Ceramic Society* and the *Journal of Electronic Materials* and Editor for the *International Journal of Applied Ceramic Technology.*

Prof. Di Zhou is a professor at the School of Electronic and Information Engineering at Xi'an Jiaotong University (China). He received his Ph.D. degree in Electronic Science and Technology from Xi'an Jiaotong

University in 2009 under the guidance of Prof. Dr Xi Yao and won the National Excellent Ph.D. Thesis Award nomination. He was a joint Ph.D. student at the Materials Research Institute. Pennsylvania State University from 2008 to 2009 and a research associate from 2015 tp 2018 at the Department of Materials Science and Engineering, University of Sheffield. He is an Associate Editor of the *Journal of the American Ceramic Society* and *International Journal of Applied Ceramic Technology*, Editorial Board Member of *Materials Research Bulletin* and *Journal of Advanced Dielectrics*, and Editorial Advisory Board member of *ACS Applied Materials & Interfaces*. His research interests include microwave dielectric materials, low temperature cofired ceramics technology (LTCC), energy storage capacitor materials, microwave absorption materials, and functional composite materials for high frequency communication/energy storage/microwave absorption.

Prof Dawei Wang is a Professor at Shenzhen Institute of Advanced Electronic Materials, Shenzhen Institute of Advanced Technology, Chinese Academy of Sciences. Previously, he was a Research Associate at the Department of Materials Science and Engineering of the University of Sheffield (2014−2020) and a visiting scholar at the Materials Research Institute of Pennsylvania State University (2016). He received his Ph.D. degree in Materials Processing Engineering from Beijing Institute of Technology in 2012. He is an associate editor for *Journal of American Ceramic Society* and *Frontiers in Materials*. His research focuses on the advanced electronic ceramics for energy storage/conversion/harvesting and translation of new materials to prototype devices/components for electronic systems.

Prof Shujun Zhang is a Professor at ISEM/AIIM of UOW, prior to which, he was a Professor at MatSE Department and Senior Scientist at MRI of Pennsylvania State University. He is the Associate EIC of *IEEE Transaction UFFC* and Associate Editor of *Science Bulletin*, *Journal ACerS*, *Journal Electronic Materials*, and section EIC of *Crystals*. He is a fellow of IEEE and ACerS, elected AdCom member of IEEE-UFFC. He is now focusing on fabrication microstructure−property-performance relationship of functional materials for piezoelectric sensors, transducers, and energy storage/harvesting applications.

Prof. Ian M. Reaney FIMM FRMS holds the Dyson Chair in Ceramics and leads the Functional Materials & Devices Group in the Department of Materials Science & Engineering, University of Sheffield. He is a Fellow of the Royal Microscopical Society and the Institute of Materials, Minerals and Mining (IOM3). He has won numerous awards including the Verulam Medal (2017) in Ceramics from IOM3 and was recently elected to the World Academy of Ceramics. He is an Adjunct Professor at Pennsylvania State University (PSU) and European site director of the Centre for Dielectrics and Piezoelectrics in partnership with PSU and North Carolina State University.

ACKNOWLEDGMENTS

This work was supported by the Engineering and Physical Sciences Research Council (EP/L017563/1 and EP/N010493/1), Henry Royce Institute for Advanced Materials, funded through EPSRC grants EP/R00661X/1, EP/S019367/1, EP/P02470X/1, and EP/P025285/1, and the National Natural Science Foundation of China (51602060 and 51402005). The authors are grateful for support provided by Functional Materials and Devices group from University of Sheffield.

REFERENCES

(1) Report of the Secretary-General on the 2019 Climate Action Summit and the Way Forward in 2020. *Climate Action Summit* 2019.

(2) Ibn-Mohammed, T.; Randall, C. A.; Mustapha, K. B.; Guo, J.; Walker, J.; Berbano, S.; Koh, S. C. L.; Wang, D.; Sinclair, D. C.; Reaney, I. M. Decarbonising Ceramic Manufacturing: A Techno-Economic Analysis of Energy Efficient Sintering Technologies in the Functional Materials Sector. *J. Eur. Ceram. Soc.* **2019**, *39*, 5213−5235.

(3) Yao, Z.; Song, Z.; Hao, H.; Yu, Z.; Cao, M.; Zhang, S.; Lanagan, M. T.; Liu, H. Homogeneous/Inhomogeneous-Structured Dielectrics and Their Energy-Storage Performances. *Adv. Mater.* **2017**, *29*, 1601727.

(4) Sherrill, S. A.; Banerjee, P.; Rubloff, G. W.; Lee, S. B. High to Ultra-High Power Electrical Energy Storage. *Phys. Chem. Chem. Phys.* **2011**, *13*, 20714−20723.

(5) Liu, C.; Li, F.; Ma, L.-P.; Cheng, H.-M. Advanced Materials for Energy Storage. *Adv. Mater.* **2010**, *22*, E28−E62.

(6) Liu, C.; Yu, Z.; Neff, D.; Zhamu, A.; Jang, B. Z. Graphene-Based Supercapacitor with an Ultrahigh Energy Density. *Nano Lett.* **2010**, *10*, 4863−4868.

(7) Snook, G. A.; Kao, P.; Best, A. S. Conducting-Polymer-Based Supercapacitor Devices and Electrodes. *J. Power Sources* **2011**, *196*, 1−12.

(8) Zhu, Y.; Murali, S.; Stoller, M. D.; Ganesh, K. J.; Cai, W.; Ferreira, P. J.; Pirkle, A.; Wallace, R. M.; Cychosz, K. A.; Thommes, M.; et al. Carbon-Based Supercapacitors Produced by Activation of Graphene. *Science* **2011**, *332*, 1537−1541.

(9) Wang, W.; Jiang, B.; Xiong, W.; Sun, H.; Lin, Z.; Hu, L.; Tu, J.; Hou, J.; Zhu, H.; Jiao, S. A New Cathode Material for Super-Valent Battery Based on Aluminium Ion Intercalation and Deintercalation. *Sci. Rep.* **2013**, *3*, 3383.

(10) Sun, H.; Wang, W.; Yu, Z.; Yuan, Y.; Wang, S.; Jiao, S. A New Aluminium-Ion Battery with High Voltage, High Safety and Low Cost. *Chem. Commun.* **2015**, *51*, 11892−11895.

(11) Wang, S.; Yu, Z.; Tu, J.; Wang, J.; Tian, D.; Liu, Y.; Jiao, S. A Novel Aluminum-Ion Battery: Al/AlCl$_3$-[Emim]Cl/Ni$_3$S$_2$@Graphene. *Adv. Energy Mater.* **2016**, *6*, 1600137.

(12) Jiao, H.; Wang, C.; Tu, J.; Tian, D.; Jiao, S. A Rechargeable Al-Ion Battery: Al/Molten AlCl$_3$-Urea/Graphite. *Chem. Commun.* **2017**, *53*, 2331−2334.

(13) Song, Y.; Jiao, S.; Tu, J.; Wang, J.; Liu, Y.; Jiao, H.; Mao, X.; Guo, Z.; Fray, D. J. A Long-Life Rechargeable Al Ion Battery Based on Molten Salts. *J. Mater. Chem. A* **2017**, *5*, 1282−1291.

(14) Wang, S.; Jiao, S.; Wang, J.; Chen, H.-S.; Tian, D.; Lei, H.; Fang, D.-N. High-Performance Aluminum-Ion Battery with Cus@C Microsphere Composite Cathode. *ACS Nano* **2017**, *11*, 469−477.

(15) Yu, Z.; Jiao, S.; Li, S.; Chen, X.; Song, W.-L.; Teng, T.; Tu, J.; Chen, H.-S.; Zhang, G.; Fang, D.-N. Flexible Stable Solid-State Al-Ion Batteries. *Adv. Funct. Mater.* **2019**, *29*, 1806799.

(16) Zhang, X.; Jiao, S.; Tu, J.; Song, W.-L.; Xiao, X.; Li, S.; Wang, M.; Lei, H.; Tian, D.; Chen, H.; et al. Rechargeable Ultrahigh-Capacity Tellurium-Aluminum Batteries. *Energy Environ. Sci.* **2019**, *12*, 1918−1927.

(17) Kishi, H.; Mizuno, Y.; Chazono, H. Base-Metal Electrode-Multilayer Ceramic Capacitors: Past, Present and Future Perspectives. *Jpn. J. Appl. Phys.* **2003**, *42*, 1−15.

(18) Pan, M.; Randall, C. A. A Brief Introduction to Ceramic Capacitors. *IEEE Electrical Insulation Magazine* **2010**, *26*, 44−50.

(19) Wang, D.; Zhou, D.; Song, K.; Feteira, A.; Randall, C. A.; Reaney, I. M. Cold-Sintered C0G Multilayer Ceramic Capacitors. *Adv. Electron. Mater.* **2019**, *5*, 1900025.

(20) Sakabe, Y. Multilayer Ceramic Capacitors. *Curr. Opin. Solid State Mater. Sci.* **1997**, *2*, 584−587.

(21) Yamamatsu, J.; Kawano, N.; Arashi, T.; Sato, A.; Nakano, Y.; Nomura, T. Reliability of Multilayer Ceramic Capacitors with Nickel Electrodes. *J. Power Sources* **1996**, *60*, 199−203.

(22) Saito, H.; Chazono, H.; Kishi, H.; Yamaoka, N. X7R Multilayer Ceramic Capacitors with Nickel Electrodes. *Jpn. J. Appl. Phys.* **1991**, *30*, 2307−2310.

(23) Christen, T.; Carlen, M. W. Theory of Ragone Plots. *J. Power Sources* **2000**, *91*, 210−216.

(24) Yano, M.; Uchida, R. History of Power Electronics in Japan. *IEEJ. Transactions on Fundamentals and Materials* **2001**, *121*, 2−10.

(25) Whittingham, M. S. Materials Challenges Facing Electrical Energy Storage. *MRS Bull.* **2008**, *33*, 411−419.

(26) Li, Q.; Liu, F.; Yang, T.; Gadinski, M. R.; Zhang, G.; Chen, L.-Q.; Wang, Q. Sandwich-Structured Polymer Nanocomposites with High Energy Density and Great Charge-Discharge Efficiency at Elevated Temperatures. *Proc. Natl. Acad. Sci. U. S. A.* **2016**, *113*, 9995.

(27) National Physical Laboratory. New Capacitors to Improve Electric Vehicles. *Phys. Org.* **2013**.

(28) Jaffe, B. Antiferroelectric Ceramics with Field-Enforced Transitions: A New Nonlinear Circuit Element. *Proc. IRE* **1961**, *49*, 1264−1267.

(29) Burn, I.; Smyth, D. M. Energy Storage in Ceramic Dielectrics. *J. Mater. Sci.* **1972**, *7*, 339−343.

(30) Love, G. R. Energy Storage in Ceramic Dielectrics. *J. Am. Ceram. Soc.* **1990**, *73*, 323−328.

(31) Yang, L.; Kong, X.; Li, F.; Hao, H.; Cheng, Z.; Liu, H.; Li, J.-F.; Zhang, S. Perovskite Lead-Free Dielectrics for Energy Storage Applications. *Prog. Mater. Sci.* **2019**, *102*, 72−108.

(32) Fletcher, N. H.; Hilton, A. D.; Ricketts, B. W. Optimization of Energy Storage Density in Ceramic Capacitors. *J. Phys. D: Appl. Phys.* **1996**, *29*, 253−258.

(33) Ogihara, H.; Randall, C. A.; Trolier-McKinstry, S. High-Energy Density Capacitors Utilizing 0.7batio$_3$-0.3bisco$_3$ Ceramics. *J. Am. Ceram. Soc.* **2009**, *92*, 1719−1724.

(34) Wang, G.; Li, J.; Zhang, X.; Fan, Z.; Yang, F.; Feteira, A.; Zhou, D.; Sinclair, D. C.; Ma, T.; Tan, X.; et al. Ultrahigh Energy Storage Density Lead-Free Multilayers by Controlled Electrical Homogeneity. *Energy Environ. Sci.* **2019**, *12*, 582−588.

(35) Damjanovic, D. Ferroelectric, Dielectric and Piezoelectric Properties of Ferroelectric Thin Films and Ceramics. *Rep. Prog. Phys.* **1998**, *61*, 1267−1324.

(36) Bokov, A. A.; Ye, Z. G. Recent Progress in Relaxor Ferroelectrics with Perovskite Structure. *J. Mater. Sci.* **2006**, *41*, 31−52.

(37) Prume, K.; Schmitz, T.; Tiedke, S. In *Polar Oxides: Properties, Characterization, and Imaging*; Waser, R., Böttger, U., Tiedke, S., Eds.; Wiley, 2004.

(38) Wang, L.-M. Relationship between Intrinsic Breakdown Field and Bandgap of Materials. *2006 25th International Conference on Microelectronics* **2006**, 576−579.

(39) Wang, D.; Wang, G.; Lu, Z.; Al-Jlaihawi, Z.; Feteira, A. Crystal Structure, Phase Transitions and Photoferroelectric Properties of KNbO$_3$-Based Lead-Free Ferroelectric Ceramics: A Brief Review. *Front. Mater.* **2020**, *7*, 91.

(40) Neudeck, P. G.; Okojie, R. S.; Chen, L.-Y. High-Temperature Electronics - a Role for Wide Bandgap Semiconductors? *Proceedings of the IEEE* **2002**, *90*, 1065−1076.

(41) Dyalsingh, H. M.; Kakalios, J. Thermopower and Conductivity Activation Energies in Hydrogenated Amorphous Silicon. *Phys. Rev. B: Condens. Matter Mater. Phys.* **1996**, *54*, 7630−7633.

(42) Qi, H.; Zuo, R.; Xie, A.; Tian, A.; Fu, J.; Zhang, Y.; Zhang, S. Ultrahigh Energy-Storage Density in NaNbO$_3$-Based Lead-Free Relaxor Antiferroelectric Ceramics with Nanoscale Domains. *Adv. Funct. Mater.* **2019**, *29*, 1903877.

(43) Qi, H.; Xie, A.; Tian, A.; Zuo, R. Superior Energy-Storage Capacitors with Simultaneously Giant Energy Density and Efficiency Using Nanodomain Engineered BiFeO$_3$-BaTiO$_3$-NaNbO$_3$ Lead-Free Bulk Ferroelectrics. *Adv. Energy Mater.* **2020**, *10*, 1903338.

(44) Irvine, J. T. S.; Sinclair, D. C.; West, A. R. Electroceramics: Characterization by Impedance Spectroscopy. *Adv. Mater.* **1990**, *2*, 132−138.

(45) Lu, Z.; Wang, G.; Bao, W.; Li, J.; Li, L.; Mostaed, A.; Yang, H.; Ji, H.; Li, D.; Feteira, A.; et al. Superior Energy Density through Tailored Dopant Strategies in Multilayer Ceramic Capacitors. *Energy Environ. Sci.* **2020**, *13*, 2938−2948.

(46) Morrison, F. D.; Sinclair, D. C.; West, A. R. Doping Mechanisms and Electrical Properties of La-Doped BaTiO$_3$ Ceramics. *Int. J. Inorg. Mater.* **2001**, *3*, 1205−1210.

(47) Li, M.; Pietrowski, M. J.; De Souza, R. A.; Zhang, H.; Reaney, I. M.; Cook, S. N.; Kilner, J. A.; Sinclair, D. C. A Family of Oxide Ion Conductors Based on the Ferroelectric Perovskite Na$_{0.5}$Bi$_{0.5}$TiO$_3$. *Nat. Mater.* **2014**, *13*, 31−35.

(48) Sinclair, D. C.; West, A. R. Impedance and Modulus Spectroscopy of Semiconducting BaTiO$_3$ Showing Positive Temperature Coefficient of Resistance. *J. Appl. Phys.* **1989**, *66*, 3850−3856.

(49) Adams, T. B.; Sinclair, D. C.; West, A. R. Influence of Processing Conditions on the Electrical Properties of CaCu$_3$Ti$_4$O$_{12}$ Ceramics. *J. Am. Ceram. Soc.* **2006**, *89*, 3129−3135.

(50) Yang, F.; Li, M.; Li, L.; Wu, P.; Pradal-Velázquez, E.; Sinclair, D. C. Defect Chemistry and Electrical Properties of Sodium Bismuth Titanate Perovskite. *J. Mater. Chem. A* **2018**, *6*, 5243−5254.

(51) Li, M.; Li, L.; Zang, J.; Sinclair, D. C. Donor-Doping and Reduced Leakage Current in Nb-Doped Na$_{0.5}$Bi$_{0.5}$TiO$_3$. *Appl. Phys. Lett.* **2015**, *106*, 102904.

(52) Smyth, D. M. The Defect Chemistry of Donor-Doped BaTiO$_3$: A Rebuttal. *J. Electroceram.* **2002**, *9*, 179−186.

(53) Chan, N. H.; Sharma, R. K.; Smyth, D. M. Nonstoichiometry in Undoped BaTiO$_3$. *J. Am. Ceram. Soc.* **1981**, *64*, 556−562.

(54) Sumino, H.; Sakurai, O.; Shinozaki, K.; Kato, M.; Mizutani, N. A New Instrument to Measure the Electrical Properties in Very Narrow Regions in Ceramics. *J. Mater. Sci. Lett.* **1991**, *10*, 1026−1028.

(55) Dimos, D.; Chaudhari, P.; Mannhart, J.; LeGoues, F. K. Orientation Dependence of Grain-Boundary Critical Currents in Yba$_2$cu$_3$o$_{7-\Delta}$ Bicrystals. *Phys. Rev. Lett.* **1988**, *61*, 219−222.

(56) Sinclair, D. C. Characterization of Electro-Materials Using Ac Impedance Spectroscopy. *Bol. Soc. Esp. Ceram. Vidrio* **1995**, *34*, 55−65.

(57) Schmidt, R.; Sinclair, D. C. Anomalous Increase of Dielectric Permittivity in Sr-Doped Ccto Ceramics Ca$_{1-X}$ Sr$_x$ Cu$_3$ Ti$_4$O$_{12}$ ($0 \leq X \leq 0.2$). *Chem. Mater.* **2010**, *22*, 6−8.

(58) Li, M.; Feteira, A.; Sinclair, D. C.; West, A. R. Influence of Mn Doping on the Semiconducting Properties of CaCu$_3$Ti$_4$O$_{12}$ Ceramics. *Appl. Phys. Lett.* **2006**, *88*, 232903.

(59) Ray, S. *An Introduction to High Voltage Engineering*; Prentice-Hall of India: New Delhi, 2004.

(60) H, F. On the Theory of Dielectric Breakdown in Solids. *Proc. R Soc. Lond A* **1947**, *188*, 521−532.

(61) Wang, J.; Chen, X.; Wang, J.; Wang, G.; Nie, H.; Cao, F.; Dong, X. Improved Dielectric Breakdown Strength of Pb$_{0.99}$(Zr$_{0.95}$Ti$_{0.05}$)$_{0.98}$Nb$_{0.02}$O$_3$ Ferroelectric Ceramics with the Addition of Cuo. *J. Mater. Sci.: Mater. Electron* **2015**, *26*, 8207−8211.

(62) Pu, Y.; Yao, M.; Zhang, L.; Chen, M. Enhanced Energy Storage Density of 0.55Bi$_{0.5}$Na$_{0.5}$TiO$_3$-0.45Ba$_{0.85}$Ca$_{0.15}$Ti$_{0.85}$Zr$_{0.1}$Sn$_{0.05}$O$_3$ with MgO Addition. *J. Alloys Compd.* **2017**, *702*, 171−177.

(63) Diao, C.; Liu, H.; Hao, H.; Cao, M.; Yao, Z. Effect of SiO2 Additive on Dielectric Response and Energy Storage Performance of Ba$_{0.4}$Sr$_{0.6}$TiO$_3$ Ceramics. *Ceram. Int.* **2016**, *42*, 12639−12643.

(64) Qi, J.; Cao, M.; Heath, J. P.; Dean, J. S.; Hao, H.; Yao, Z.; Yu, Z.; Liu, H. Improved Breakdown Strength and Energy Storage Density of a Ce Doped Strontium Titanate Core by Silica Shell Coating. *J. Mater. Chem. C* **2018**, *6*, 9130−9139.

(65) Dong, G.; Ma, S.; Du, J.; Cui, J. Dielectric Properties and Energy Storage Density in ZnO-Doped Ba$_{0.3}$Sr$_{0.7}$TiO$_3$ Ceramics. *Ceram. Int.* **2009**, *35*, 2069−2075.

(66) Qu, B.; Hongliang, D.; Yang, Z.; Liu, Q. Large Recoverable Energy Storage Density and Low Sintering Temperature in Potassium-Sodium Niobate-Based Ceramics for Multilayer Pulsed Power Capacitors. *J. Am. Ceram. Soc.* **2017**, *100*, 1517−1526.

(67) Yang, L.; Kong, X.; Cheng, Z.; Zhang, S. Enhanced Energy Storage Performance of Sodium Niobate-Based Relaxor Dielectrics by a Ramp-to-Spike Sintering Profile. *ACS Appl. Mater. Interfaces* **2020**, *12*, 32834−32841.

(68) Zhan, D.; Xu, Q.; Huang, D.-P.; Liu, H.-X.; Chen, W.; Zhang, F. Contributions of Intrinsic and Extrinsic Polarization Species to Energy Storage Properties of Ba$_{0.95}$Ca$_{0.05}$Zr$_{0.2}$Ti$_{0.8}$O$_3$ Ceramics. *J. Phys. Chem. Solids* **2018**, *114*, 220−227.

(69) Xu, Q.; Xie, J.; He, Z.; Zhang, L.; Cao, M.; Huang, X.; Lanagan, M. T.; Hao, H.; Yao, Z.; Liu, H. Energy-Storage Properties of Bi$_{0.5}$Na$_{0.5}$TiO$_3$-BaTiO$_3$-KNbO$_3$ Ceramics Fabricated by Wet-Chemical Method. *J. Eur. Ceram. Soc.* **2017**, *37*, 99−106.

(70) Huang, Y. H.; Wu, Y. J.; Li, J.; Liu, B.; Chen, X. M. Enhanced Energy Storage Properties of Barium Strontium Titanate Ceramics

Prepared by Sol-Gel Method and Spark Plasma Sintering. *J. Alloys Compd.* **2017**, *701*, 439−446.

(71) Luo, H.; Ke, H.; Zhang, H.; Zhang, L.; Li, F.; Cao, L.; Jia, D.; Zhou, Y. Enhanced Ferroelectric and Energy-Storage Properties of Nb-Doped $0.94Na_{0.5}Bi_{0.5}TiO_3$-$0.06BaTiO_3$ Ceramics Prepared by a Multi-Ionic Sol-Gel Method. *Phys. B* **2019**, *567*, 17−24.

(72) Li, C.; Yao, M.; Gao, W.; Yao, X. High Breakdown Strength and Energy Density in Antiferroelectric PLZST Ceramics with Al_2O_3 Buffer. *Ceram. Int.* **2020**, *46*, 722−730.

(73) Song, Z.; Zhang, S.; Liu, H.; Hao, H.; Cao, M.; Li, Q.; Wang, Q.; Yao, Z.; Wang, Z.; Lanagan, M. T. Improved Energy Storage Properties Accompanied by Enhanced Interface Polarization in Annealed Microwave-Sintered BST. *J. Am. Ceram. Soc.* **2015**, *98*, 3212−3222.

(74) Cui, C.; Pu, Y. Improvement of Energy Storage Density with Trace Amounts of ZrO_2 Additives Fabricated by Wet-Chemical Method. *J. Alloys Compd.* **2018**, *747*, 495−504.

(75) Jin, Q.; Pu, Y.; Wang, C.; Gao, Z.; Wang, Y.; Zheng, H.; Yao, M. Microstructure, Dielectric Properties and Energy Storage Performance of $Ba_{0.4}Sr_{0.6}TiO_3$ Ceramics Prepared by Hydrothermal Method and Microwave Sintering. *Mater. Lett.* **2017**, *188*, 159−161.

(76) Ma, J.-P.; Chen, X.-M.; Ouyang, W.-Q.; Wang, J.; Li, H.; Fang, J.-L. Microstructure, Dielectric, and Energy Storage Properties of $BaTiO_3$ Ceramics Prepared Via Cold Sintering. *Ceram. Int.* **2018**, *44*, 4436−4441.

(77) Xie, J.; Yao, M.; Gao, W.; Su, Z.; Yao, X. Ultrahigh Breakdown Strength and Energy Density in PLZST@ Pbsazm Antiferroelectric Ceramics Based on Core-Shell Structure. *J. Eur. Ceram. Soc.* **2019**, *39*, 1050−1056.

(78) Zhou, H. Y.; Liu, X. Q.; Zhu, X. L.; Chen, X. M. Catio3 Linear Dielectric Ceramics with Greatly Enhanced Dielectric Strength and Energy Storage Density. *J. Am. Ceram. Soc.* **2018**, *101*, 1999−2008.

(79) Liu, B.; Wang, X.; Zhao, Q.; Li, L. Improved Energy Storage Properties of Fine-Crystalline $BaTiO_3$ Ceramics by Coating Powders with Al_2O_3 and SiO_2. *J. Am. Ceram. Soc.* **2015**, *98*, 2641−2646.

(80) Zhao, Q.; Wang, X.; Gong, H.; Liu, B.; Luo, B.; Li, L. The Properties of Al_2O_3 Coated Fine-Grain Temperature Stable $BaTiO_3$-Based Ceramics Sintered in Reducing Atmosphere. *J. Am. Ceram. Soc.* **2018**, *101*, 1245−1254.

(81) Lai, X.; Hao, H.; Liu, Z.; Li, S.; Liu, Y.; Emmanuel, M.; Yao, Z.; Cao, M.; Wang, D.; Liu, H. Structure and Dielectric Properties of MgO-Coated $BaTiO_3$ Ceramics. *J. Mater. Sci.: Mater. Electron.* **2020**, *31*, 8963−8970.

(82) Tunkasiri, T.; Rujijanagul, G. Dielectric Strength of Fine Grained Barium Titanate Ceramics. *J. Mater. Sci. Lett.* **1996**, *15*, 1767−1769.

(83) Lee, H. Y.; Cho, K. H.; Nam, H.-D. Grain Size and Temperature Dependence of Electrical Breakdown in $BaTiO_3$ Ceramic. *Ferroelectrics* **2006**, *334*, 165−169.

(84) Liu, B.; Wang, X.; Zhang, R.; Li, L. Grain Size Effect and Microstructure Influence on the Energy Storage Properties of Fine-Grained $BaTiO_3$-Based Ceramics. *J. Am. Ceram. Soc.* **2017**, *100*, 3599−3607.

(85) Waser, R. Tri4: The Role of Grain Boundaries in Conduction and Breakdown of Perovskite-Type Titanates. *Ferroelectrics* **1992**, *133*, 109−114.

(86) Lu, X.; Zhang, L.; Talebinezhad, H.; Tong, Y.; Cheng, Z. Y. Effects of Cuo Additive on the Dielectric Property and Energy-Storage Performance of BaTiO3-SiO_2 Ceramic-Glass Composite. *Ceram. Int.* **2018**, *44*, 16977−16983.

(87) Bian, F.; Yan, S.; Xu, C.; Liu, Z.; Chen, X.; Mao, C.; Cao, F.; Bian, J.; Wang, G.; Dong, X. Enhanced Breakdown Strength and Energy Density of Antiferroelectric Pb,La(Zr,Sn,Ti)O_3 Ceramic by Forming Core-Shell Structure. *J. Eur. Ceram. Soc.* **2018**, *38*, 3170−3176.

(88) Xu, C.; Su, R.; Wang, Z.; Wang, Y.; Zhang, D.; Wang, J.; Bian, J.; Wu, C.; Lou, X.; Yang, Y. Tuning the Microstructure of $BaTiO_3$@SiO_2 Core-Shell Nanoparticles for High Energy Storage Composite Ceramics. *J. Alloys Compd.* **2019**, *784*, 173−181.

(89) Zhao, P.; Cai, Z.; Chen, L.; Wu, L.; Huan, Y.; Guo, L.; Li, L.; Wang, H.; Wang, X. Ultra-High Energy Storage Performance in Lead-Free Multilayer Ceramic Capacitors Via a Multiscale Optimization Strategy. *Energy Environ. Sci.* **2020**, *13*, 4882−4890.

(90) Wang, D.; Fan, Z.; Zhou, D.; Khesro, A.; Murakami, S.; Feteira, A.; Zhao, Q.; Tan, X.; Reaney Ian, M. Bismuth Ferrite-Based Lead-Free Ceramics and Multilayers with High Recoverable Energy Density. *J. Mater. Chem. A* **2018**, *6*, 4133−4144.

(91) Shao, T.; Du, H.; Ma, H.; Qu, S.; Wang, J.; Wang, J.; Wei, X.; Xu, Z. Potassium-Sodium Niobate Based Lead-Free Ceramics: Novel Electrical Energy Storage Materials. *J. Mater. Chem. A* **2017**, *5*, 554−563.

(92) Yang, Z.; Du, H.; Qu, S.; Hou, Y.; Ma, H.; Wang, J.; Wang, J.; Wei, X.; Xu, Z. Significantly Enhanced Recoverable Energy Storage Density in Potassium-Sodium Niobate-Based Lead Free Ceramics. *J. Mater. Chem. A* **2016**, *4*, 13778−13785.

(93) Dale, G.; Strawhorne, M.; Sinclair, D. C.; Dean, J. S. Finite Element Modeling on the Effect of Intra-Granular Porosity on the Dielectric Properties of $BaTiO_3$ Mlccs. *J. Am. Ceram. Soc.* **2018**, *101*, 1211−1220.

(94) Heath, J. P.; Dean, J. S.; Harding, J. H.; Sinclair, D. C. Simulation of Impedance Spectra for Core-Shell Grain Structures Using Finite element Modeling. *J. Am. Ceram. Soc.* **2015**, *98*, 1925−1931.

(95) Heath, J. P.; Harding, J. H.; Sinclair, D. C.; Dean, J. S. The Analysis of Impedance Spectra for Core-Shell Microstructures: Why a Multiformalism Approach Is Essential. *Adv. Funct. Mater.* **2019**, *29*, 1904036.

(96) Morshead, F. H.; Foeller, P. Y.; Freeman, C. L.; Zhang, H.; Reaney, I. M.; Sinclair, D. C.; Dean, J. S. How to Extract Reliable Core-Volume Fractions from Core-Shell Polycrystalline Microstructures Using Cross Sectional Tem Micrographs. *J. Eur. Ceram. Soc.* **2017**, *37*, 2795−2801.

(97) Wu, L.; Wang, X.; Li, L. Enhanced Energy Density in Core-Shell Ferroelectric Ceramics: Modeling and Practical Conclusions. *J. Am. Ceram. Soc.* **2016**, *99*, 930−937.

(98) Yuan, J.; Wang, D.-W.; Lin, H.-B.; Zhao, Q.-L.; Zhang, D.-Q.; Cao, M.-S. Effect of ZnO Whisker Content on Sinterability and Fracture Behaviour of PZT Peizoelectric Composites. *J. Alloys Compd.* **2010**, *504*, 123−128.

(99) Wang, D.-W.; Cao, M.-S.; Yuan, J.; Zhao, Q.-L.; Li, H.-B.; Zhang, D.-Q.; Agathopoulos, S. Enhanced Piezoelectric and Ferroelectric Properties of Nb_2O_5 Modified Lead Zirconate Titanate-Based Composites. *J. Am. Ceram. Soc.* **2011**, *94*, 647−650.

(100) Wang, D.; Cao, M.; Zhang, S. Piezoelectric Ceramics in the $PbSnO_3$-$Pb(Mg_{1/3}Nb_{2/3})O_3$-$PbTiO_3$ Ternary System. *J. Am. Ceram. Soc.* **2011**, *94*, 3690−3693.

(101) Zhao, Q. L.; Cao, M. S.; Yuan, J.; Lu, R.; Wang, D. W.; Zhang, D. Q. Thickness Effect on Electrical Properties of $Pb(Zr_{0.52}Ti_{0.48})O_3$ Thick Films Embedded with ZnO Nanowhiskers Prepared by a Hybrid Sol-Gel Route. *Mater. Lett.* **2010**, *64*, 632−635.

(102) Zhang, T. F.; Tang, X. G.; Liu, Q. X.; Jiang, Y. P.; Huang, X. X.; Zhou, Q. F. Energy-Storage Properties and High-Temperature Dielectric Relaxation Behaviors of Relaxor Ferroelectric Pb-$(Mg_{1/3}Nb_{2/3})O_3$-$PbTiO_3$ Ceramics. *J. Phys. D: Appl. Phys.* **2016**, *49*, 095302.

(103) Liu, Z.; Lu, T.; Ye, J.; Wang, G.; Dong, X.; Withers, R.; Liu, Y. Antiferroelectrics for Energy Storage Applications: A Review. *Advanced Materials Technologies* **2018**, *3*, 1800111.

(104) Li, Y.; Sun, N.; Du, J.; Li, X.; Hao, X. Stable Energy Density of a PMN-PST Ceramic from Room Temperature to Its Curie Point Based on the Synergistic Effect of Diversified Energy. *J. Mater. Chem. C* **2019**, *7*, 7692−7699.

(105) Perumal, R. N.; Athikesavan, V. Investigations on Electrical and Energy Storage Behaviour of PZN-PT, PMN-PT, PZN-PMN-PT Piezoelectric Solid Solutions. *J. Mater. Sci.: Mater. Electron.* **2019**, *30*, 902−913.

(106) Zhang, T.-F.; Tang, X.-G.; Huang, X.-X.; Liu, Q.-X.; Jiang, Y.-P.; Zhou, Q.-F. High-Temperature Dielectric Relaxation Behaviors of Relaxer-Like $PbZrO_3$-$SrTiO_3$ Ceramics for Energy-Storage Applications. *Energy Technology* **2016**, *4*, 633−640.

(107) Bikyashev, E. A.; Ryush, I. O.; Reshetnikova, E. A. Structures of Pb_{1-X} $La_x[Zr_{0.9}$ $Mg_{(0.1+X)/3}$ $Nb_{(0.2-X)/3}]O_3$ Solid Solutions, Electrostriction and Energy Storage Characteristics of a New Antiferroelectric Phase with Disturbed Translational Symmetry. *Ceram. Int.* **2017**, *43*, 1429−1436.

(108) Chao, M.; Liu, J.; Zeng, M.; Wang, D.; Yu, H.; Yuan, Y.; Zhang, S. High Discharge Efficiency of (Sr,Pb,Bi)TiO_3 Relaxor Ceramics for Energy-Storage Application. *Appl. Phys. Lett.* **2018**, *112*, 203903.

(109) Qi, X.; Zhao, Y.; Sun, E.; Du, J.; Li, K.; Sun, Y.; Yang, B.; Zhang, R.; Cao, W. Large Electrostrictive Effect and High Energy Storage Performance of Pr^{3+}-Doped Pin-PMN-Pt Multifunctional Ceramics in the Ergodic Relaxor Phase. *J. Eur. Ceram. Soc.* **2019**, *39*, 4060−4069.

(110) Shkuratov, S. I.; Baird, J.; Antipov, V. G.; Hackenberger, W.; Luo, J.; Zhang, S.; Lynch, C. S.; Chase, J. B.; Jo, H. R.; Roberts, C. C. Complete Stress-Induced Depolarization of Relaxor Ferroelectric Crystals without Transition through a Non-Polar Phase. *Appl. Phys. Lett.* **2018**, *112*, 122903.

(111) Li, Y.; Sun, N.; Li, X.; Du, J.; Chen, L.; Gao, H.; Hao, X.; Cao, M. Multiple Electrical Response and Enhanced Energy Storage Induced by Unusual Coexistent-Phase Structure in Relaxor Ferroelectric Ceramics. *Acta Mater.* **2018**, *146*, 202−210.

(112) Jo, H. R.; Lynch, C. S. A High Energy Density Relaxor Antiferroelectric Pulsed Capacitor Dielectric. *J. Appl. Phys.* **2016**, *119*, 024104.

(113) Gao, J.; Liu, Y.; Wang, Y.; Wang, D.; Zhong, L.; Ren, X. High Temperature-Stability of $(Pb_{0.9}$ $La_{0.1})(Zr_{0.65}$ $Ti_{0.35})O_3$ Ceramic for Energy-Storage Applications at Finite Electric Field Strength. *Scr. Mater.* **2017**, *137*, 114−118.

(114) Li, B.; Liu, Q.; Tang, X.; Zhang, T.; Jiang, Y.; Li, W.; Luo, J. High Energy Storage Density and Impedance Response of PLZT2/95/5 Antiferroelectric Ceramics. *Materials* **2017**, *10*, 143.

(115) Qiao, P.; Zhang, Y.; Chen, X.; Zhou, M.; Yan, S.; Dong, X.; Wang, G. Enhanced Energy Storage Properties and Stability in $(Pb_{0.895}$ $La_{0.07})(Zr_x$ $Ti_{1-X})O_3$ Antiferroelectric Ceramics. *Ceram. Int.* **2019**, *45*, 15898−15905.

(116) Chen, S.; Wang, X.; Yang, T.; Wang, J. Composition-Dependent Dielectric Properties and Energy Storage Performance of (Pb,La)(Zr,Sn,Ti)O_3 Antiferroelectric Ceramics. *J. Electroceram.* **2014**, *32*, 307−310.

(117) Zhuo, F.; Qiang, L.; Li, Y.; Gao, J.; Yan, Q.; Zhang, Y.; Chu, X.; Cao, W. Effect of a-Site La^{3+} Modified on Dielectric and Energy Storage Properties in Lead Zironate Stannate Titanate Ceramics. *Mater. Res. Express* **2014**, *1*, 045501.

(118) Wang, X.; Shen, J.; Yang, T.; Dong, Y.; Liu, Y. High Energy-Storage Performance and Dielectric Properties of Antiferroelectric $(Pb_{0.97}$ $La_{0.02})$ $(Zr_{0.5}$ $Sn_{0.5-X}$ $Ti_x)O_3$ Ceramic. *J. Alloys Compd.* **2016**, *655*, 309−313.

(119) Xu, R.; Xu, Z.; Feng, Y.; Wei, X.; Tian, J.; Huang, D. Evaluation of Discharge Energy Density of Antiferroelectric Ceramics for Pulse Capacitors. *Appl. Phys. Lett.* **2016**, *109*, 032903.

(120) Liu, Z.; Dong, X.; Liu, Y.; Cao, F.; Wang, G. Electric Field Tunable Thermal Stability of Energy Storage Properties of PLZST Antiferroelectric Ceramics. *J. Am. Ceram. Soc.* **2017**, *100*, 1−5.

(121) Shen, J.; Wang, X.; Yang, T.; Wang, H.; Wei, J. High Discharge Energy Density and Fast Release Speed of (Pb, La)(Zr, Sn, Ti)O_3 Antiferroelectric Ceramics for Pulsed Capacitors. *J. Alloys Compd.* **2017**, *721*, 191−198.

(122) xu, R.; Tian, J.; Zhu, Q.; Zhao, T.; Feng, Y.; Wei, X.; Xu, Z. Effects of La-Induced Phase Transition on Energy Storage and Discharge Properties of PLZST Ferroelectric/Antiferroelectric Ceramics. *Ceram. Int.* **2017**, *43*, 13918−13923.

(123) Zhang, Q.; Dan, Y.; Chen, J.; Lu, Y.; Yang, T.; Yao, X.; He, Y. Effects of Composition and Temperature on Energy Storage Properties of (Pb,La)(Zr,Sn,Ti)O_3 Antiferroelectric Ceramics. *Ceram. Int.* **2017**, *43*, 11428−11432.

(124) Dan, Y.; Xu, H.; Zou, K.; Zhang, Q.; Lu, Y.; Chang, G.; Huang, H.; He, Y. Energy Storage Characteristics of (Pb,La)(Zr,Sn,Ti)O_3 Antiferroelectric Ceramics with High Sn Content. *Appl. Phys. Lett.* **2018**, *113*, 063902.

(125) Dan, Y.; Xu, H.; Zhang, Y.; Zou, K.; Zhang, Q.; Lu, Y.; Chang, G.; Zhang, Q.; He, Y. High-Energy Density of $Pb_{0.97}La_{0.02}(Zr_{0.50}Sn_{0.45}Ti_{0.05})O_3$ Antiferroelectric Ceramics Prepared by Sol-Gel Method with Low-Cost Dibutyltin Oxide. *J. Am. Ceram. Soc.* **2019**, *102*, 1776−1783.

(126) Dan, Y.; Zou, K.; Chen, G.; Yu, Y.; Zhang, Y.; Zhang, Q.; Lu, Y.; Zhang, Q.; He, Y. Superior Energy-Storage Properties in (Pb,La)-(Zr,Sn,Ti)O_3 Antiferroelectric Ceramics with Appropriate La Content. *Ceram. Int.* **2019**, *45*, 11375−11381.

(127) Yu, Y.; Zhang, Y.; Zou, K.; Chen, G.; Zhang, Y.; Li, H.; Lu, Y.; Zhang, Q.; He, Y. High Energy Density and Efficiency in (Pb,La)-(Zr,Sn,Ti)O_3 Antiferroelectric Ceramics with High La^{3+} Content and Optimized Sn^{4+} Content. *Ceram. Int.* **2019**, *45*, 24419−24424.

(128) Zhao, Q.; Lei, H.; He, G.; Di, J.; Wang, D.; Tan, P.; Jin, H.; Cao, M. Effects of Thickness on Energy Storage of (Pb, La)(Zr, Sn, Ti) O3 Antiferroelectric Films Deposited on Lanio3 Electrodes. *Ceram. Int.* **2016**, *42*, 1314−1317.

(129) Zhao, Q.; Lei, H.; He, G.; Di, J.; Wang, D.; Tan, P.; Jin, H.; Cao, M. Effects of Thickness on Energy Storage of (Pb,La)(Zr,Sn,Ti)O_3 Antiferroelectric Films Deposited on $Lanio_3$ Electrodes. *Ceram. Int.* **2016**, *42*, 1314−1317.

(130) Liu, X.; Li, Y.; Hao, X. Ultra-High Energy-Storage Density and Fast Discharge Speed of $(Pb_{0.98-X}$ $La_{0.02}$ $Sr_x)(Zr_{0.9}$ $Sn_{0.1})_{0.995}O_3$ Antiferroelectric Ceramics Prepared Via the Tape-Casting Method. *J. Mater. Chem. A* **2019**, *7*, 11858−11866.

(131) Wang, H.; Liu, Y.; Yang, T.; Zhang, S. Ultrahigh Energy-Storage Density in Antiferroelectric Ceramics with Field-Induced Multiphase Transitions. *Adv. Funct. Mater.* **2019**, *29*, 1807321.

(132) Yang, X.; Zhuo, F.; Wang, C.; Liu, Y.; Wang, Z.; Tailor, H.; He, C.; Long, X. High Energy Storage Density and Ultrafast Discharge in Lead Lutetium Niobate Based Ceramics. *J. Mater. Chem. A* **2019**, *7*, 8414−8422.

(133) Wei, J.; Yang, T.; Wang, H. Excellent Energy Storage and Charge-Discharge Performances in $PbHfO_3$ Antiferroelectric Ceramics. *J. Eur. Ceram. Soc.* **2019**, *39*, 624−630.

(134) Gao, P.; Liu, Z.; Zhang, N.; Wu, H.; Bokov, A. A.; Ren, W.; Ye, Z.-G. New Antiferroelectric Perovskite System with Ultrahigh Energy-Storage Performance at Low Electric Field. *Chem. Mater.* **2019**, *31*, 979−990.

(135) Bao, Y.; Zhou, M.; Yan, S.; Cao, F.; Dong, X.; Wang, G. Novel Complex B-Site Lead Oxide Antiferroelectric System Developed by Compositional Design for Dielectric Energy Storage. *J. Eur. Ceram. Soc.* **2019**, *39*, 4785−4793.

(136) Xu, L.; He, C.; Yang, X.; Wang, Z.; Li, X.; Tailor, H. N.; Long, X. Composition Dependent Structure, Dielectric and Energy Storage Properties of $Pb(Tm_{1/2}Nb_{1/2})O_3$-$Pb(Mg_{1/3}Nb_{2/3})O_3$ Antiferroelectric Ceramics. *J. Eur. Ceram. Soc.* **2017**, *37*, 3329−3334.

(137) Yang, X.; Liu, Y.; He, C.; Tailor, H.; Long, X. La-Modified $Pb(Lu_{1/2}Nb_{1/2})O_3$ Antiferroelectric Ceramics with High Energy Storage Density. *J. Eur. Ceram. Soc.* **2015**, *35*, 4173−4180.

(138) Chao, W.; Yang, T.; Li, Y. Achieving High Energy Efficiency and Energy Density in $PbHfO_3$-Based Antiferroelectric Ceramics. *J. Mater. Chem. C* **2020**, *8*, 17016−17024.

(139) Hao, X.; Zhai, J.; Kong, L. B.; Xu, Z. A Comprehensive Review on the Progress of Lead Zirconate-Based Antiferroelectric Materials. *Prog. Mater. Sci.* **2014**, *63*, 1−57.

(140) Haertling, G. H.; Land, C. E. Hot-Pressed (Pb,La)(Zr,Ti)O_3 Ferroelectric Ceramics for Electrooptic Applications. *J. Am. Ceram. Soc.* **1971**, *54*, 1−11.

(141) Li, B.; Liu, Q.-X.; Tang, X.-G.; Zhang, T.-F.; Jiang, Y.-P.; Li, W.-H.; Luo, J. Antiferroelectric to Relaxor Ferroelectric Phase Transition in PbO Modified $(Pb_{0.97}$ $La_{0.02})(Zr_{0.95}$ $Ti_{0.05})O_3$ Ceramics with a Large Energy-Density for Dielectric Energy Storage. *RSC Adv.* **2017**, *7*, 43327−43333.

(142) Niu, Z.-H.; Jiang, Y.-P.; Tang, X.-G.; Liu, Q.-X.; Li, W.-H. B-Site Non-Stoichiometric $(Pb_{0.97}$ $La_{0.02})(Zr_{0.95}$ $Ti_{0.05})O_3$ Antiferroelectric Ceramics for Energy Storage. *Journal of Asian Ceramic Societies* **2018**, *6*, 240−246.

(143) Samanta, S.; Sankaranarayanan, V.; Sethupathi, K. Effect of Nb and Fe Co-Doping on Microstructure, Dielectric Response, Ferroelectricity and Energy Storage Density of PLZT. *J. Mater. Sci.: Mater. Electron.* **2018**, *29*, 20383−20394.

(144) Kumar, A.; Yoon, J.; Thakre, A.; Peddigari, M.; Jeong, D.-Y.; Kong, Y.-M.; Ryu, J. Dielectric, Ferroelectric, Energy Storage, and Pyroelectric Properties of Mn-Doped $(Pb_{0.93}\ La_{0.07})(Zr_{0.82}\ Ti_{0.18})O_3$ Anti-Ferroelectric Ceramics. *Han'guk Seramik Hakhoechi* **2019**, *56*, 412−420.

(145) Qiao, P.; Zhang, Y.; Chen, X.; Zhou, M.; Wang, G.; Dong, X. Effect of Mn-Doping on Dielectric and Energy Storage Properties of $(Pb_{0.91}\ La_{0.06})(Zr_{0.96}Ti_{0.04})O_3$ Antiferroelectric Ceramics. *J. Alloys Compd.* **2019**, *780*, 581−587.

(146) Ciuchi, I. V.; Mitoseriu, L.; Galassi, C. Antiferroelectric to Ferroelectric Crossover and Energy Storage Properties of $(Pb_{1\text{-}X}La_x)(Zr_{0.90}\ Ti_{0.10})_{1\text{-}X/4}O_3$ $(0.02 \leq X \leq 0.04)$ Ceramics. *J. Am. Ceram. Soc.* **2016**, *99*, 2382−2387.

(147) Kumar, A.; Kim, S.; Peddigari, M.; Jeong, D.-H.; Hwang, G.; Ryu, J. High Energy Storage Properties and Electrical Field Stability of Energy Efficiency of $(Pb_{0.89}\ La_{0.11})(Zr_{0.70}\ Ti_{0.30})_{0.9725}O_3$ Relaxor Ferroelectric Ceramics. *Electron. Mater. Lett.* **2019**, *15*, 323−330.

(148) Jiang, S.; Zhang, L.; Zhang, G.; Liu, S.; Yi, J.; Xiong, X.; Yu, Y.; He, J.; Zeng, Y. Effect of Zr:Sn Ratio in the Lead Lanthanum Zirconate Stannate Titanate Anti-Ferroelectric Ceramics on Energy Storage Properties. *Ceram. Int.* **2013**, *39*, 5571−5575.

(149) Zhang, L.; Jiang, S.; Zeng, Y.; Fu, M.; Han, K.; Li, Q.; Wang, Q.; Zhang, G. Y Doping and Grain Size Co-Effects on the Electrical Energy Storage Performance of $(Pb_{0.87}\ Ba_{0.1}\ La_{0.02})\ (Zr_{0.65}\ Sn_{0.3}\ Ti_{0.05})O_3$ Anti-Ferroelectric Ceramics. *Ceram. Int.* **2014**, *40*, 5455−5460.

(150) Wang, X.; Shen, J.; Yang, T.; Xiao, Z.; Dong, Y. Phase Transition and Energy Storage Performance in Ba-Doped PLZST Antiferroelectric Ceramics. *J. Mater. Sci.: Mater. Electron.* **2015**, *26*, 9200−9204.

(151) Zhang, G.; Zhu, D.; Zhang, X.; Zhang, L.; Yi, J.; Xie, B.; Zeng, Y.; Li, Q.; Wang, Q.; Jiang, S. High-Energy Storage Performance of $(Pb_{0.87}\ Ba_{0.1}\ La_{0.02})(Zr_{0.68}\ Sn_{0.24}\ Ti_{0.08})O_3$ Antiferroelectric Ceramics Fabricated by the Hot-Press Sintering Method. *J. Am. Ceram. Soc.* **2015**, *98*, 1175−1181.

(152) Zhang, L.; Jiang, S.; Fan, B.; Zhang, G. High Energy Storage Performance in $(Pb_{0.858}\ Ba_{0.1}\ La_{0.02}Y_{0.008})(Zr_{0.65}\ Sn_{0.3}\ Ti_{0.05})O_3\text{-}(Pb_{0.97}\ La_{0.02})(Zr_{0.9}\ Sn_{0.05}\ Ti_{0.05})O_3$ Anti-Ferroelectric Composite Ceramics. *Ceram. Int.* **2015**, *41*, 1139−1144.

(153) Zhang, Q.; Liu, X.; Zhang, Y.; Song, X.; Zhu, J.; Baturin, I.; Chen, J. Effect of Barium Content on Dielectric and Energy Storage Properties of $(Pb,La,Ba)(Zr,Sn,Ti)O_3$ Ceramics. *Ceram. Int.* **2015**, *41*, 3030−3035.

(154) Xu, R.; Xu, Z.; Feng, Y.; Tian, J.; Huang, D. Energy Storage and Release Properties of Sr-Doped $(Pb,La)(Zr,Sn,Ti)O_3$ Antiferroelectric Ceramics. *Ceram. Int.* **2016**, *42*, 12875−12879.

(155) Zhang, Q.; Chen, J.; Lu, Y.; Yang, T. Q.; Yao, X.; He, Y. $(Pb,Sm)(Zr,Sn,Ti)O_3$ Multifunctional Ceramics with Large Electric-Field-Induced Strain and High-Energy Storage Density. *J. Am. Ceram. Soc.* **2016**, *99*, 3853−3856.

(156) Zhang, Q.; Tong, H.; Chen, J.; Lu, Y.; Yang, T.; Yao, X.; He, Y. High Recoverable Energy Density over a Wide Temperature Range in Sr Modified $(Pb,La)(Zr,Sn,Ti)O_3$ Antiferroelectric Ceramics with an Orthorhombic Phase. *Appl. Phys. Lett.* **2016**, *109*, 262901.

(157) Guo, B.; Liu, P.; Song, Y.; Liu, D. Effect of Ti Content on Energy Storage Properties of $(Pb_{0.87}\ Ba_{0.10}\ La_{0.02})(Zr_{0.60}\ Sn_{0.40\text{-}X}\ Ti_x)O_3$ Bulk Ceramics. *Ferroelectrics* **2017**, *510*, 152−160.

(158) Liu, Z.; Bai, Y.; Chen, X.; Dong, X.; Nie, H.; Cao, F.; Wang, G. Linear Composition-Dependent Phase Transition Behavior and Energy Storage Performance of Tetragonal PLZST Antiferroelectric Ceramics. *J. Alloys Compd.* **2017**, *691*, 721−725.

(159) Zhang, G.; Liu, P.; Fan, B.; Liu, H.; Zeng, Y.; Qiu, S.; Jiang, S.; Li, Q.; Wang, Q.; Liu, J. Large Energy Density in Ba Doped $Pb_{0.97}La_{0.02}(Zr_{0.65}Sn_{0.3}Ti_{0.05})O_3$ Antiferroelectric Ceramics with Improved Temperature Stability. *IEEE Trans. Dielectr. Electr. Insul.* **2017**, *24*, 744−748.

(160) Liu, P.; Li, M.-Y.; Zhang, Q.; Li, W.; Zhang, Y.; Shen, M.; Qiu, S.; Zhang, G.; Jiang, S. High Thermal Stability in PLZST Anti-Ferroelectric Energy Storage Ceramics with the Coexistence of Tetragonal and Orthorhombic Phase. *J. Eur. Ceram. Soc.* **2018**, *38*, 5396−5401.

(161) Liu, P.; Zhang, Y.; Zhu, Y.; Fan, B.; Li, W.; Zhang, H.; Jiang, S. Structure Variation and Energy Storage Properties of Acceptor-Modified Pblzst Antiferroelectric Ceramics. *J. Am. Ceram. Soc.* **2018**, *102*, 1912−1920.

(162) Mohapatra, P.; Fan, Z.; Cui, J.; Tan, X. Relaxor Antiferroelectric Ceramics with Ultrahigh Efficiency for Energy Storage Applications. *J. Eur. Ceram. Soc.* **2019**, *39*, 4735−4742.

(163) Wei, M.; Tang, Z.; Wang, W.; Yu, H.; Chen, H.; Zhang, J.; Zhang, W. Enhanced Energy Storage Properties of (1-X)PLZST-$Xbiyo_3$ Ceramics. *J. Electron. Mater.* **2019**, *48*, 2162−2167.

(164) Yu, H.; Zhang, J.; Wei, M.; Huang, J.; Chen, H.; Yang, C. Enhanced Energy Storage Density Performance in $(Pb_{0.97}\ La_{0.02})(Zr_{0.5}\ Sn_{0.44}\ Ti_{0.06})\text{-}BiYO_3$ Anti-Ferroelectric Composite Ceramics. *J. Mater. Sci.: Mater. Electron* **2016**, *28*, 832−838.

(165) Xu, R.; Zhu, Q.; Tian, J.; Feng, Y.; Xu, Z. Effect of Ba-Dopant on Dielectric and Energy Storage Properties of PLZST Antiferroelectric Ceramics. *Ceram. Int.* **2017**, *43*, 2481−2485.

(166) Chen, S.; Yang, T.; Wang, J.; Yao, X. Effects of Glass Additions on the Dielectric Properties and Energy Storage Performance of $Pb_{0.97}La_{0.02}(Zr_{0.56}Sn_{0.35}Ti_{0.09})O_3$ Antiferroelectric Ceramics. *J. Mater. Sci.: Mater. Electron* **2013**, *24*, 4764−4768.

(167) Pan, W.; Zhang, Q.; Bhalla, A.; Cross, L. E. Field-Forced Antiferroelectric-to-Ferroelectric Switching in Modified Lead Zirconate Titanate Stannate Ceramics. *J. Am. Ceram. Soc.* **1989**, *72*, 571−578.

(168) Reaney, I. M.; Glazounov, A.; Chu, F.; Bell, A.; Setter, N. Tem of Antiferroelectric-Ferroelectric Phase Boundary in $(Pb_{1\text{-}X}\ Ba_x)(Zr_{1\text{-}X}\ Ti_x)O_3$ Solid Solution. *Br. Ceram. Trans.* **1997**, *96*, 217−224.

(169) MacLaren, I.; Villaurrutia, R.; Peláiz-Barranco, A. Domain Structures and Nanostructures in Incommensurate Antiferroelectric $Pb_x\ La_{1\text{-}X}(Zr_{0.9}\ Ti_{0.1})O_3$. *J. Appl. Phys.* **2010**, *108*, 034109.

(170) Villaurrutia, R.; MacLaren, I.; Peláiz-Barranco, A. Study of Incommensurate Phases in Lanthanum-Doped Zirconium-Rich Lead Zirconate Titanate Ceramics. *Journal of Physics: Conference Series* **2010**, *241*, 012038.

(171) Bersuker, I. B. Pseudo Jahn-Teller Origin of Perovskite Multiferroics, Magnetic-Ferroelectric Crossover, and Magnetoelectric Effects: The D^0-D^{10} Problem. *Phys. Rev. Lett.* **2012**, *108*, 137202.

(172) Fu, Z.; Chen, X.; Li, Z.; Hu, T.; Zhang, L.; Lu, P.; Zhang, S.; Wang, G.; Dong, X.; Xu, F. Unveiling the Ferrielectric Nature of $PbZrO_3$-Based Antiferroelectric Materials. *Nat. Commun.* **2020**, *11*, 3809.

(173) Zhang, L.; Jiang, S.; Fan, B.; Zhang, G. Enhanced Energy Storage Performance in $(Pb_{0.858}\ Ba_{0.1}\ La_{0.02}Y_{0.008})(Zr_{0.65}\ Sn_{0.3}\ Ti_{0.05})O_3\text{-}(Pb_{0.97}\ La_{0.02})(Zr_{0.9}\ Sn_{0.05}\ Ti_{0.05})O_3$ Anti-Ferroelectric Composite Ceramics by Spark Plasma Sintering. *J. Alloys Compd.* **2015**, *622*, 162−165.

(174) Ibn-Mohammed, T.; Koh, S. C. L.; Reaney, I. M.; Sinclair, D. C.; Mustapha, K. B.; Acquaye, A.; Wang, D. Are Lead-Free Piezoelectrics More Environmentally Friendly? *MRS Commun.* **2017**, *7*, 1−7.

(175) Ibn-Mohammed, T.; Koh, S. C. L.; Reaney, I. M.; Acquaye, A.; Wang, D.; Taylor, S.; Genovese, A. Integrated Hybrid Life Cycle Assessment and Supply Chain Environmental Profile Evaluations of Lead-Based (Lead Zirconate Titanate) Versus Lead-Free (Potassium Sodium Niobate) Piezoelectric Ceramics. *Energy Environ. Sci.* **2016**, *9*, 3495−3520.

(176) Wang, D.; Wang, G.; Murakami, S.; Fan, Z.; Feteira, A.; Zhou, D.; Sun, S.; Zhao, Q.; Reaney, I. M. $BiFeO_3$-$BaTiO_3$: A New Generation of Lead-Free Electroceramics. *J. Adv. Dielectr.* **2018**, *08*, 1830004.

(177) Peddigari, M.; Palneedi, H.; Hwang, G.-T.; Ryu, J. Linear and Nonlinear Dielectric Ceramics for High-Power Energy Storage Capacitor Applications. *Han'guk Seramik Hakhoechi* **2019**, *56*, 1−23.

(178) Sun, Z.; Wang, Z.; Tian, Y.; Wang, G.; Wang, W.; Yang, M.; Wang, X.; Zhang, F.; Pu, Y. Progress, Outlook, and Challenges in Lead-

Free Energy-Storage Ferroelectrics. *Adv. Electron. Mater.* **2020**, *6*, 1900698.

(179) Hao, X. A Review on the Dielectric Materials for High Energy-Storage Application. *J. Adv. Dielectr.* **2013**, *03*, 1330001.

(180) Du, H.-L.; Yang, Z.-T.; Gao, F.; Jin, L.; Cheng, H.-L.; Qu, S.-B. Lead-Free Nonlinear Dielectric Ceramics for Energy Storage Applications: Current Status and Challenges. *Journal of Inorganic Materials* **2018**, *33*, 1046−1058.

(181) Han, D.; Wang, C.; Lu, D.; Hussain, F.; Wang, D.; Meng, F. A Temperature Stable $(Ba_{1-X}\ Ce_x)(Ti_{1-X/2}\ Mg_{x/2})O_3$ Lead-Free Ceramic for X4D Capacitors. *J. Alloys Compd.* **2020**, *821*, 153480.

(182) Yang, H.; Yan, F.; Zhang, G.; Lin, Y.; Wang, F. Dielectric Behavior and Impedance Spectroscopy of Lead-Free $Ba_{0.85}Ca_{0.15}Zr_{0.1}Ti_{0.9}O_3$ Ceramics with B_2O_3-Al_2O_3-SiO_2 Glass-Ceramics Addition for Enhanced Energy Storage. *J. Alloys Compd.* **2017**, *720*, 116−125.

(183) Ren, P.; Wang, Q.; Li, S.; Zhao, G. Energy Storage Density and Tunable Dielectric Properties of $BaTi_{0.85}Sn_{0.15}O_3$/MgO Composite Ceramics Prepared by Sps. *J. Eur. Ceram. Soc.* **2017**, *37*, 1501−1507.

(184) Ma, R.; Cui, B.; Shangguan, M.; Wang, S.; Wang, Y.; Chang, Z.; Wang, Y. A Novel Double-Coating Approach to Prepare Fine-Grained $BaTiO_3$@La_2O_3@SiO_2 Dielectric Ceramics for Energy Storage Application. *J. Alloys Compd.* **2017**, *690*, 438−445.

(185) Liu, B.; Wu, Y.; Huang, Y. H.; Song, K. X.; Wu, Y. J. Enhanced Dielectric Strength and Energy Storage Density in $BaTi_{0.7}Zr_{0.3}O_3$ Ceramics Via Spark Plasma Sintering. *J. Mater. Sci.* **2019**, *54*, 4511−4517.

(186) Wang, T.; Wei, X.; Hu, Q.; Jin, L.; Xu, Z.; Feng, Y. Effects of $Znnb_2o_6$ Addition on $BaTiO_3$ Ceramics for Energy Storage. *Mater. Sci. Eng., B* **2013**, *178*, 1081−1086.

(187) Zeng, M.; Liu, J.; Yu, H.; Chao, M.; Tang, B.; Zhang, S. $NiNb_2O_6$-$BaTiO_3$ Ceramics for Energy-Storage Capacitors. *Energy Technology* **2018**, *6*, 899−905.

(188) Hu, Q.; Jin, L.; Wang, T.; Li, C.; Xing, Z.; Wei, X. Dielectric and Temperature Stable Energy Storage Properties of 0.88batio$_3$-0.12bi-$(Mg_{1/2}\ ti_{1/2})O_3$ Bulk Ceramics. *J. Alloys Compd.* **2015**, *640*, 416−420.

(189) Zhang, Q.; Li, Z. Weakly Coupled Relaxor Behavior of $BaTiO_3$-$Bi(Mg_{1/2}\ Ti_{1/2})O_3$ Lead-Free Ceramics. *J. Adv. Dielectr.* **2013**, *03*, 1320001.

(190) Shen, Z.; Wang, X.; Luo, B.; Li, L. $BaTiO_3$-$BiYbO_3$ Perovskite Materials for Energy Storage Applications. *J. Mater. Chem. A* **2015**, *3*, 18146−18153.

(191) Li, W.-B.; Zhou, D.; Pang, L.-X. Enhanced Energy Storage Density by Inducing Defect Dipoles in Lead Free Relaxor Ferroelectric $BaTiO_3$-Based Ceramics. *Appl. Phys. Lett.* **2017**, *110*, 132902.

(192) Wang, T.; Jin, L.; Li, C.; Hu, Q.; Wei, X. Relaxor Ferroelectric $BaTiO_3$-$Bi(Mg_{2/3}Nb_{1/3})O_3$ Ceramics for Energy Storage Application. *J. Am. Ceram. Soc.* **2015**, *98*, 559−566.

(193) Liu, G.; Li, Y.; Shi, M.; Yu, L.; Chen, P.; Yu, K.; Yan, Y.; Jin, L.; Wang, D.; Gao, J. An Investigation of the Dielectric Energy Storage Performance of $Bi(Mg_{2/3}Nb_{1/3})O_3$-Modifed $BaTiO_3$ Pb-Free Bulk Ceramics with Improved Temperature/Frequency Stability. *Ceram. Int.* **2019**, *45*, 19189−19196.

(194) Yang, H.; Yan, F.; Lin, Y.; Wang, T.; Wang, F.; Wang, Y.; Guo, L.; Tai, W.; Wei, H. Lead-Free $BaTiO_3$-$Bi_{0.5}Na_{0.5}TiO_3$-$Na_{0.73}Bi_{0.09}NbO_3$ Relaxor Ferroelectric Ceramics for High Energy Storage. *J. Eur. Ceram. Soc.* **2017**, *37*, 3303−3311.

(195) Li, W.-B.; Zhou, D.; He, B.; Li, F.; Pang, L.-X.; Lu, S.-G. Structure and Dielectric Properties of $Nd(Zn_{1/2}Ti_{1/2})O_3$-$BaTiO_3$ Ceramics for Energy Storage Applications. *J. Alloys Compd.* **2016**, *685*, 418−422.

(196) Wu, L.; Wang, X.; Li, L. Lead-Free $BaTiO_3$-$Bi(Zn_{2/3}Nb_{1/3})O_3$ Weakly Coupled Relaxor Ferroelectric Materials for Energy Storage. *RSC Adv.* **2016**, *6*, 14273−14282.

(197) Li, W.-B.; Zhou, D.; Pang, L.-X.; Xu, R.; Guo, H.-H. Novel Barium Titanate Based Capacitors with High Energy Density and Fast Discharge Performance. *J. Mater. Chem. A* **2017**, *5*, 19607−19612.

(198) Li, W.-B.; Zhou, D.; Xu, R.; Wang, D.-W.; Su, J.-Z.; Pang, L.-X.; Liu, W.-F.; Chen, G.-H. $BaTiO_3$-Based Multilayers with Outstanding Energy Storage Performance for High Temperature Capacitor Applications. *ACS Appl. Energy Mater.* **2019**, *2*, 5499−5506.

(199) Yuan, Q.; Yao, F.; Wang, Y.; Ma, R.; Wang, H. Relaxor Ferroelectric 0.9$BaTiO_3$-0.1$Bi(Zn_{0.5}\ Zr_{0.5})O_3$ Ceramic Capacitors with High Energy Density and Temperature Stable Energy Storage Properties. *J. Mater. Chem. C* **2017**, *5*, 9552−9558.

(200) Zhao, X.; Zhou, Z.; Liang, R.; Liu, F.; Dong, X. High-Energy Storage Performance in Lead-Free (1-X)$BaTiO_3$-X$Bi(Zn_{0.5}\ Ti_{0.5})O_3$ Relaxor Ceramics for Temperature Stability Applications. *Ceram. Int.* **2017**, *43*, 9060−9066.

(201) Dong, X.; Chen, H.; Wei, M.; Wu, K.; Zhang, J. Structure, Dielectric and Energy Storage Properties of $BaTiO_3$ Ceramics Doped with $Ynbo_4$. *J. Alloys Compd.* **2018**, *744*, 721−727.

(202) Li, F.; Zhou, M.; Zhai, J.; Shen, B.; Zeng, H. Novel Barium Titanate Based Ferroelectric Relaxor Ceramics with Superior Charge-Discharge Performance. *J. Eur. Ceram. Soc.* **2018**, *38*, 4646−4652.

(203) Li, W.-B.; Zhou, D.; Xu, R.; Pang, L.-X.; Reaney, I. M. $BaTiO_3$-$Bi(Li_{0.5}\ Ta_{0.5})O_3$, Lead-Free Ceramics, and Multilayers with High Energy Storage Density and Efficiency. *ACS Appl. Energy Mater.* **2018**, *1*, 5016−5023.

(204) Yuan, Q.; Li, G.; Yao, F.-Z.; Cheng, S.-D.; Wang, Y.; Ma, R.; Mi, S.-B.; Gu, M.; Wang, K.; Li, J.-F.; et al. Simultaneously Achieved Temperature-Insensitive High Energy Density and Efficiency in Domain Engineered $BaTiO_3$-$Bi(Mg_{0.5}\ Zr_{0.5})O_3$ Lead-Free Relaxor Ferroelectrics. *Nano Energy* **2018**, *52*, 203−210.

(205) Zhou, M.; Liang, R.; Zhou, Z.; Dong, X. Novel $BaTiO_3$-Based Lead-Free Ceramic Capacitors Featuring High Energy Storage Density, High Power Density, and Excellent Stability. *J. Mater. Chem. C* **2018**, *6*, 8528−8537.

(206) Wan, J.; Pu, Y.; Hui, C.; Cui, C.; Guo, Y. Effect of $KNbO_3$ on Microstructure and Electrical Properties of Lead-Free 0.92$BaTiO_3$-0.08$K_{0.5}Bi_{0.5}TiO_3$ Ceramic. *J. Mater. Sci.: Mater. Electron* **2018**, *29*, 6556−6563.

(207) Wan, J.; Pu, Y.; Hui, C.; Cui, C.; Guo, Y. Synthesis and Characterizations of $NaNbO_3$ Modified 0.92$BaTiO_3$-0.08$K_{0.5}Bi_{0.5}TiO_3$ Ceramics for Energy Storage Applications. *J. Mater. Sci.: Mater. Electron* **2018**, *29*, 5158−5162.

(208) Hu, Q.; Tian, Y.; Zhu, Q.; Bian, J.; Jin, L.; Du, H.; Alikin, D. O.; Shur, V. Y.; Feng, Y.; Xu, Z.; et al. Achieve Ultrahigh Energy Storage Performance in $BaTiO_3$-$Bi(Mg_{1/2}\ Ti_{1/2})O_3$ Relaxor Ferroelectric Ceramics Via Nano-Scale Polarization Mismatch and Reconstruction. *Nano Energy* **2020**, *67*, 104264.

(209) Yang, H.; Lu, Z.; Li, L.; Bao, W.; Ji, H.; Li, J.; Feteira, A.; Xu, F.; Zhang, Y.; Sun, H.; et al. Novel $BaTiO_3$-Based, Ag/Pd-Compatible Lead-Free Relaxors with Superior Energy Storage Performance. *ACS Appl. Mater. Interfaces* **2020**, *12*, 43942−43949.

(210) Zhang, L.; Pang, L.-X.; Li, W.-B.; Zhou, D. Extreme High Energy Storage Efficiency in Perovskite Structured $(1-X)(Ba_{0.8}\ sr_{0.2})TiO_3$-$Xbi(Zn_{2/3}Nb_{1/3})O_3$ $(0.04 \le X \le 0.16)$ Ceramics. *J. Eur. Ceram. Soc.* **2020**, *40*, 3343−3347.

(211) Dai, Z.; Xie, J.; Liu, W.; Wang, X.; Zhang, L.; Zhou, Z.; Li, J.; Ren, X. Effective Strategy to Achieve Excellent Energy Storage Properties in Lead-Free $BaTiO_3$-Based Bulk Ceramics. *ACS Appl. Mater. Interfaces* **2020**, *12*, 30289−30296.

(212) Liu, G.; Li, Y.; Guo, B.; Tang, M.; Li, Q.; Dong, J.; Yu, L.; Yu, K.; Yan, Y.; Wang, D.; et al. Ultrahigh Dielectric Breakdown Strength and Excellent Energy Storage Performance in Lead-Free Barium Titanate-Based Relaxor Ferroelectric Ceramics Via a Combined Strategy of Composition Modification, Viscous Polymer Processing, and Liquid-Phase Sintering. *Chem. Eng. J.* **2020**, *398*, 125625.

(213) Wu, T.; Pu, Y.; Gao, P.; Liu, D. Influence of Sr/Ba Ratio on the Energy Storage Properties and Dielectric Relaxation Behaviors of Strontium Barium Titanate Ceramics. *J. Mater. Sci.: Mater. Electron.* **2013**, *24*, 4105−4112.

(214) Jin, Q.; Pu, Y.-P.; Wang, C.; Gao, Z.-Y.; Zheng, H.-Y. Enhanced Energy Storage Performance of $Ba_{0.4}Sr_{0.6}TiO_3$ Ceramics: Influence of Sintering Atmosphere. *Ceram. Int.* **2017**, *43*, S232−S238.

(215) Song, Z.; Liu, H.; Zhang, S.; Wang, Z.; Shi, Y.; Hao, H.; Cao, M.; Yao, Z.; Yu, Z. Effect of Grain Size on the Energy Storage Properties of

$(Ba_{0.4}Sr_{0.6})TiO_3$ Paraelectric Ceramics. *J. Eur. Ceram. Soc.* **2014**, *34*, 1209−1217.

(216) Song, Z.; Liu, H.; Hao, H.; Zhang, S.; Zhang, S.; Cao, M.; Yao, Z.; Wang, Z.; Hu, W.; Shi, Y.; et al. The Effect of Grain Boundary on the Energy Storage Properties of $(Ba_{0.4}$ $Sr_{0.6M})TiO_3$ Paraelectric Ceramics by Varying Grain Sizes. *IEEE transactions on ultrasonics, ferroelectrics, and frequency control* **2015**, *62*, 609−616.

(217) Hu, Q.-G.; Shen, Z.-Y.; Li, Y.-M.; Wang, Z.-M.; Luo, W.-Q.; Xie, Z.-X. Enhanced Energy Storage Properties of Dysprosium Doped Strontium Titanate Ceramics. *Ceram. Int.* **2014**, *40*, 2529−2534.

(218) Yao, Z.; Luo, Q.; Zhang, G.; Hao, H.; Cao, M.; Liu, H. Improved Energy-Storage Performance and Breakdown Enhancement Mechanism of Mg-Doped $SrTiO_3$ Bulk Ceramics for High Energy Density Capacitor Applications. *J. Mater. Sci.: Mater. Electron.* **2017**, *28*, 11491−11499.

(219) Ang, C.; Yu, Z. High Remnant Polarization in $(Sr_{0.7}Bi_{0.2})TiO_3$-$(Na_{0.5}$ $Bi_{0.5})TiO_3$ Solid Solutions. *Appl. Phys. Lett.* **2009**, *95*, 232908.

(220) Ang, C.; Yu, Z. Dielectric and Ferroelectric Properties in $(Sr,Ni,Na)TiO_3$ Solid Solutions. *J. Appl. Phys.* **2010**, *107*, 114106.

(221) Ang, C.; Yu, Z. Phonon-Coupled Impurity Dielectric Modes in $Sr_{1-1.5x}$ Bi_xTiO_3. *Phys. Rev. B: Condens. Matter Mater. Phys.* **2000**, *61*, 11363−11366.

(222) Li, J.; Li, F.; Xu, Z.; Zhang, S. Multilayer Lead-Free Ceramic Capacitors with Ultrahigh Energy Density and Efficiency. *Adv. Mater.* **2018**, *30*, 1802155.

(223) Ye, X. Y.; Li, Y. M.; Bian, J. J. Dielectric and Energy Storage Properties of Mn-Doped $Ba_{0.3}$ $Sr_{0.475}$ $La_{0.12}$ $Ce_{0.03}$ TiO_3 Dielectric Ceramics. *J. Eur. Ceram. Soc.* **2017**, *37*, 107−114.

(224) Xie, J.; Hao, H.; Liu, H.; Yao, Z.; Song, Z.; Zhang, L.; Xu, Q.; Dai, J.; Cao, M. Dielectric Relaxation Behavior and Energy Storage Properties of Sn Modified $SrTiO_3$ Based Ceramics. *Ceram. Int.* **2016**, *42*, 12796−12801.

(225) Luo, Q.; Li, X.; Yao, Z.; Zhang, L.; Xie, J.; Hao, H.; Cao, M.; Manan, A.; Liu, H. The Role of Dielectric Permittivity in the Energy Storage Performances of Ultrahigh-Permittivity $(Sr_x$ $Ba_{1-X})$-$(Ti_{0.85}Sn_{0.15})O_3$ Ceramics. *Ceram. Int.* **2018**, *44*, 5304−5310.

(226) Zhang, Q.; Wang, L.; Luo, J.; Tang, Q.; Du, J. $Ba_{0.4}Sr_{0.6}TiO_3$/MgO Composites with Enhanced Energy Storage Density and Low Dielectric Loss for Solid-State Pulse-Forming Line. *Int. J. Appl. Ceram. Technol.* **2010**, *7*, E124−E128.

(227) Huang, Y. H.; Wu, Y. J.; Qiu, W. J.; Li, J.; Chen, X. M. Enhanced Energy Storage Density of $Ba_{0.4}Sr_{0.6}TiO_3$-MgO Composite Prepared by Spark Plasma Sintering. *J. Eur. Ceram. Soc.* **2015**, *35*, 1469−1476.

(228) Li, W.-B.; Zhou, D.; Pang, L.-X. Structure and Energy Storage Properties of Mn-Doped $(Ba,Sr)TiO_3$-MgO Composite Ceramics. *J. Mater. Sci.: Mater. Electron.* **2017**, *28*, 8749−8754.

(229) Huang, Y. H.; Wu, Y. J.; Liu, B.; Yang, T. N.; Wang, J. J.; Li, J.; Chen, L.-Q.; Chen, X. M. From Core-Shell $Ba_{0.4}Sr_{0.6}TiO_3@SiO_2$ Particles to Dense Ceramics with High Energy Storage Performance by Spark Plasma Sintering. *J. Mater. Chem. A* **2018**, *6*, 4477−4484.

(230) Chen, K.; Pu, Y.; Xu, N.; Luo, X. Effects of SrO-B_2O_3-SiO_2 Glass Additive on Densification and Energy Storage Properties of $Ba_{0.4}Sr_{0.6}TiO_3$ Ceramics. *J. Mater. Sci.: Mater. Electron* **2012**, *23*, 1599−1603.

(231) Liu, B.; Wang, X.; Zhang, R.; Li, L. Energy Storage Properties of Ultra Fine-Grained $Ba_{0.4}Sr_{0.6}TiO_3$-Based Ceramics Sintered at Low Temperature. *J. Alloys Compd.* **2017**, *691*, 619−623.

(232) Yang, H.; Yan, F.; Lin, Y.; Wang, T. Enhanced Energy Storage Properties of $Ba_{0.4}Sr_{0.6}TiO_3$ Lead-Free Ceramics with Bi_2o_3-B_2O_3-SiO_2 Glass Addition. *J. Eur. Ceram. Soc.* **2018**, *38*, 1367−1373.

(233) Shen, Z.-Y.; Yu, Y.-Y.; Wang, Y.; Zhang, L.; Luo, W.-Q.; Wang, Z.-M.; Li, Y.-M. Reduced High Temperature Dielectric Loss in Bsb Glass Modified $Ba_{0.3}Sr_{0.7}TiO_3$ Ceramics for Energy Storage. *J. Mater. Sci.: Mater. Electron* **2018**, *29*, 1093−1097.

(234) Wang, J.; Xu, C.; Shen, B.; Zhai, J. Enhancing Energy Storage Density of (Ba, Sr)TiO_3 Ceramic Particles by Coating with Al_2O_3 and SiO_2. *J. Mater. Sci.: Mater. Electron* **2013**, *24*, 3309−3314.

(235) Li, L.; Yu, X.; Cai, H.; Liao, Q.; Han, Y.; Gao, Z. Preparation and Dielectric Properties of $BaCu(B_2O_5)$-Doped $SrTiO_3$-Based Ceramics for Energy Storage. *Mater. Sci. Eng., B* **2013**, *178*, 1509−1514.

(236) Li, Z. C.; Chen, G. H.; Yuan, C. L.; Zhou, C. R.; Yang, T.; Yang, Y. Effects of $NiNb_2O_6$ Doping on Dielectric Property, Microstructure and Energy Storage Behavior of $Sr_{0.97}La_{0.02}TiO_3$ Ceramics. *J. Mater. Sci.: Mater. Electron* **2017**, *28*, 1151−1158.

(237) Cui, C.; Pu, Y.; Gao, Z.; Wan, J.; Guo, Y.; Hui, C.; Wang, Y.; Cui, Y. Structure, Dielectric and Relaxor Properties in Lead-Free ST-NBT Ceramics for High Energy Storage Applications. *J. Alloys Compd.* **2017**, *711*, 319−326.

(238) Zhang, L.; Wang, Z.; Li, Y.; Chen, P.; Cai, J.; Yan, Y.; Zhou, Y.; Wang, D.; Liu, G. Enhanced Energy Storage Performance in Sn Doped $Sr_{0.6}(Na_{0.5}$ $Bi_{0.5})_{0.4}$ TiO_3 Lead-Free Relaxor Ferroelectric Ceramics. *J. Eur. Ceram. Soc.* **2019**, *39*, 3057−3063.

(239) Wang, C.; Yan, F.; Yang, H.; Lin, Y.; Wang, T. Dielectric and Ferroelectric Properties of $SrTiO_3$-$Bi_{0.54}Na_{0.46}TiO_3$-$BaTiO_3$ Lead-Free Ceramics for High Energy Storage Applications. *J. Alloys Compd.* **2018**, *749*, 605−611.

(240) Yan, F.; Yang, H.; Lin, Y.; Wang, T. Dielectric and Ferroelectric Properties of $SrTiO_3$-$Bi_{0.5}Na_{0.5}TiO_3$-$BaAl_{0.5}Nb_{0.5}O_3$ Lead-Free Ceramics for High-Energy-Storage Applications. *Inorg. Chem.* **2017**, *56*, 13510−13516.

(241) Yang, H.; Yan, F.; Lin, Y.; Wang, T.; He, L.; Wang, F. A Lead Free Relaxation and High Energy Storage Efficiency Ceramics for Energy Storage Applications. *J. Alloys Compd.* **2017**, *710*, 436−445.

(242) Kong, X.; Yang, L.; Cheng, Z.; Zhang, S. Bi-Modified $SrTiO_3$-Based Ceramics for High-Temperature Energy Storage Applications. *J. Am. Ceram. Soc.* **2020**, *103*, 1722−1731.

(243) Cui, C.; Pu, Y.; Shi, R. High-Energy Storage Performance in Lead-Free $(0.8\text{-}X)SrTiO_3$-$0.2Na_{0.5}Bi_{0.5}TiO_3$-$xBaTiO_3$ Relaxor Ferroelectric Ceramics. *J. Alloys Compd.* **2018**, *740*, 1180−1187.

(244) Cui, C.; Pu, Y.; Li, X.; Cui, Y.; Liu, G. High Energy Storage Density of Temperature-Stable X9R Ceramics. *Mater. Res. Bull.* **2018**, *105*, 114−120.

(245) Li, Y.; Dong, G.; Liu, Q.; Wu, D. Preparation and Investigation on Properties of BST-Base Ceramic with High-Energy Storage Density. *J. Adv. Dielectr.* **2013**, *03*, 1350005.

(246) Pan, W.; Cao, M.; Jan, A.; Hao, H.; Yao, Z.; Liu, H. High Breakdown Strength and Energy Storage Performance in (Nb, Zn) Modified $SrTiO_3$ Ceramics Via Synergy Manipulation. *J. Mater. Chem. C* **2020**, *8*, 2019−2027.

(247) Yang, H.; Yan, F.; Lin, Y.; Wang, T. Enhanced Recoverable Energy Storage Density and High Efficiency of $SrTiO_3$-Based Lead-Free Ceramics. *Appl. Phys. Lett.* **2017**, *111*, 253903.

(248) Yang, H.; Yan, F.; Lin, Y.; Wang, T. Novel Strontium Titanate-Based Lead-Free Ceramics for High-Energy Storage Applications. *ACS Sustainable Chem. Eng.* **2017**, *5*, 10215−10222.

(249) Tao, H.; Wu, W.; Wu, J. Electrical Properties of Holmium Doped $(K,Na)(Nb,Sb)O_3$-$(Bi,Na)HfO_3$ Ceramics with Wide Sintering and Poling Temperature Range. *J. Alloys Compd.* **2016**, *689*, 759−766.

(250) Qu, B.; Du, H.; Yang, Z.; Liu, Q.; Liu, T. Enhanced Dielectric Breakdown Strength and Energy Storage Density in Lead-Free Relaxor Ferroelectric Ceramics Prepared Using Transition Liquid Phase Sintering. *RSC Adv.* **2016**, *6*, 34381−34389.

(251) Yang, Z.; Gao, F.; Du, H.; Jin, L.; Yan, L.; Hu, Q.; Yu, Y.; Qu, S.; Wei, X.; Xu, Z.; et al. Grain Size Engineered Lead-Free Ceramics with Both Large Energy Storage Density and Ultrahigh Mechanical Properties. *Nano Energy* **2019**, *58*, 768−777.

(252) Tao, H.; Wu, J. Optimization of Energy Storage Density in Relaxor (K, Na, Bi)NbO_3 Ceramics. *J. Mater. Sci.: Mater. Electron.* **2017**, *28*, 16199−16204.

(253) Qiao, X.; Zhang, X.; Wu, D.; Chao, X.; Yang, Z. Influence of Bi Nonstoichiometry on the Energy Storage Properties of 0.93knn-$0.07Bi_xMN$ Relaxor Ferroelectrics. *J. Adv. Dielectr.* **2018**, *08*, 1830006.

(254) Li, Y.; Zhen, Y.; Wang, W.; Fang, Z.; Jia, Z.; Zhang, J.; Zhong, H.; Wu, J.; Yan, Y.; Xue, Q.; et al. Enhanced Energy Storage Density and Discharge Efficiency in Potassium Sodium Niobite-Based Ceramics

Prepared Using a New Scheme. *J. Eur. Ceram. Soc.* **2020**, *40*, 2357−2365.

(255) Zhang, M.; Yang, H.; Li, D.; Ma, L.; Lin, Y. Giant Energy Storage Efficiency and High Recoverable Energy Storage Density Achieved in $K_{0.5}Na_{0.5}NbO_3$-$Bi(Zn_{0.5}\ Zr_{0.5})O_3$ Ceramics. *J. Mater. Chem. C* **2020**, *8*, 8777−8785.

(256) Li, Y.; Cao, M.-S.; Wang, D.-W.; Yuan, J. High-Efficiency and Dynamic Stable Electromagnetic Wave Attenuation for La Doped Bismuth Ferrite at Elevated Temperature and Gigahertz Frequency. *RSC Adv.* **2015**, *5*, 77184−77191.

(257) Li, Y.; Cao, W.-Q.; Yuan, J.; Wang, D.-W.; Cao, M.-S. Nd Doping of Bismuth Ferrite to Tune Electromagnetic Properties and Increase Microwave Absorption by Magnetic-Dielectric Synergy. *J. Mater. Chem. C* **2015**, *3*, 9276−9282.

(258) Wang, D.; Wang, M.; Liu, F.; Cui, Y.; Zhao, Q.; Sun, H.; Jin, H.; Cao, M. Sol-Gel Synthesis of Nd-Doped $BiFeO_3$ Multiferroic and Its Characterization. *Ceram. Int.* **2015**, *41*, 8768−8772.

(259) Li, Z.-J.; Hou, Z.-L.; Song, W.-L.; Liu, X.-D.; Wang, D.-W.; Tang, J.; Shao, X.-H. Mg-Substitution for Promoting Magnetic and Ferroelectric Properties of $BiFeO_3$ Multiferroic Nanoparticles. *Mater. Lett.* **2016**, *175*, 207−211.

(260) Wang, G.; Fan, Z.; Murakami, S.; Lu, Z.; Hall, D. A.; Sinclair, D. C.; Feteira, A.; Tan, X.; Jones, J. L.; Kleppe, A. K.; et al. Origin of the Large Electrostrain in $BiFeO_3$-$BaTiO_3$ Based Lead-Free Ceramics. *J. Mater. Chem. A* **2019**, *7*, 21254−21263.

(261) Rojac, T.; Bencan, A.; Malic, B.; Tutuncu, G.; Jones, J. L.; Daniels, J. E.; Damjanovic, D. $BiFeO_3$ Ceramics: Processing, Electrical, and Electromechanical Properties. *J. Am. Ceram. Soc.* **2014**, *97*, 1993−2011.

(262) Masó, N.; West, A. R. Electrical Properties of Ca-Doped $BiFeO_3$ Ceramics: From P-Type Semiconduction to Oxide-Ion Conduction. *Chem. Mater.* **2012**, *24*, 2127−2132.

(263) Yuan, G. L.; Baba-Kishi, K. Z.; Liu, J. M.; Wing Or, S.; Wang, Y. P.; Liu, Z. G. Multiferroic Properties of Single-Phase $Bi_{0.85}$ $la_{0.15}$ feo_3 Lead-Free Ceramics. *J. Am. Ceram. Soc.* **2006**, *89*, 3136−3139.

(264) Leontsev, S.; Eitel, R. Topical Review: Progress in Engineering High Strain Lead-Free Piezoelectric Ceramics. *Sci. Technol. Adv. Mater.* **2010**, *11*, 044302.

(265) Wang, T.; Jin, L.; Tian, Y.; Shu, L.; Hu, Q.; Wei, X. Microstructure and Ferroelectric Properties of Nb_2O_5-Modified $BiFeO_3$-$BaTiO_3$ Lead-Free Ceramics for Energy Storage. *Mater. Lett.* **2014**, *137*, 79−81.

(266) Wang, D.; Fan, Z.; Li, W.; Zhou, D.; Feteira, A.; Wang, G.; Murakami, S.; Sun, S.; Zhao, Q.; Tan, X.; et al. High Energy Storage Density and Large Strain in $Bi(Zn_{2/3}Nb_{1/3})O_3$-Doped $BiFeO_3$-$BaTiO_3$ Ceramics. *ACS Appl. Energy Mater.* **2018**, *1*, 4403−4412.

(267) Zheng, D.; Zuo, R. Enhanced Energy Storage Properties in $La(Mg_{1/2}\ ti_{1/2})O_3$-Modified $BiFeO_3$-$BaTiO_3$ Lead-Free Relaxor Ferroelectric Ceramics within a Wide Temperature Range. *J. Eur. Ceram. Soc.* **2017**, *37*, 413−418.

(268) Sun, H.; Wang, X.; Sun, Q.; Zhang, X.; Ma, Z.; Guo, M.; Sun, B.; Zhu, X.; Liu, Q.; Lou, X. Large Energy Storage Density in $BiFeO_3$-$BaTiO_3$-$AgNbO_3$ Lead-Free Relaxor Ceramics. *J. Eur. Ceram. Soc.* **2020**, *40*, 2929−2935.

(269) Zheng, D.; Zuo, R.; Zhang, D.; Li, Y. Novel $BiFeO_3$-$BaTiO_3$-$Ba(Mg_{1/3}Nb_{2/3})O_3$ Lead-Free Relaxor Ferroelectric Ceramics for Energy-Storage Capacitors. *J. Am. Ceram. Soc.* **2015**, *98*, 2692−2695.

(270) Liu, N.; Liang, R.; Zhao, X.; Xu, C.; Zhou, Z.; Dong, X. Novel Bismuth Ferrite-Based Lead-Free Ceramics with High Energy and Power Density. *J. Am. Ceram. Soc.* **2018**, *101*, 3259−3265.

(271) Chen, Z.; Bu, X.; Ruan, B.; Du, J.; Zheng, P.; Li, L.; Wen, F.; Bai, W.; Wu, W.; Zheng, L.; et al. Simultaneously Achieving High Energy Storage Density and Efficiency under Low Electric Field in $BiFeO_3$-Based Lead-Free Relaxor Ferroelectric Ceramics. *J. Eur. Ceram. Soc.* **2020**, *40*, 5450−5457.

(272) Liu, N.; Liang, R.; Zhou, Z.; Dong, X. Designing Lead-Free Bismuth Ferrite-Based Ceramics Learning from Relaxor Ferroelectric Behavior for Simultaneous High Energy Density and Efficiency under Low Electric Field. *J. Mater. Chem. C* **2018**, *6*, 10211−10217.

(273) Chen, Z.; Bai, X.; Wang, H.; Du, J.; Bai, W.; Li, L.; Wen, F.; Zheng, P.; Wu, W.; Zheng, L.; et al. Achieving High-Energy Storage Performance in $0.67Bi1_{-x}Sm_xFeO_3$-$0.33BaTiO_3$ Lead-Free Relaxor Ferroelectric Ceramics. *Ceram. Int.* **2020**, *46*, 11549−11555.

(274) Li, Q.; Ji, S.; Wang, D.; Zhu, J.; Li, L.; Wang, W.; Zeng, M.; Hou, Z.; Gao, X.; Lu, X.; et al. Simultaneously Enhanced Energy Storage Density and Efficiency in Novel $BiFeO_3$-Based Lead-Free Ceramic Capacitors. *J. Eur. Ceram. Soc.* **2021**, *41*, 387−393.

(275) Yang, H.; Qi, H.; Zuo, R. Enhanced Breakdown Strength and Energy Storage Density in a New $BiFeO_3$-Based Ternary Lead-Free Relaxor Ferroelectric Ceramic. *J. Eur. Ceram. Soc.* **2019**, *39*, 2673−2679.

(276) Wang, G.; Lu, Z.; Yang, H.; Ji, H.; Mostaed, A.; Li, L.; Wei, Y.; Feteira, A.; Sun, S.; Sinclair, D. C.; et al. Fatigue Resistant Lead-Free Multilayer Ceramic Capacitors with Ultrahigh Energy Density. *J. Mater. Chem. A* **2020**, *8*, 11414−11423.

(277) Li, B.; Cao, M.-S.; Liu, J.; Wang, D.-W. Domain Structure and Enhanced Electrical Properties in Sodium Bismuth Titanate Ceramics Sintered from Crystals with Different Morphologies. *J. Am. Ceram. Soc.* **2016**, *99*, 2316−2326.

(278) Zhang, Y.; Liu, X.; Wang, G.; Li, Y.; Zhang, S.; Wang, D.; Sun, H. Enhanced Mechanical Energy Harvesting Capability in Sodium Bismuth Titanate Based Lead-Free Piezoelectric. *J. Alloys Compd.* **2020**, *825*, 154020.

(279) Lu, R.; Yuan, J.; Shi, H.; Li, B.; Wang, W.; Wang, D.; Cao, M. Morphology-Controlled Synthesis and Growth Mechanism of Lead-Free Bismuth Sodium Titanate Nanostructures Via the Hydrothermal Route. *CrystEngComm* **2013**, *15*, 3984−3991.

(280) McLaughlin, K.; Pascual-Gonzalez, C.; Wang, D.; Feteira, A. Site Occupancy and Electric-Field Induced Strain Response of Er-Doped $(Bi_{0.4}\ Na_{0.4}\ Sr_{0.2})TiO_3$ Ceramics. *J. Alloys Compd.* **2019**, *779*, 7−14.

(281) Wang, G.; Hall, D. A.; Comyn, T. P.; Daniel, L.; Kleppe, A. K. Structure and Ferroelectric Behaviour of $Na_{0.5}Bi_{0.5}TiO_3$-$KNbO_3$ Ceramics. *Adv. Appl. Ceram.* **2016**, *115*, 89−95.

(282) Wang, G.; Hall, D. A.; Li, Y.; Murray, C. A.; Tang, C. C. Structural Characterization of the Electric Field-Induced Ferroelectric Phase in $Na_{0.5}Bi_{0.5}TiO_3$-$KNbO_3$ Ceramics. *J. Eur. Ceram. Soc.* **2016**, *36*, 4015−4021.

(283) Wang, G.; Li, Y.; Murray, C. A.; Tang, C. C.; Hall, D. A. Thermally-Induced Phase Transformations in $Na_{0.5}Bi_{0.5}TiO_3$-$KNbO_3$ Ceramics. *J. Am. Ceram. Soc.* **2017**, *100*, 3293−3304.

(284) Wang, G.; Lu, Z.; Zhang, Z.; Feteira, A.; Tang, C. C.; Hall, D. A. Electric Field-Induced Irreversible Relaxor to Ferroelectric Phase Transformations in $Na_{0.5}Bi_{0.5}TiO_3$-$NaNbO_3$ Ceramics. *J. Am. Ceram. Soc.* **2019**, *102*, 7746−7754.

(285) Chen, P.; Zhang, L.; Cai, J.; Wang, Z.; Shi, W.; Jing, J.; Wei, F.; Liu, G.; Yan, Y.; Liu, H.; et al. Effect of Dy_2O_3 Content on the Dielectric, Ferroelectric, and Energy Storage Properties of Lead-Free $0.5Na_{0.5}Bi_{0.5}TiO_3$-$0.5SrTiO_3$ Bulk Ceramics. *J. Mater. Sci.: Mater. Electron* **2019**, *30*, 13556−13566.

(286) Kumar, A.; Kumar, R.; Singh, K.; Singh, S. Enhanced Electrocaloric Effect and Energy Storage Density in Lead-Free $0.8Na_{0.5}Bi_{0.5}TiO_3$-$0.2SrTiO_3$ Ceramics. *Phys. Status Solidi A* **2019**, *216*, 1800786.

(287) Kandula, K. R.; Banerjee, K.; Raavi, S. S. K.; Asthana, S. Enhanced Electrocaloric Effect and Energy Storage Density of Nd-Substituted 0.92NBT-0.08BT Lead Free Ceramic. *Phys. Status Solidi A* **2018**, *215*, 1700915.

(288) Hu, D.; Pan, Z.; Zhang, X.; Ye, H.; He, Z.; Wang, M.; Xing, S.; Zhai, J.; Fu, Q.; Liu, J. Greatly Enhanced Discharge Energy Density and Efficiency of Novel Relaxation Ferroelectric BNT-BKT-Based Ceramics. *J. Mater. Chem. C* **2020**, *8*, 591−601.

(289) Cao, W.; Li, W.; Zhang, T.; Sheng, J.; Hou, Y.; Feng, Y.; Yu, Y.; Fei, W. High-Energy Storage Density and Efficiency of (1-X)-[0.94NBT-0.06BT]-xST Lead-Free Ceramics. *Energy Technol.* **2015**, *3*, 1198−1204.

(290) Liu, Z.; Zhang, A.; Xu, S.; Lu, J.; Xie, B.; Guo, K.; Mao, Y. Mediating the Confliction of Polarizability and Breakdown Electric-

Field Strength in Bnst Relaxor Ferroelectric for Energy Storage Applications. *J. Alloys Compd.* **2020**, *823*, 153772.

(291) Zhang, L.; Pu, Y.; Chen, M.; Wei, T.; Peng, X. Novel $Na_{0.5}Bi_{0.5}TiO_3$ Based, Lead-Free Energy Storage Ceramics with High Power and Energy Density and Excellent High-Temperature Stability. *Chem. Eng. J.* **2020**, *383*, 123154.

(292) Wu, J.; Mahajan, A.; Riekehr, L.; Zhang, H.; Yang, B.; Meng, N.; Zhang, Z.; Yan, H. Perovskite $Srx(Bi_{1-X}\ Na_{0.97-X}\ Li_{0.03})_{0.5}\ TiO_3$ Ceramics with Polar Nano Regions for High Power Energy Storage. *Nano Energy* **2018**, *50*, 723−732.

(293) Borkar, H.; Singh, V. N.; Singh, B. P.; Tomar, M.; Gupta, V.; Kumar, A. Room Temperature Lead-Free Relaxor-Antiferroelectric Electroceramics for Energy Storage Applications. *RSC Adv.* **2014**, *4*, 22840−22847.

(294) Luo, W.-Q.; Shen, Z.-Y.; Yu, Y.-Y.; Song, F.-S.; Wang, Z.-M.; Li, Y.-M. Structure and Dielectric Properties of NBT-xBT-ST Lead-Free Ceramics for Energy Storage. *J. Adv. Dielectr.* **2018**, *08*, 1820004.

(295) Qiao, X.; Zhang, F.; Wu, D.; Chen, B.; Zhao, X.; Peng, Z.; Ren, X.; Liang, P.; Chao, X.; Yang, Z. Superior Comprehensive Energy Storage Properties in $Bi_{0.5}Na_{0.5}TiO_3$-Based Relaxor Ferroelectric Ceramics. *Chem. Eng. J.* **2020**, *388*, 124158.

(296) Li, F.; Yang, K.; Liu, X.; Zou, J.; Zhai, J.; Shen, B.; Li, P.; Shen, J.; Liu, B.; Chen, P.; et al. Temperature Induced High Charge-Discharge Performances in Lead-Free $Bi_{0.5}Na_{0.5}TiO_3$-Based Ergodic Relaxor Ferroelectric Ceramics. *Scr. Mater.* **2017**, *141*, 15−19.

(297) Qi, H.; Zuo, R. Linear-Like Lead-Free Relaxor Antiferroelectric $(Bi_{0.5}Na_{0.5})TiO_3$-$NaNbO_3$ with Giant Energy-Storage Density/Efficiency and Super Stability against Temperature and Frequency. *J. Mater. Chem. A* **2019**, *7*, 3971−3978.

(298) Pan, Z.; Hu, D.; Zhang, Y.; Liu, J.; Shen, B.; Zhai, J. Achieving High Discharge Energy Density and Efficiency with NBT-Based Ceramics for Application in Capacitors. *J. Mater. Chem. C* **2019**, *7*, 4072−4078.

(299) Huang, Y.; Li, F.; Hao, H.; Xia, F.; Liu, H.; Zhang, S. $(Bi_{0.51}\ Na_{0.47})TiO_3$ Based Lead Free Ceramics with High Energy Density and Efficiency. *J. Materiomics* **2019**, *5*, 385−393.

(300) Qiu, Y.; Lin, Y.; Liu, X.; Yang, H. $Bi(Mg_{2/3}Nb_{1/3})O_3$ Addition Inducing High Recoverable Energy Storage Density in Lead-Free $0.65BaTiO_3$-$0.35Bi_{0.5}Na_{0.5}TiO_3$ Bulk Ceramics. *J. Alloys Compd.* **2019**, *797*, 348−355.

(301) Ren, P.; Liu, Z.; Wang, X.; Duan, Z.; Wan, Y.; Yan, F.; Zhao, G. Dielectric and Energy Storage Properties of $SrTiO_3$ and $Srzro_3$ Modified $Bi_{0.5}Na_{0.5}TiO_3$-$Sr_{0.8}Bi_{0.1}\square_{0.1}$ tio_3 Based Ceramics. *J. Alloys Compd.* **2018**, *742*, 683−689.

(302) Yao, M.; Pu, Y.; Zhang, L.; Chen, M. Enhanced Energy Storage Properties of $(1\text{-}X)Bi_{0.5}Na_{0.5}TiO_3$-$XBa_{0.85}\ Ca_{0.15}\ Ti_{0.9}\ Zr_{0.1}O_3$ Ceramics. *Mater. Lett.* **2016**, *174*, 110−113.

(303) Yin, J.; Lv, X.; Wu, J. Enhanced Energy Storage Properties of $\{Bi_{0.5}[(Na_{0.8}K_{0.2})_{1\text{-}Z}\ Li_z]_{0.5}\}_{0.96}\ Sr_{0.04}(Ti_{1\text{-}X\text{-}Y}\ Ta_x\ Nb_y)O_3$ Lead-Free Ceramics. *Ceram. Int.* **2017**, *43*, 13541−13546.

(304) Liu, X.; Yang, H.; Yan, F.; Qin, Y.; Lin, Y.; Wang, T. Enhanced Energy Storage Properties of $BaTiO_3$-$Bi_{0.5}Na_{0.5}TiO_3$ Lead-Free Ceramics Modified by $SrY_{0.5}Nb_{0.5}O_3$. *J. Alloys Compd.* **2019**, *778*, 97−104.

(305) Hu, B.; Fan, H.; Ning, L.; Gao, S.; Yao, Z.; Li, Q. Enhanced Energy-Storage Performance and Dielectric Temperature Stability of $(1\text{-}X)(0.65bi_{0.5}\ na_{0.5}\ tio_3$-$0.35bi_{0.1}\ sr_{0.85}\ tio_3)$-$Xknbo_3$ Ceramics. *Ceram. Int.* **2018**, *44*, 10968−10974.

(306) Zhang, L.; Pu, Y.; Chen, M.; Li, R.; Guo, X.; Cui, Y. Enhanced Energy-Storage Properties of $(1\text{-}X)Na_{0.5}Bi_{0.5}TiO_3$-$XBaSnO_3$ Ceramics. *Ceram. Int.* **2018**, *44*, S207−S210.

(307) Xu, Y.; Hou, Y.; Zhao, H.; Zheng, M.; Zhu, M. Enhanced High-Temperature Energy Storage Properties in Fine-Grained Lead-Free Ceramic with High Insulation Resistivity. *Mater. Lett.* **2019**, *249*, 21−24.

(308) Yang, Y.; Wang, H.; Bi, L.; Zheng, Q.; Fan, G.; Jie, W.; Lin, D. High Energy Storage Density and Discharging Efficiency in La^{3+}/Nb^{5+}-Co-Substituted $(Bi_{0.5}Na_{0.5})_{0.94}\ Ba_{0.06}\ TiO_3$ Ceramics. *J. Eur. Ceram. Soc.* **2019**, *39*, 3051−3056.

(309) Hu, B.; Fan, H.; Ning, L.; Wen, Y.; Wang, C. High Energy Storage Performance of $[(Bi_{0.5}Na_{0.5})_{0.94}\ Ba_{0.06}]_{0.97}\ La_{0.03}\ Ti_{1\text{-}X}(Al_{0.5}\ Nb_{0.5})_XO_3$ Ceramics with Enhanced Dielectric Breakdown Strength. *Ceram. Int.* **2018**, *44*, 15160−15166.

(310) Zhang, L.; Pu, Y.; Chen, M.; Wei, T.; Keipper, W.; Shi, R.; Guo, X.; Li, R.; Peng, X. High Energy-Storage Density under Low Electric Fields and Improved Optical Transparency in Novel Sodium Bismuth Titanate-Based Lead-Free Ceramics. *J. Eur. Ceram. Soc.* **2020**, *40*, 71−77.

(311) Sui, J.; Fan, H.; Hu, B.; Ning, L. High Temperature Stable Dielectric Properties and Enhanced Energy-Storage Performance of $(1\text{-}X)(0.85na_{0.5}\ bi_{0.5}\ tio_3 - 0.15ba_{0.8}\ ca_{0.2}\ ti_{0.8}\ zr_{0.2}o_3)$-$xK_{0.5}Na_{0.5}NbO_3$ Lead-Free Ceramics. *Ceram. Int.* **2018**, *44*, 18054−18059.

(312) Butnoi, P.; Manotham, S.; Jaita, P.; Randorn, C.; Rujijanagul, G. High Thermal Stability of Energy Storage Density and Large Strain Improvement of Lead-Free $Bi_{0.5}(Na_{0.40}K_{0.10})TiO_3$ Piezoelectric Ceramics Doped with La and Zr. *J. Eur. Ceram. Soc.* **2018**, *38*, 3822−3832.

(313) Chen, P.; Chu, B. Improvement of Dielectric and Energy Storage Properties in $Bi(Mg_{1/2}\ Ti_{1/2})O_3$-Modified $(Na_{1/2}\ Bi_{1/2})_{0.92}\ Ba_{0.08}\ TiO_3$ Ceramics. *J. Eur. Ceram. Soc.* **2016**, *36*, 81−88.

(314) Zhang, L.; Pu, X.; Chen, M.; Bai, S.; Pu, Y. Influence of $BaSnO_3$ Additive on the Energy Storage Properties of $Na_{0.5}Bi_{0.5}TiO_3$-Based Relaxor Ferroelectrics. *J. Eur. Ceram. Soc.* **2018**, *38*, 2304−2311.

(315) Zhang, L.; Pu, Y.; Chen, M. Influence of $Bazro_3$ Additive on the Energy-Storage Properties of $0.775Na_{0.5}\ Bi_{0.5}\ TiO_3$-$0.225BaSnO_3$ Relaxor Ferroelectrics. *J. Alloys Compd.* **2019**, *775*, 342−347.

(316) Lin, Y.; Li, D.; Zhang, M.; Yang, H. $(Na_{0.5}\ Bi_{0.5})_{0.7}\ Sr_{0.3}\ TiO_3$ Modified by $Bi(Mg_{2/3}Nb_{1/3})O_3$ Ceramics with High Energy-Storage Properties and an Ultrafast Discharge Rate. *J. Mater. Chem. C* **2020**, *8*, 2258−2264.

(317) Liu, G.; Dong, J.; Zhang, L.; Yu, L.; Wei, F.; Li, Y.; Gao, J.; Hu, J.; Yan, Y.; Li, Q.; et al. $Na_{0.25}\ sr_{0.5}\ bi_{0.25}\ tio_3$ Relaxor Ferroelectric Ceramic with Greatly Enhanced Electric Storage Property by a B-Site Ion Doping. *Ceram. Int.* **2020**, *46*, 11680−11688.

(318) Yang, Z.; Yuan, Y.; Cao, L.; Li, E.; Zhang, S. Relaxor Ferroelectric $(Na_{0.5}\ Bi_{0.5})_{0.4}\ Sr_{0.6}\ TiO_3$-Based Ceramics for Energy Storage Application. *Ceram. Int.* **2020**, *46*, 11282−11289.

(319) Xu, Q.; Liu, H.; Zhang, L.; Xie, J.; Hao, H.; Cao, M.; Yao, Z.; Lanagan, M. T. Structure and Electrical Properties of Lead-Free $Bi_{0.5}Na_{0.5}TiO_3$-Based Ceramics for Energy-Storage Applications. *RSC Adv.* **2016**, *6*, 59280−59291.

(320) Zhang, L.; Pu, Y.; Chen, M. Ultra-High Energy Storage Performance under Low Electric Fields in $Na_{0.5}Bi_{0.5}TiO_3$-Based Relaxor Ferroelectrics for Pulse Capacitor Applications. *Ceram. Int.* **2020**, *46*, 98−105.

(321) Yang, L.; Kong, X.; Cheng, Z.; Zhang, S. Ultra-High Energy Storage Performance with Mitigated Polarization Saturation in Lead-Free Relaxors. *J. Mater. Chem. A* **2019**, *7*, 8573−8580.

(322) Qiao, X.; Wu, D.; Zhang, F.; Chen, B.; Ren, X.; Liang, P.; Du, H.; Chao, X.; Yang, Z. $Bi_{0.5}Na_{0.5}TiO_3$-Based Relaxor Ferroelectric Ceramic with Large Energy Density and High Efficiency under a Moderate Electric Field. *J. Mater. Chem. C* **2019**, *7*, 10514−10520.

(323) Wu, Y.; Fan, Y.; Liu, N.; Peng, P.; Zhou, M.; Yan, S.; Cao, F.; Dong, X.; Wang, G. Enhanced Energy Storage Properties in Sodium Bismuth Titanate-Based Ceramics for Dielectric Capacitor Applications. *J. Mater. Chem. C* **2019**, *7*, 6222−6230.

(324) Ma, W.; Zhu, Y.; Marwat, M. A.; Fan, P.; Xie, B.; Salamon, D.; Ye, Z.-G.; Zhang, H. Enhanced Energy-Storage Performance with Excellent Stability under Low Electric Fields in BNT-St Relaxor Ferroelectric Ceramics. *J. Mater. Chem. C* **2019**, *7*, 281−288.

(325) Zhu, C.; Cai, Z.; Luo, B.; Guo, L.; Li, L.; Wang, X. High Temperature Lead-Free BNT-Based Ceramics with Stable Energy Storage and Dielectric Properties. *J. Mater. Chem. A* **2020**, *8*, 683−692.

(326) Zhang, L.; Pu, Y.; Chen, M.; Liu, G. Antiferroelectric-Like Properties in MgO-Modified $0.775Na_{0.5}Bi_{0.5}TiO_3$-$0.225BaSnO_3$ Ceramics for High Power Energy Storage. *J. Eur. Ceram. Soc.* **2018**, *38*, 5388−5395.

(327) Tao, C.-W.; Geng, X.-Y.; Zhang, J.; Wang, R.-X.; Gu, Z.-B.; Zhang, S.-T. $Bi_{0.5}Na_{0.5}TiO_3$-$BaTiO_3$-$K_{0.5}Na_{0.5}NbO_3$:ZnO Relaxor

Ferroelectric Composites with High Breakdown Electric Field and Large Energy Storage Properties. *J. Eur. Ceram. Soc.* **2018**, *38*, 4946−4952.

(328) Cui, C.; Pu, Y. Effect of Sn Substitution on the Energy Storage Properties of 0.45SrTiO$_3$-0.2Na$_{0.5}$Bi$_{0.5}$TiO$_3$-0.35BaTiO$_3$ Ceramics. *J. Mater. Sci.* **2018**, *53*, 9830−9841.

(329) Yao, Y.; Li, Y.; Sun, N.; Du, J.; Li, X.; Zhang, L.; Zhang, Q.; Hao, X. Enhanced Dielectric and Energy-Storage Properties in ZnO-Doped 0.9(0.94Na$_{0.5}$Bi$_{0.5}$TiO$_3$-0.06BaTiO$_3$)-0.1NaNbO$_3$ Ceramics. *Ceram. Int.* **2018**, *44*, 5961−5966.

(330) Shi, W.; Zhang, L.; Chen, P.; Li, Y.; Wang, Y.; Liu, G.; Yu, K.; Yan, Y. The Ferroelectric, Dielectric and Energy Storage Properties of Pb-Free 0.6Na$_{0.5}$Bi$_{0.5}$TiO$_3$-0.4SrTiO$_3$ Bulk Ceramics Modified by Fe$_2$O$_3$. *Mater. Res. Express* **2019**, *6*, 086329.

(331) Chen, P.; Zhang, L.; Wang, Z.; Wang, Y.; Song, C.; Hu, J.; Liu, G.; Yan, Y. Improved Dielectric Energy Storage Performance of Pb-Free 0.5Na$_{0.5}$Bi$_{0.5}$TiO$_3$-0.5SrTiO$_3$ Ceramics Modified with Cao. *J. Adv. Dielectr.* **2018**, *08*, 1850042.

(332) Cao, W. P.; Sheng, J.; Qiao, Y. L.; Jing, L.; Liu, Z.; Wang, J.; Li, W. L. Optimized Strain with Small Hysteresis and High Energy-Storage Density in Mn-Doped NBT-ST System. *J. Eur. Ceram. Soc.* **2019**, *39*, 4046−4052.

(333) Li, F.; Zhai, J.; Shen, B.; Liu, X.; Zeng, H. Simultaneously High-Energy Storage Density and Responsivity in Quasi-Hysteresis-Free Mn-Doped Bi$_{0.5}$Na$_{0.5}$TiO$_3$-BaTiO$_3$-(Sr$_{0.7}$ Bi$_{0.2}\square_{0.1}$)TiO$_3$ Ergodic Relaxor Ceramics. *Mater. Res. Lett.* **2018**, *6*, 345−352.

(334) Li, F.; Hou, X.; Wang, J.; Zeng, H.; Shen, B.; Zhai, J. Structure-Design Strategy of 0−3 Type (Bi$_{0.32}$ sr$_{0.42}$ na$_{0.20}$)TiO$_3$/MgO Composite to Boost Energy Storage Density, Efficiency and Charge-Discharge Performance. *J. Eur. Ceram. Soc.* **2019**, *39*, 2889−2898.

(335) Verma, A.; Yadav, A. K.; Kumar, S.; Srihari, V.; Jangir, R.; Poswal, H. K.; Biring, S.; Sen, S. Enhanced Energy Storage Properties in a-Site Substituted Na$_{0.5}$Bi$_{0.5}$TiO$_3$ Ceramics. *J. Alloys Compd.* **2019**, *792*, 95−107.

(336) Verma, A.; Yadav, A. K.; Kumar, S.; Srihari, V.; Jangir, R.; Poswal, H. K.; Biring, S.; Sen, S. Structural, Thermally Stable Dielectric, and Energy Storage Properties of Lead-Free (1-X)(Na$_{0.50}$Bi$_{0.50}$)TiO$_3$-xKSbO$_3$ Ceramics. *J. Mater. Sci.: Mater. Electron* **2019**, *30*, 15005−15017.

(337) Ji, H.; Bao, W.; Lu, Z.; Wang, G.; Li, J.; Yang, H.; Mostaed, A.; Li, L.; Feteira, A.; Xu, F.; et al. Ultrahigh Energy Density in Short-Range Tilted Lead-Free Multilayer Ceramic Capacitors by Nanodomain Percolation. *Energy Storage Mater.* **2021**, *38*, 113−120.

(338) Pu, Y.; Zhang, L.; Cui, Y.; Chen, M. High Energy Storage Density and Optical Transparency of Microwave Sintered Homogeneous (Na$_{0.5}$Bi$_{0.5}$)(1-x)Ba$_x$Ti$_{(1-y)}$Sn$_y$O$_3$ Ceramics. *ACS Sustainable Chem. Eng.* **2018**, *6*, 6102−6109.

(339) Yin, J.; Zhang, Y.; Lv, X.; Wu, J. Ultrahigh Energy-Storage Potential under Low Electric Field in Bismuth Sodium Titanate-Based Perovskite Ferroelectrics. *J. Mater. Chem. A* **2018**, *6*, 9823−9832.

(340) Zhao, X.; Bai, W.; Ding, Y.; Wang, L.; Wu, S.; Zheng, P.; Li, P.; Zhai, J. Tailoring High Energy Density with Superior Stability under Low Electric Field in Novel (Bi$_{0.5}$Na$_{0.5}$)TiO$_3$-Based Relaxor Ferroelectric Ceramics. *J. Eur. Ceram. Soc.* **2020**, *40*, 4475−4486.

(341) Li, D.; Lin, Y.; Yuan, Q.; Zhang, M.; Ma, L.; Yang, H. A Novel Lead-Free Na$_{0.5}$Bi$_{0.5}$TiO$_3$-Based Ceramic with Superior Comprehensive Energy Storage and Discharge Properties for Dielectric Capacitor Applications. *J. Materiomics* **2020**, *6*, 743−750.

(342) Yan, F.; Huang, K.; Jiang, T.; Zhou, X.; Shi, Y.; Ge, G.; Shen, B.; Zhai, J. Significantly Enhanced Energy Storage Density and Efficiency of BNT-Based Perovskite Ceramics Via a-Site Defect Engineering. *Energy Storage Mater.* **2020**, *30*, 392−400.

(343) Tian, Y.; Jin, L.; Zhang, H.; Xu, Z.; Wei, X.; Politova, E. D.; Stefanovich, S. Y.; Tarakina, N. V.; Abrahams, I.; Yan, H. High Energy Density in Silver Niobate Ceramics. *J. Mater. Chem. A* **2016**, *4*, 17279−17287.

(344) Yang, D.; Gao, J.; Shu, L.; Liu, Y.-X.; Yu, J.; Zhang, Y.; Wang, X.; Zhang, B.-P.; Li, J.-F. Lead-Free Antiferroelectric Niobates AgNbO$_3$ and NaNbO$_3$ for Energy Storage Applications. *J. Mater. Chem. A* **2020**, *8*, 23724−23737.

(345) Gao, J.; Zhao, L.; Liu, Q.; Wang, X.; Zhang, S.; Li, J.-F. Antiferroelectric-Ferroelectric Phase Transition in Lead-Free AgNbO$_3$ Ceramics for Energy Storage Applications. *J. Am. Ceram. Soc.* **2018**, *101*, 5443−5450.

(346) Zhao, L.; Liu, Q.; Zhang, S.; Li, J.-F. Lead-Free AgNbO$_3$ Anti-Ferroelectric Ceramics with an Enhanced Energy Storage Performance Using Mno$_2$ Modification. *J. Mater. Chem. C* **2016**, *4*, 8380−8384.

(347) Zhao, L.; Gao, J.; Liu, Q.; Zhang, S.; Li, J.-F. Silver Niobate Lead-Free Antiferroelectric Ceramics: Enhancing Energy Storage Density by B-Site Doping. *ACS Appl. Mater. Interfaces* **2018**, *10*, 819−826.

(348) Luo, N.; Han, K.; Zhuo, F.; Xu, C.; Zhang, G.; Liu, L.; Chen, X.; Hu, C.; Zhou, H.; Wei, Y. Aliovalent a-Site Engineered AgNbO$_3$ Lead-Free Antiferroelectric Ceramics toward Superior Energy Storage Density. *J. Mater. Chem. A* **2019**, *7*, 14118−14128.

(349) Luo, N.; Han, K.; Zhuo, F.; Liu, L.; Chen, X.; Peng, B.; Wang, X.; Feng, Q.; Wei, Y. Design for High Energy Storage Density and Temperature-Insensitive Lead-Free Antiferroelectric Ceramics. *J. Mater. Chem. C* **2019**, *7*, 4999−5008.

(350) Gao, J.; Zhang, Y.; Zhao, L.; Lee, K.-Y.; Liu, Q.; Studer, A.; Hinterstein, M.; Zhang, S.; Li, J. Enhanced Antiferroelectric Phase Stability in La-Doped AgNbO$_3$: Perspectives from the Microstructure to Energy Storage Properties. *J. Mater. Chem. A* **2019**, *7*, 2225−2232.

(351) Xu, C.; Fu, Z.; Liu, Z.; Wang, L.; Yan, S.; Chen, X.; Cao, F.; Dong, X.; Wang, G. La/Mn Codoped AgNbO$_3$ Lead-Free Antiferroelectric Ceramics with Large Energy Density and Power Density. *ACS Sustainable Chem. Eng.* **2018**, *6*, 16151−16159.

(352) Luo, N.; Han, K.; Liu, L.; Peng, B.; Wang, X.; Hu, C.; Zhou, H.; Feng, Q.; Chen, X.; Wei, Y. Lead-Free Ag$_{1-3x}$ La$_x$NbO$_3$ Antiferroelectric Ceramics with High-Energy Storage Density and Efficiency. *J. Am. Ceram. Soc.* **2019**, *102*, 4640−4647.

(353) Tian, Y.; Jin, L.; Zhang, H.; Xu, Z.; Wei, X.; Viola, G.; Abrahams, I.; Yan, H. Phase Transitions in Bismuth-Modified Silver Niobate Ceramics for High Power Energy Storage. *J. Mater. Chem. A* **2017**, *5*, 17525−17531.

(354) Han, K.; Luo, N.; Mao, S.; Zhuo, F.; Chen, X.; Liu, L.; Hu, C.; Zhou, H.; Wang, X.; Wei, Y. Realizing High Low-Electric-Field Energy Storage Performance in AgNbO$_3$ Ceramics by Introducing Relaxor Behaviour. *J. Materiomics* **2019**, *5*, 597−605.

(355) Li, S.; Nie, H.; Wang, G.; Xu, C.; Liu, N.; Zhou, M.; Cao, F.; Dong, X. Significantly Enhanced Energy Storage Performance of Rare-Earth-Modified Silver Niobate Lead-Free Antiferroelectric Ceramics Via Local Chemical Pressure Tailoring. *J. Mater. Chem. C* **2019**, *7*, 1551−1560.

(356) Han, K.; Luo, N.; Jing, Y.; Wang, X.; Peng, B.; Liu, L.; Hu, C.; Zhou, H.; Wei, Y.; Chen, X.; et al. Structure and Energy Storage Performance of Ba-Modified AgNbO$_3$ Lead-Free Antiferroelectric Ceramics. *Ceram. Int.* **2019**, *45*, 5559−5565.

(357) Zhao, L.; Liu, Q.; Gao, J.; Zhang, S.; Li, J.-F. Lead-Free Antiferroelectric Silver Niobate Tantalate with High Energy Storage Performance. *Adv. Mater.* **2017**, *29*, 1701824.

(358) Tian, Y.; Jin, L.; Hu, Q.; Yu, K.; Zhuang, Y.; Viola, G.; Abrahams, I.; Xu, Z.; Wei, X.; Yan, H. Phase Transitions in Tantalum-Modified Silver Niobate Ceramics for High Power Energy Storage. *J. Mater. Chem. A* **2019**, *7*, 834−842.

(359) Han, K.; Luo, N.; Mao, S.; Zhuo, F.; Liu, L.; Peng, B.; Chen, X.; Hu, C.; Zhou, H.; Wei, Y. Ultrahigh Energy-Storage Density in a-/B-Site Co-Doped AgNbO$_3$ Lead-Free Antiferroelectric Ceramics: Insight into the Origin of Antiferroelectricity. *J. Mater. Chem. A* **2019**, *7*, 26293−26301.

(360) Song, A.; Song, J.; Lv, Y.; Liang, L.; Wang, J.; Zhao, L. Energy Storage Performance in Bimno$_3$-Modified AgNbO$_3$ Anti-Ferroelectric Ceramics. *Mater. Lett.* **2019**, *237*, 278−281.

(361) Yan, Z.; Zhang, D.; Zhou, X.; Qi, H.; Luo, H.; Zhou, K.; Abrahams, I.; Yan, H. Silver Niobate Based Lead-Free Ceramics with High Energy Storage Density. *J. Mater. Chem. A* **2019**, *7*, 10702−10711.

(362) Gao, J.; Liu, Q.; Dong, J.; Wang, X.; Zhang, S.; Li, J.-F. Local Structure Heterogeneity in Sm-Doped $AgNbO_3$ for Improved Energy-Storage Performance. *ACS Appl. Mater. Interfaces* **2020**, *12*, 6097−6104.

(363) Chao, W.; Yang, T.; Li, Y.; Liu, Z. Enhanced Energy Storage Density in Ca and Ta Co-Doped $AgNbO_3$ Antiferroelectric Ceramics. *J. Am. Ceram. Soc.* **2020**, *103*, 7283−7290.

(364) Xu, Y.; Guo, Y.; Liu, Q.; Wang, G.; Bai, J.; Tian, J.; Lin, L.; Tian, Y. High Energy Storage Properties of Lead-Free Mn-Doped (1-X)$AgNbO_3$-$Xbi_{0.5}$ $Na_{0.5}TiO_3$ Antiferroelectric Ceramics. *J. Eur. Ceram. Soc.* **2020**, *40*, 56−62.

(365) Luo, N.; Han, K.; Cabral, M. J.; Liao, X.; Zhang, S.; Liao, C.; Zhang, G.; Chen, X.; Feng, Q.; Li, J.-F.; et al. Constructing Phase Boundary in $AgNbO_3$ Antiferroelectrics: Pathway Simultaneously Achieving High Energy Density and Efficiency. *Nat. Commun.* **2020**, *11*, 4824.

(366) Lu, Z.; Bao, W.; Wang, G.; Sun, S.-K.; Li, L.; Li, J.; Yang, H.; Ji, H.; Feteira, A.; Li, D.; et al. Mechanism of Enhanced Energy Storage Density in $AgNbO_3$-Based Lead-Free Antiferroelectrics. *Nano Energy* **2021**, *79*, 105423.

(367) Li, S.; Hu, T.; Nie, H.; Fu, Z.; Xu, C.; Xu, F.; Wang, G.; Dong, X. Giant Energy Density and High Efficiency Achieved in Silver Niobate-Based Lead-Free Antiferroelectric Ceramic Capacitors Via Domain Engineering. *Energy Storage Mater.* **2021**, *34*, 417−426.

(368) Gao, L.; Guo, H.; Zhang, S.; Randall, C. A. Stabilized Antiferroelectricity in $xBiScO_3$-(1-X)$NaNbO_3$ Lead-Free Ceramics with Established Double Hysteresis Loops. *Appl. Phys. Lett.* **2018**, *112*, 092905.

(369) Gao, L.; Guo, H.; Zhang, S.; Randall, C. A. A Perovskite Lead-Free Antiferroelectric $xCaHfO_3$-(1-X) $NaNbO_3$ with Induced Double Hysteresis Loops at Room Temperature. *J. Appl. Phys.* **2016**, *120*, 204102.

(370) Guo, H.; Shimizu, H.; Randall, C. A. Direct Evidence of an Incommensurate Phase in $NaNbO_3$ and Its Implication in $NaNbO_3$-Based Lead-Free Antiferroelectrics. *Appl. Phys. Lett.* **2015**, *107*, 112904.

(371) Ye, J.; Wang, G.; Zhou, M.; Liu, N.; Chen, X.; Li, S.; Cao, F.; Dong, X. Excellent Comprehensive Energy Storage Properties of Novel Lead-Free $NaNbO_3$-Based Ceramics for Dielectric Capacitor Applications. *J. Mater. Chem. C* **2019**, *7*, 5639−5645.

(372) Zhou, M.; Liang, R.; Zhou, Z.; Yan, S.; Dong, X. Novel Sodium Niobate-Based Lead-Free Ceramics as New Environment-Friendly Energy Storage Materials with High Energy Density, High Power Density, and Excellent Stability. *ACS Sustainable Chem. Eng.* **2018**, *6*, 12755−12765.

(373) Shi, J.; Chen, X.; Li, X.; Sun, J.; Sun, C.; Pang, F.; Zhou, H. Realizing Ultrahigh Recoverable Energy Density and Superior Charge-Discharge Performance in $NaNbO_3$-Based Lead-Free Ceramics Via a Local Random Field Strategy. *J. Mater. Chem. C* **2020**, *8*, 3784−3794.

(374) Tian, A.; Zuo, R.; Qi, H.; Shi, M. Large Energy-Storage Density in Transition-Metal Oxide Modified $NaNbO_3$-$Bi(Mg_{0.5}$ $Ti_{0.5})O_3$ Lead-Free Ceramics through Regulating the Antiferroelectric Phase Structure. *J. Mater. Chem. A* **2020**, *8*, 8352−8359.

(375) Shi, R.; Pu, Y.; Wang, W.; Guo, X.; Li, J.; Yang, M.; Zhou, S. A Novel Lead-Free $NaNbO_3$-$Bi(Zn_{0.5}$ $Ti_{0.5})O_3$ Ceramics System for Energy Storage Application with Excellent Stability. *J. Alloys Compd.* **2020**, *815*, 152356.

(376) Sun, C.; Chen, X.; Shi, J.; Pang, F.; Dong, X.; Chen, H. Y.; Wang, K.; Zhou, X.; Zhou, H. Simultaneously with Large Energy Density and High Efficiency Achieved in $NaNbO_3$-Based Relaxor Ferroelectric Ceramics. *J. Eur. Ceram. Soc.* **2021**, *41*, 1891−1903.

(377) Zhou, M.; Liang, R.; Zhou, Z.; Dong, X. Superior Energy Storage Properties and Excellent Stability of Novel $NaNbO_3$-Based Lead-Free Ceramics with a-Site Vacancy Obtained Via a Bi_2o_3 Substitution Strategy. *J. Mater. Chem. A* **2018**, *6*, 17896−17904.

(378) Yang, L.; Kong, X.; Cheng, Z.; Zhang, S. Enhanced Energy Density and Electric Cycling Reliability Via Mno_2 Modification in Sodium Niobate-Based Relaxor Dielectric Capacitors. *J. Mater. Res.* **2021**, 1−9.

(379) Dong, X.; Li, X.; Chen, X.; Chen, H.; Sun, C.; Shi, J.; Pang, F.; Zhou, H. High Energy Storage Density and Power Density Achieved Simultaneously in $NaNbO_3$-Based Lead-Free Ceramics Via Antiferroelectricity Enhancement. *J. Materiomics* **2021**, *7*, 629−639.

(380) Chen, J.; Qi, H.; Zuo, R. Realizing Stable Relaxor Antiferroelectric and Superior Energy Storage Properties in $(Na_{1-X/2}$ $La_{x/2})$-$(Nb_{1-X}$ $Ti_x)O_3$ Lead-Free Ceramics through a/B-Site Complex Substitution. *ACS Appl. Mater. Interfaces* **2020**, *12*, 32871−32879.

(381) Chen, H.; Shi, J.; Chen, X.; Sun, C.; Pang, F.; Dong, X.; Zhang, H.; Zhou, H. Excellent Energy Storage Properties and Stability of $NaNbO_3$-$Bi(Mg_{0.5}Ta_{0.5})O_3$ Ceramics by Introducing $(Bi_{0.5}Na_{0.5})$-$0.7Sr_{0.3}TiO_3$. *J. Mater. Chem. A* **2021**, *9*, 4789.

(382) Liu, S.; Shen, B.; Hao, H.; Zhai, J. Glass-Ceramic Dielectric Materials with High Energy Density and Ultra-Fast Discharge Speed for High Power Energy Storage Applications. *J. Mater. Chem. C* **2019**, *7*, 15118−15135.

(383) Chen, G.-H.; Zhang, W.-J.; Liu, X.-Y.; Zhou, C.-R. Preparation and Properties of Strontium Barium Niobate Based Glass-Ceramics for Energy Storage Capacitors. *J. Electroceram.* **2011**, *27*, 78−82.

(384) Wang, S.; Tian, J.; Liu, J.; Yang, K.; Shen, B.; Zhai, J. Ultrahigh Energy Storage Density and Instantaneous Discharge Power Density in BaO-PbO-Na_2O-Nb_2O_5-SiO_2-Al_2O_3 Glass-Ceramics. *J. Mater. Chem. C* **2018**, *6*, 12608−12614.

(385) Luo, J.; Du, J.; Tang, Q.; Mao, C. Lead Sodium Niobate Glass-Ceramic Dielectrics and Internal Electrode Structure for High Energy Storage Density Capacitors. *IEEE Trans. Electron Devices* **2008**, *55*, 3549−3554.

(386) Yang, Y.; Song, J.; Chen, G.; Yuan, C.; Li, X.; Zhou, C. Effect of Crystallization Temperature on the Dielectric Property and Energy Density of SrO-BaO-Nb_2O_6-B_2O_3 Glass-Ceramics. *J. Non-Cryst. Solids* **2015**, *410*, 96−99.

(387) Xiao, S.; Xiu, S.; Xue, S.; Shen, B.; Zhai, J. Crystallization Behavior and Dielectric Properties of K_2O-SrO-Nb_2O_5-B_2O_3-Al_2O_3-SiO_2 Glass-Ceramic for Energy Storage. *J. Alloys Compd.* **2015**, *648*, 745−750.

(388) Liu, J.; Yang, K.; Zhai, J.; Shen, B. Effects of Crystallization Temperature on Phase Evolution and Energy Storage Properties of BaO-Na_2O-Nb_2O_5-SiO_2-Al_2O_3 Glass-Ceramics. *J. Eur. Ceram. Soc.* **2018**, *38*, 2312−2317.

(389) Jiang, T.; Chen, K.; Shen, B.; Zhai, J. Excellent Energy Storage and Charge-Discharge Performances in Sodium-Barium-Niobium Based Glass Ceramics. *Ceram. Int.* **2019**, *45*, 19429−19434.

(390) Wang, H.; Liu, J.; Zhai, J.; Shen, B.; Pan, Z.; Liu, J. R.; Yang, K. Effect of Crystallization Temperature on Dielectric and Energy-Storage Properties in SrO-Na_2O-Nb_2O_5-SiO_2 Glass-Ceramics. *Ceram. Int.* **2017**, *43*, 8898−8904.

(391) Tian, J.; Wang, S.; Jiang, T.; Chen, K.; Zhai, J.; Shen, B. Dielectric Characterization of a Novel Bi_2o_3-Nb_2O_5-SiO_2-Al_2O_3 Glass-Ceramic with Excellent Charge-Discharge Properties. *J. Eur. Ceram. Soc.* **2019**, *39*, 1164−1169.

(392) Liu, J.; Wang, H.; Shen, B.; Zhai, J.; Pan, Z.; Yang, K.; Liu, J. Crystallization Kinetics, Breakdown Strength, and Energy-Storage Properties in Niobate-Based Glass-Ceramics. *J. Alloys Compd.* **2017**, *722*, 212−218.

(393) Wang, H.; Liu, J.; Zhai, J.; Shen, B.; Pan, Z.; Yang, K.; Liu, J. Effect of K_2O Content on Breakdown Strength and Energy-Storage Density in K_2O-BaO-Nb_2O_5-SiO_2 Glass-Ceramics. *Ceram. Int.* **2017**, *43*, 4183−4187.

(394) Wang, H.; Liu, J.; Zhai, J.; Pan, Z.; Shen, B. Effects of Sr Substitution for Ba on Dielectric and Energy-Storage Properties of SrO-BaO-K_2O-Nb_2O_5-SiO_2 Glass-Ceramics. *J. Eur. Ceram. Soc.* **2017**, *37*, 3917−3925.

(395) Li, B.; Wang, D.; Chen, G.; Liu, X.; Yuan, C. Effect of K:Ba Ratio on Energy Storage Properties of Strontium Barium Potassium Niobate-Glass Ceramics. *J. Mater. Sci.: Mater. Electron.* **2019**, *30*, 19262−19269.

(396) Liu, J.; Yang, K.; Zhai, J.; Shen, B.; Wang, H.; Li, F. High Energy Storage Density and Rapid Discharge Speed of Niobosilicate Glasses. *Mater. Chem. Phys.* **2018**, *206*, 29−34.

(397) Smith, N. J.; Rangarajan, B.; Lanagan, M. T.; Pantano, C. G. Alkali-Free Glass as a High Energy Density Dielectric Material. *Mater. Lett.* **2009**, *63*, 1245−1248.

(398) Xiu, S.; Xiao, S.; Xue, S.; Shen, B.; Zhai, J. Effect of Different Al/Si Ratios on the Structure and Energy Storage Properties of Strontium Barium Niobate-Based Glass-Ceramics. *J. Electron. Mater.* **2016**, *45*, 1017−1022.

(399) Zhang, W.; Wang, J.; Xue, S.; Liu, S.; Shen, B.; Zhai, J. Effect of La_2O_3 Additive on the Dielectric Properties of Barium Strontium Titanate Glass-Ceramics. *J. Mater. Sci.: Mater. Electron.* **2014**, *25*, 4145−4149.

(400) Zheng, J.; Chen, G. H.; Yuan, C. L.; Zhou, C. R.; Chen, X.; Feng, Q.; Li, M. Dielectric Characterization and Energy-Storage Performance of Lead-Free Niobate Glass-Ceramics Added with La_2O_3. *Ceram. Int.* **2016**, *42*, 1827−1832.

(401) Zhou, Y.; Zhang, Q.; Luo, J.; Tang, Q.; Du, J. Structural Optimization and Improved Discharged Energy Density for Niobate Glass-Ceramics by La_2O_3 Addition. *J. Am. Ceram. Soc.* **2013**, *96*, 372−375.

(402) Chen, G. H.; Zheng, J.; Li, Z. C.; Yuan, C. L.; Zhou, C. R. Optimized Microstructure and Energy-Storage Density of Sm_2O_3-Added Lead-Free Borate Glass-Ceramic Composites. *J. Mater. Sci.: Mater. Electron.* **2016**, *27*, 8499−8503.

(403) Li, B.; Wang, D.; Chen, G.; Liu, X. Effect of Yb_2o_3 Content on Dielectric and Energy-Storage Properties of Lead-Free Niobate Glass-Ceramics. *J. Mater. Sci.: Mater. Electron.* **2018**, *29*, 19238−19244.

(404) Xiu, S.; Xiao, S.; Zhang, W.; Xue, S.; Shen, B.; Zhai, J. Effect of Rare-Earth Additions on the Structure and Dielectric Energy Storage Properties of Ba_x sr_{1-X} tio_3-Based Barium Boronaluminosilicate Glass-Ceramics. *J. Alloys Compd.* **2016**, *670*, 217−221.

(405) Yang, K.; Liu, J.; Shen, B.; Zhai, J.; Wang, H. Large Improvement on Energy Storage and Charge-Discharge Properties of Gd_2O_3-Doped BaO-K_2O-Nb_2O_5-SiO_2 Glass-Ceramic Dielectrics. *Mater. Sci. Eng., B* **2017**, *223*, 178−184.

(406) Xiu, S.; Xiao, S.; Shen, B.; Zhai, J. The Structure, Dielectric and Energy Storage Properties of Strontium Barium Niobate-Based Glass-Ceramics Doped with La_2O_3. *J. Electron. Mater.* **2017**, *46*, 4557−4561.

(407) Xiao, S.; Xiu, S.; Shen, B.; Zhai, J. Microstructure Evolution and Energy Storage Properties of Potassium Strontium Niobate Boroaluminosilicate Glass-Ceramics by Microwave Crystallization. *J. Eur. Ceram. Soc.* **2016**, *36*, 4071−4076.

(408) Zhang, W.; Xue, S.; Liu, S.; Wang, J.; Shen, B.; Zhai, J. Structure and Dielectric Properties of $Ba_xSr_{1-x}TiO_3$-Based Glass Ceramics for Energy Storage. *J. Alloys Compd.* **2014**, *617*, 740−745.

(409) Xue, S.; Zhai, J.; Xiao, S.; Xiu, S.; Shen, B. Improved Dielectric Breakdown Strength and Suppressed Energy Loss in Niobate Glass-Ceramics Crystallized by Microwave Process. *Mater. Lett.* **2017**, *190*, 154−156.

(410) Liu, J.; Wang, H.; Shen, B.; Zhai, J.; Li, P.; Pan, Z. Significantly Enhanced Energy-Storage Density in the Strontium Barium Niobate-Based/Titanate-Based Glass-Ceramics. *J. Am. Ceram. Soc.* **2017**, *100*, 506−510.

(411) Xiu, S.; Shen, B.; Zhai, J. The Effects of Mno_2 Addition on the Structure and Dielectric Properties of the Strontium Barium Niobate Glass-Ceramics. *Mater. Res. Bull.* **2017**, *95*, 349−353.

(412) Wang, H.; Liu, J.; Zhai, J.; Shen, B.; Xiu, S.; Xiao, S.; Pan, Z. Enhanced Energy Storage Density and Discharge Efficiency in the Strontium Sodium Niobate-Based Glass-Ceramics. *J. Alloys Compd.* **2016**, *687*, 280−285.

(413) Tian, J.; Wang, S.; Yang, K.; Liu, J.; Zhai, J.; Shen, B. Enhanced Energy Storage Properties of BaO-K_2O-Nb_2O_5-SiO_2 Glass Ceramics Obtained through Microwave Crystallization. *Ceram. Int.* **2018**, *44*, 15490−15494.

(414) Wang, S.; Tian, J.; Yang, K.; Liu, J.; Zhai, J.; Shen, B. Crystallization Kinetics Behavior and Dielectric Energy Storage Properties of Strontium Potassium Niobate Glass-Ceramics with Different Nucleating Agents. *Ceram. Int.* **2018**, *44*, 8528−8533.

(415) Hong, K.; Lee, T. H.; Suh, J. M.; Yoon, S.-H.; Jang, H. W. Perspectives and Challenges in Multilayer Ceramic Capacitors for Next Generation Electronics. *J. Mater. Chem. C* **2019**, *7*, 9782−9802.

(416) Wang, G.; Lu, Z.; Li, J.; Ji, H.; Yang, H.; Li, L.; Sun, S.; Feteira, A.; Yang, H.; Zuo, R.; et al. Lead-Free (Ba,Sr)TiO_3-$BiFeO_3$ Based Multilayer Ceramic Capacitors with High Energy Density. *J. Eur. Ceram. Soc.* **2020**, *40*, 1779−1783.

(417) Shrout, T. R.; Zhang, S. J. Lead-Free Piezoelectric Ceramics: Alternatives for PZT? *J. Electroceram.* **2007**, *19*, 113−126.

(418) Rödel, J.; Jo, W.; Seifert, K. T. P.; Anton, E.-M.; Granzow, T.; Damjanovic, D. Perspective on the Development of Lead-Free Piezoceramics. *J. Am. Ceram. Soc.* **2009**, *92*, 1153−1177.

(419) Rödel, J.; Webber, K. G.; Dittmer, R.; Jo, W.; Kimura, M.; Damjanovic, D. Transferring Lead-Free Piezoelectric Ceramics into Application. *J. Eur. Ceram. Soc.* **2015**, *35*, 1659−1681.

(420) Wang, D.; Khesro, A.; Murakami, S.; Feteira, A.; Zhao, Q.; Reaney, I. M. Temperature Dependent, Large Electromechanical Strain in Nd-Doped $BiFeO_3$-$BaTiO_3$ Lead-Free Ceramics. *J. Eur. Ceram. Soc.* **2017**, *37*, 1857−1860.

(421) Murakami, S.; Ahmed, N. T. A. F.; Wang, D.; Feteira, A.; Sinclair, D. C.; Reaney, I. M. Optimising Dopants and Properties in $Bimeo_3$ (Me = Al, Ga, Sc, Y, $Mg_{2/3}Nb_{1/3}$, $Zn_{2/3}Nb_{1/3}$, $Zn_{1/2}Ti_{1/2}$) Lead-Free $BaTiO_3$-$BiFeO_3$ Based Ceramics for Actuator Applications. *J. Eur. Ceram. Soc.* **2018**, *38*, 4220−4231.

(422) Murakami, S.; Wang, D.; Mostaed, A.; Khesro, A.; Feteira, A.; Sinclair, D. C.; Fan, Z.; Tan, X.; Reaney, I. M. High Strain (0.4%) $Bi(Mg_{2/3}Nb_{1/3})O_3$-$BaTiO_3$-$BiFeO_3$ Lead-Free Piezoelectric Ceramics and Multilayers. *J. Am. Ceram. Soc.* **2018**, *101*, 5428−5442.

(423) Wang, G.; Goetzee-Barral, A.; Lu, Z.; Keeble, D. S.; Hall, D. A. Thermally-Induced Local Structural Transformations in $Na_{0.5}Bi_{0.5}TiO_3$-$KNbO_3$ Ceramics. *J. Eur. Ceram. Soc.* **2021**, *41*, 3832−3837.

(424) Knowles Capacitors. Multilayer Ceramic Capacitors in Automotive. *Power Electronics Europe* 2017, 36.

(425) Sharma, S. K.; Shyam, A. Design and Testing of 45 Kv, 50 Khz Pulse Power Supply for Dielectric Barrier Discharges. *Rev. Sci. Instrum.* **2016**, *87*, 105115.

(426) Elsied, M.; Salem, A.; Oukaour, A.; Gualous, H.; Chaoui, H.; Youssef, F. T.; Belie, D.; Melkebeek, J.; Mohammed, O. *2015 IEEE Vehicle Power and Propulsion Conference (VPPC)* **2015**, 1−6.

(427) Obaid, Z. A.; Cipcigan, L. M.; Abrahim, L.; Muhssin, M. T. Frequency Control of Future Power Systems: Reviewing and Evaluating Challenges and New Control Methods. *J. Mod. Power Syst. Clean Energy* **2019**, *7*, 9−25.

(428) Siami, S.; Joubert, C.; Glaize, C. High Frequency Model for Power Electronics Capacitors. *IEEE Trans. Power Electron.* **2001**, *16*, 157−166.

(429) Yano, M.; Abe, S.; Ohno, E. In *IEEE Conference on the History of Electronics*; IEEE, 2004.

(430) Rashid, M. H. *Power Electronics Handbook [Electronic Resource]: Devices, Circuits, and Applications*; 3rd ed.; Elsevier/BH: Amsterdam, 2011.

(431) Hussain, F.; Khesro, A.; Lu, Z.; Wang, G.; Wang, D. Lead Free Multilayer Piezoelectric Actuators by Economically New Approach. *Front. Mater.* **2020**, *7*, 87.

(432) Khesro, A.; Wang, D.; Hussain, F.; Sinclair, D. C.; Feteira, A.; Reaney, I. M. Temperature Stable and Fatigue Resistant Lead-Free Ceramics for Actuators. *Appl. Phys. Lett.* **2016**, *109*, 142907.

(433) Multilayer Ceramic Capacitor Market, Global Opportunity Analysis and Industry Forecast, 2018−2024. *Allied Market Research* 2018, SE_184655.

(434) Shkuratov, S. I.; Baird, J.; Antipov, V. G.; Zhang, S.; Chase, J. B. Multilayer PZT 95/5 Antiferroelectric Film Energy Storage Devices with Giant Power Density. *Adv. Mater.* **2019**, *31*, 1904819.

(435) Chen, L.; Sun, N.; Li, Y.; Zhang, Q.; Zhang, L.; Hao, X. Multifunctional Antiferroelectric Mlcc with High-Energy-Storage Properties and Large Field-Induced Strain. *J. Am. Ceram. Soc.* **2018**, *101*, 2313−2320.

(436) Liu, X.; Li, Y.; Sun, N.; Hao, X. High Energy-Storage Performance of Plzs Antiferroelectric Multilayer Ceramic Capacitors. *Inorg. Chem. Front.* **2020**, *7*, 756−764.

(437) Cai, Z.; Zhu, C.; Wang, H.; Zhao, P.; Chen, L.; Li, L.; Wang, X. High-Temperature Lead-Free Multilayer Ceramic Capacitors with Ultrahigh Energy Density and Efficiency Fabricated Via Two-Step Sintering. *J. Mater. Chem. A* **2019**, *7*, 14575−14582.

(438) Zhao, P.; Wang, H.; Wu, L.; Chen, L.; Cai, Z.; Li, L.; Wang, X. High-Performance Relaxor Ferroelectric Materials for Energy Storage Applications. *Adv. Energy Mater.* **2019**, *9*, 1803048.

(439) Li, J.; Shen, Z.; Chen, X.; Yang, S.; Zhou, W.; Wang, M.; Wang, L.; Kou, Q.; Liu, Y.; Li, Q.; et al. Grain-Orientation-Engineered Multilayer Ceramic Capacitors for Energy Storage Applications. *Nat. Mater.* **2020**, *19*, 999−1005.

(440) Jia, W.; Hou, Y.; Zheng, M.; Xu, Y.; Yu, X.; Zhu, M.; Yang, K.; Cheng, H.; Sun, S.; Xing, J. Superior Temperature-Stable Dielectrics for Mlccs Based on $Bi_{0.5}Na_{0.5}TiO_3$-$NaNbO_3$ System Modified by $CaZrO_3$. *J. Am. Ceram. Soc.* **2018**, *101*, 3468−3479.

(441) Yuan, Q.; Cui, J.; Wang, Y.; Ma, R.; Wang, H. Significant Enhancement in Breakdown Strength and Energy Density of the $BaTiO_3$/$BaTiO_3$@SiO_2 Layered Ceramics with Strong Interface Blocking Effect. *J. Eur. Ceram. Soc.* **2017**, *37*, 4645−4652.

(442) Yan, F.; Yang, H.; Ying, L.; Wang, T. Enhanced Energy Storage Properties of a Novel Lead-Free Ceramic with a Multilayer Structure. *J. Mater. Chem. C* **2018**, *6*, 7905−7912.

(443) Tong, X.-Y.; Yang, Y.-T.; Song, M.-W.; Zhou, J.-J.; Wang, K.; Guan, C.-L.; Liu, H.; Fang, J.-Z. Energy-Storage Properties of Low-Temperature Co-Fired BNT-St/Agpd Multilayer Lead-Free Ceramic Capacitors. *J. Alloys Compd.* **2020**, *827*, 154260.

(444) Chen, L.; Wang, H.; Zhao, P.; Zhu, C.; Cai, Z.; Cen, Z.; Li, L.; Wang, X. Multifunctional $BaTiO_3$-$(Bi_{0.5}Na_{0.5})TiO_3$-Based Mlcc with High-Energy Storage Properties and Temperature Stability. *J. Am. Ceram. Soc.* **2019**, *102*, 4178−4187.

(445) Lee, H.; Kim, J. R.; Lanagan, M. J.; Trolier-McKinstry, S.; Randall, C. A. High-Energy Density Dielectrics and Capacitors for Elevated Temperatures: $Ca(Zr,Ti)O_3$. *J. Am. Ceram. Soc.* **2013**, *96*, 1209−1213.

(446) Cai, Z.; Wang, H.; Zhao, P.; Chen, L.; Zhu, C.; Hui, K.; Li, L.; Wang, X. Significantly Enhanced Dielectric Breakdown Strength and Energy Density of Multilayer Ceramic Capacitors with High Efficiency by Electrodes Structure Design. *Appl. Phys. Lett.* **2019**, *115*, 023901.

(447) Wang, H.; Zhao, P.; Chen, L.; Wang, X. Effects of Dielectric Thickness on Energy Storage Properties of $0.87batio_3$-$0.13bi$-$(Zn_{2/3}(Nb_{0.85}\ ta_{0.15})_{1/3})O_3$ Multilayer Ceramic Capacitors. *J. Eur. Ceram. Soc.* **2020**, *40*, 1902−1908.

(448) Wang, H.; Zhao, P.; Chen, L.; Li, L.; Wang, X. Energy Storage Properties of $0.87BaTiO_3$-$0.13Bi(Zn_{2/3}(Nb_{0.85}\ Ta_{0.15})_{1/3})O_3$ Multilayer Ceramic Capacitors with Thin Dielectric Layers. *J. Adv. Ceram.* **2020**, *9*, 292−302.

(449) Shen, B.-Z.; Li, Y.; Hao, X. Multifunctional All-Inorganic Flexible Capacitor for Energy Storage and Electrocaloric Refrigeration over a Broad Temperature Range Based on PLZT 9/65/35 Thick Films. *ACS Appl. Mater. Interfaces* **2019**, *11*, 34117−34127.

(450) Zhao, Q. L.; Cao, M. S.; Yuan, J.; Song, W. L.; Lu, R.; Wang, D. W.; Zhang, D. Q. Preparation and Electrical Properties of Pb-$(Zr_{0.52}Ti_{0.48})O_3$ Thick Films Embedded with ZnO Nanowhiskers by a Hybrid Sol-Gel Route. *J. Alloys Compd.* **2010**, *492*, 264−268.

(451) Zhao, Q.; Su, D.; Cao, M.; He, G.; Di, J.; Yuan, J.; Wang, D. Thickness-Dependent Electrical Properties of Sol-Gel Derived Pb-$(Zr_{0.52}Ti_{0.48})O_3$ Thick Films Using $PbTiO_3$ Buffer Layers. *J. Mater. Sci.: Mater. Electron* **2013**, *24*, 3521−3525.

(452) Pan, H.; Li, F.; Liu, Y.; Zhang, Q.; Wang, M.; Lan, S.; Zheng, Y.; Ma, J.; Gu, L.; Shen, Y.; et al. Ultrahigh-Energy Density Lead-Free Dielectric Films Via Polymorphic Nanodomain Design. *Science* **2019**, *365*, 578.

(453) Lin, Z.; Chen, Y.; Liu, Z.; Wang, G.; Rémiens, D.; Dong, X. Large Energy Storage Density, Low Energy Loss and Highly Stable $(Pb_{0.97}\ La_{0.02})(Zr_{0.66}\ Sn_{0.23}\ Ti_{0.11})O_3$ Antiferroelectric Thin-Film Capacitors. *J. Eur. Ceram. Soc.* **2018**, *38*, 3177−3181.

(454) Sun, N.; Wang, Y.; Zhang, L.; Zhang, X.; Hao, X.; Li, M. Effects of Thickness on the Microstructure and Energy-Storage Performance of PLZT Antiferroelectric Thick Films. *J. Adv. Dielectr.* **2013**, *03*, 1350021.

(455) Wang, J.; Sun, N.; Li, Y.; Zhang, Q.; Hao, X.; Chou, X. Effects of Mn Doping on Dielectric Properties and Energy-Storage Performance of $Na_{0.5}Bi_{0.5}TiO_3$ Thick Films. *Ceram. Int.* **2017**, *43*, 7804−7809.

(456) Wang, J.; Li, Y.; Sun, N.; Zhang, Q.; Zhang, L.; Hao, X.; Chou, X. Effects of Fe^{3+} Doping on Electrical Properties and Energy-Storage Performances of the $(Na_{0.85}K_{0.15})_{0.5}\ Bi_{0.5}TiO_3$ Thick Films Prepared by Sol-Gel Method. *J. Alloys Compd.* **2017**, *727*, 596−602.

(457) Sun, N.; Li, Y.; Zhang, Q.; Hao, X. Giant Energy-Storage Density and High Efficiency Achieved in $(Bi_{0.5}Na_{0.5})TiO_3$-$Bi(Ni_{0.5}\ Zr_{0.5})O_3$ Thick Films with Polar Nanoregions. *J. Mater. Chem. C* **2018**, *6*, 10693−10703.

(458) Park, M. H.; Kim, H. J.; Kim, Y. J.; Moon, T.; Kim, K. D.; Hwang, C. S. Thin $Hf_x\ zr_{1-x}o_2$ Films: A New Lead-Free System for Electrostatic Supercapacitors with Large Energy Storage Density and Robust Thermal Stability. *Adv. Energy Mater.* **2014**, *4*, 1400610.

(459) Payne, A.; Brewer, O.; Leff, A.; Strnad, N. A.; Jones, J. L.; Hanrahan, B. Dielectric, Energy Storage, and Loss Study of Antiferroelectric-Like Al-Doped Hfo_2 Thin Films. *Appl. Phys. Lett.* **2020**, *117*, 221104.

(460) Liu, Y.; Wang, Y.; Hao, X.; Xu, J. Preparation and Energy-Storage Performance of PLZT Antiferroelectric Thick Films Via Sol-Gel Method. *Ceram. Int.* **2013**, *39*, S513−S516.

(461) Wu, S.; Chen, P.; Zhai, J.; Shen, B.; Li, P.; Li, F. Enhanced Piezoelectricity and Energy Storage Performances of Fe-Doped BNT-BKT-St Thin Films. *Ceram. Int.* **2018**, *44*, 21289−21294.

(462) Ahn, C. W.; Amarsanaa, G.; Won, S. S.; Chae, S. A.; Lee, D. S.; Kim, I. W. Antiferroelectric Thin-Film Capacitors with High Energy-Storage Densities, Low Energy Losses, and Fast Discharge Times. *ACS Appl. Mater. Interfaces* **2015**, *7*, 26381−26386.

(463) Tong, S.; Ma, B.; Narayanan, M.; Liu, S.; Koritala, R.; Balachandran, U.; Shi, D. Lead Lanthanum Zirconate Titanate Ceramic Thin Films for Energy Storage. *ACS Appl. Mater. Interfaces* **2013**, *5*, 1474−1480.

(464) Cai, H.; Yan, S.; Zhou, M.; Liu, N.; Ye, J.; Li, S.; Cao, F.; Dong, X.; Wang, G. Significantly Improved Energy Storage Properties and Cycling Stability in La-Doped $PbZrO_3$ Antiferroelectric Thin Films by Chemical Pressure Tailoring. *J. Eur. Ceram. Soc.* **2019**, *39*, 4761−4769.

(465) Peddigari, M.; Palneedi, H.; Hwang, G.-T.; Lim, K. W.; Kim, G.-Y.; Jeong, D.-Y.; Ryu, J. Boosting the Recoverable Energy Density of Lead-Free Ferroelectric Ceramic Thick Films through Artificially Induced Quasi-Relaxor Behavior. *ACS Appl. Mater. Interfaces* **2018**, *10*, 20720−20727.

(466) Yang, X.; Li, W.; Qiao, Y.; Zhang, Y.; He, J.; Fei, W. High Energy-Storage Density of Lead-Free $(Sr_{1-1.5x}\ Bi_x)Ti_{0.99}\ Mn_{0.01}O_3$ Thin Films Induced by Bi^{3+}-V_{sr} Dipolar Defects. *Phys. Chem. Chem. Phys.* **2019**, *21*, 16359−16366.

(467) Wang, Y.; Hao, X.; Xu, J. Effects of PbO Insert Layer on the Microstructure and Energy Storage Performance of (042)-Preferred PLZT Antiferroelectric Thick Films. *J. Mater. Res.* **2012**, *27*, 1770−1775.

(468) Xie, J.; Yao, Z.; Hao, H.; Xie, Y.; Li, Z.; Liu, H.; Cao, M. A Novel Lead-Free Bismuth Magnesium Titanate Thin Films for Energy Storage Applications. *J. Am. Ceram. Soc.* **2019**, *102*, 3819−3822.

(469) Dang, H. T.; Trinh, T. T.; Nguyen, C. T. Q.; Do, T. V.; Nguyen, M. D.; Vu, H. N. Enhancement of Relaxor Behavior by La Doping and Its Influence on the Energy Storage Performance and Electric Breakdown Strength of Ferroelectric $Pb(Zr_{0.52}Ti_{0.48})O_3$ Thin Films. *Mater. Chem. Phys.* **2019**, *234*, 210−216.

(470) Won, S. S.; Kawahara, M.; Kuhn, L.; Venugopal, V.; Kwak, J.; Kim, I. W.; Kingon, A. I.; Kim, S.-H. $BiFeO_3$-Doped $(K_{0.5},Na_{0.5})$-$(Mn_{0.005},Nb_{0.995})O_3$ Ferroelectric Thin Film Capacitors for High Energy Density Storage Applications. *Appl. Phys. Lett.* **2017**, *110*, 152901.

(471) Zhang, T.; Li, W.; Hou, Y.; Yu, Y.; Song, R.; Cao, W.; Fei, W. High-Energy Storage Density and Excellent Temperature Stability in

Antiferroelectric/Ferroelectric Bilayer Thin Films. *J. Am. Ceram. Soc.* **2017**, *100*, 3080−3087.

(472) Sun, B.; Guo, M.; Wu, M.; Ma, Z.; Gao, W.; Sun, H.; Lou, X. Large Enhancement of Energy Storage Density in $(Pb_{0.92}\ la_{0.08})(Zr_{0.65}\ ti_{0.35})O_3/PbZrO_3$ Multilayer Thin Film. *Ceram. Int.* **2019**, *45*, 20046−20050.

(473) Wang, X.; Zhang, L.; Hao, X.; An, S. High Energy-Storage Performance of $0.9Pb(Mg_{1/3}Nb_{2/3})O_3$-$0.1PbTiO_3$ Relaxor Ferroelectric Thin Films Prepared by Rf Magnetron Sputtering. *Mater. Res. Bull.* **2015**, *65*, 73−79.

(474) Yao, Y.; Li, Y.; Sun, N.; Du, J.; Li, X.; Zhang, L.; Zhang, Q.; Hao, X. High Energy-Storage Performance of BNT-BT-Nn Ferroelectric Thin Films Prepared by Rf Magnetron Sputtering. *J. Alloys Compd.* **2018**, *750*, 228−234.

(475) Wang, C.; Sun, N.; Hao, X. Dielectric Property and Energy-Storage Performance Of $(1\text{-}X)PbTiO_3$-$Xbi(Mg_{0.5}\ Zr_{0.5})O_3$ Relaxor Ferroelectric Thin Films. *J. Mater. Sci.: Mater. Electron* **2020**, *31*, 2063−2072.

(476) Xu, Z.; Hao, X.; An, S. Dielectric Properties and Energy-Storage Performance of $(Na_{0.5}\ Bi_{0.5})TiO_3$-$SrTiO_3$ Thick Films Derived from Polyvinylpyrrolidone-Modified Chemical Solution. *J. Alloys Compd.* **2015**, *639*, 387−392.

(477) Yang, B.; Guo, M.; Tang, X.; Wei, R.; Hu, L.; Yang, J.; Song, W.; Dai, J.; Lou, X.; Zhu, X.; et al. Lead-Free $A_2\ Bi_4Ti_{15}O_{18}$ Thin Film Capacitors (a = Ba and Sr) with Large Energy Storage Density, High Efficiency, and Excellent Thermal Stability. *J. Mater. Chem. C* **2019**, *7*, 1888−1895.

(478) Zhao, Y.; Hao, X.; Zhang, Q. Energy-Storage Properties and Electrocaloric Effect of $Pb_{(1-3x/2)}La_x\ Zr_{0.85}Ti_{0.15}O_3$ Antiferroelectric Thick Films. *ACS Appl. Mater. Interfaces* **2014**, *6*, 11633−11639.

(479) Kühnel, K.; Czernohorsky, M.; Mart, C.; Weinreich, W. High-Density Energy Storage in Si-Doped Hafnium Oxide Thin Films on Area-Enhanced Substrates. *J. Vac. Sci. Technol., B: Nanotechnol. Microelectron.: Mater., Process., Meas., Phenom.* **2019**, *37*, 021401.

(480) Tang, Z.; Ge, J.; Ni, H.; Lu, B.; Tang, X.-G.; Lu, S.-G.; Tang, M.; Gao, J. High Energy-Storage Density of Lead-Free $BiFeO_3$ Doped $Na_{0.5}Bi_{0.5}TiO_3$-$BaTiO_3$ Thin Film Capacitor with Good Temperature Stability. *J. Alloys Compd.* **2018**, *757*, 169−176.

(481) Song, D. P.; Yang, J.; Yang, B. B.; Wang, Y.; Chen, L. Y.; Wang, F.; Zhu, X. B. Energy Storage in $BaBi_4Ti_4O_{15}$ Thin Films with High Efficiency. *J. Appl. Phys.* **2019**, *125*, 134101.

(482) Yang, B. B.; Guo, M. Y.; Song, D. P.; Tang, X. W.; Wei, R. H.; Hu, L.; Yang, J.; Song, W. H.; Dai, J. M.; Lou, X. J.; et al. $Bi_{3.25}La_{0.75}Ti_3O_{12}$ Thin Film Capacitors for Energy Storage Applications. *Appl. Phys. Lett.* **2017**, *111*, 183903.

(483) Xie, Z.; Peng, B.; Zhang, J.; Zhang, X.; Yue, Z.; Li, L. Effects of Thermal Anneal Temperature on Electrical Properties and Energy-Storage Density of $Bi(Ni_{1/2}\ Ti_{1/2})O_3$-$PbTiO_3$ Thin Films. *Ceram. Int.* **2015**, *41*, S206−S212.

(484) Zhang, L.; Yang, B.; Yu, J.; Deng, Y.; Huang, K.; Zhang, M.; Zhu, X. Energy Storage Properties in $SrTiO_3$-$Bi_{3.25}La_{0.75}Ti_3O_{12}$ Thin Films. *J. Alloys Compd.* **2019**, *799*, 66−70.

(485) Song, B.; Wu, S.; Li, F.; Chen, P.; Shen, B.; Zhai, J. Excellent Energy Storage Density and Charge-Discharge Performance of a Novel $Bi_{0.2}Sr_{0.7}TiO_3$-$BiFeO_3$ Thin Film. *J. Mater. Chem. C* **2019**, *7*, 10891−10900.

(486) Lomenzo, P. D.; Chung, C.-C.; Zhou, C.; Jones, J. L.; Nishida, T. Doped $Hf_{0.5}Zr_{0.5}O_2$ for High Efficiency Integrated Supercapacitors. *Appl. Phys. Lett.* **2017**, *110*, 232904.

(487) Xie, Z.; Yue, Z.; Peng, B.; Li, L. Effect of PbO Excess on the Microstructure, Dielectric and Piezoelectric Properties, and Energy-Storage Performance of $Bi(Ni_{1/2}\ Ti_{1/2})O_3$-$PbTiO_3$ Thin Films. *Jpn. J. Appl. Phys.* **2014**, *53*, 08NA02.

(488) Hao, X.; Wang, Y.; Zhang, L.; Zhang, L.; An, S. Composition-Dependent Dielectric and Energy-Storage Properties of (Pb,La)-$(Zr,Sn,Ti)O_3$ Antiferroelectric Thick Films. *Appl. Phys. Lett.* **2013**, *102*, 163903.

(489) Yang, B. B.; Guo, M. Y.; Song, D. P.; Tang, X. W.; Wei, R. H.; Hu, L.; Yang, J.; Song, W. H.; Dai, J. M.; Lou, X. J.; et al. Energy Storage Properties in $BaTiO_3$-$Bi_{3.25}La_{0.75}Ti_3O_{12}$ Thin Films. *Appl. Phys. Lett.* **2018**, *113*, 183902.

(490) Ali, F.; Liu, X.; Zhou, D.; Yang, X.; Xu, J.; Schenk, T.; Müller, J.; Schroeder, U.; Cao, F.; Dong, X. Silicon-Doped Hafnium Oxide Anti-Ferroelectric Thin Films for Energy Storage. *J. Appl. Phys.* **2017**, *122*, 144105.

(491) Yang, C. H.; Yao, Q.; Qian, J.; Han, Y. J.; Chen, J. Growth, Microstructure, Energy-Storage and Dielectric Performances of Chemical-Solution Nbt-Based Thin Films: Effect of Sodium Non-stoichimometry. *Ceram. Int.* **2018**, *44*, 9152−9158.

(492) Yang, B. B.; Guo, M. Y.; Jin, L. H.; Tang, X. W.; Wei, R. H.; Hu, L.; Yang, J.; Song, W. H.; Dai, J. M.; Lou, X. J.; et al. Ultrahigh Energy Storage in Lead-Free $BiFeO_3/Bi_{3.25}La_{0.75}Ti_3O_{12}$ Thin Film Capacitors by Solution Processing. *Appl. Phys. Lett.* **2018**, *112*, 033904.

(493) Yang, C.; Yao, Q.; Qian, J.; Han, Y.; Chen, J. Comparative Study on Energy Storage Performance of $Na_{0.5}\ bi_{0.5}(Ti,W,Ni)O_3$ Thin Films with Different Bismuth Contents. *Ceram. Int.* **2018**, *44*, 9643−9648.

(494) Pan, H.; Ma, J.; Ma, J.; Zhang, Q.; Liu, X.; Guan, B.; Gu, L.; Zhang, X.; Zhang, Y.-J.; Li, L.; et al. Giant Energy Density and High Efficiency Achieved in Bismuth Ferrite-Based Film Capacitors Via Domain Engineering. *Nat. Commun.* **2018**, *9*, 1813.

(495) Yang, C.; Lv, P.; Qian, J.; Han, Y.; Ouyang, J.; Lin, X.; Huang, S.; Cheng, Z. Fatigue-Free and Bending-Endurable Flexible Mn-Doped $Na_{0.5}Bi_{0.5}TiO_3$-$BaTiO_3$-$BiFeO_3$ Film Capacitor with an Ultrahigh Energy Storage Performance. *Adv. Energy Mater.* **2019**, *9*, 1803949.

(496) Wang, K.; Ouyang, J.; Wuttig, M.; Zhao, Y.-Y.; Cheng, H.; Zhang, Y.; Su, R.; Yan, J.; Zhong, X.; Zeng, F. Superparaelectric $(Ba_{0.95},Sr_{0.05})(Zr_{0.2},Ti_{0.8})O_3$ Ultracapacitors. *Adv. Energy Mater.* **2020**, *10*, 2001778.

(497) Kim, J.; Saremi, S.; Acharya, M.; Velarde, G.; Parsonnet, E.; Donahue, P.; Qualls, A.; Garcia, D.; Martin, L. W. Ultrahigh Capacitive Energy Density in Ion-Bombarded Relaxor Ferroelectric Films. *Science* **2020**, *369*, 81−84.

(498) Levin, I.; Laws, W. J.; Wang, D.; Reaney, I. M. Designing Pseudocubic Perovskites with Enhanced Nanoscale Polarization. *Appl. Phys. Lett.* **2017**, *111*, 212902.

(499) Lin, Y.; Li, D.; Zhang, M.; Zhan, S.; Yang, Y.; Yang, H.; Yuan, Q. Excellent Energy-Storage Properties Achieved in $BaTiO_3$-Based Lead-Free Relaxor Ferroelectric Ceramics Via Domain Engineering on the Nanoscale. *ACS Appl. Mater. Interfaces* **2019**, *11*, 36824−36830.

(500) Wu, L.; Wang, X.; Li, L. Core-Shell $BaTiO_3@BiScO_3$ Particles for Local Graded Dielectric Ceramics with Enhanced Temperature Stability and Energy Storage Capability. *J. Alloys Compd.* **2016**, *688*, 113−121.

(501) Zhang, Y.; Cao, M.; Yao, Z.; Wang, Z.; Song, Z.; Ullah, A.; Hao, H.; Liu, H. Effects of Silica Coating on the Microstructures and Energy Storage Properties of $BaTiO_3$ Ceramics. *Mater. Res. Bull.* **2015**, *67*, 70−76.

(502) Yang, H.; Liu, P.; Yan, F.; Lin, Y.; Wang, T. A Novel Lead-Free Ceramic with Layered Structure for High Energy Storage Applications. *J. Alloys Compd.* **2019**, *773*, 244−249.

(503) Heath, J. P.; Harding, J. H.; Sinclair, D. C.; Dean, J. S. Electric Field Enhancement in Ceramic Capacitors Due to Interface Amplitude Roughness. *J. Eur. Ceram. Soc.* **2019**, *39*, 1170−1177.